

National Technical University of Athens

---

SCHOOL OF MECHANICAL ENGINEERING

FLUIDS SECTION

LABORATORY OF THERMAL TURBOMACHINERY



# Turbofan Inter-Compressor Duct Pressure Loss Model Using CFD

## **Supervisor**

Nikolaos Aretakis, Associate Professor

## **Candidate**

Aspasia Anastasiou

---

Athens, Academic Year 2020 – 2021



# Acknowledgements

I would first like to thank my supervisor, associate professor Nikolaos Aretakis, who offered me the opportunity to work on such an interesting topic and guided me throughout it. I am grateful for his insightful feedback which encouraged me during this project.

Secondly, I would like to express my appreciation for the PhD. Candidate Konstantinos Ntonas, who was always available for my questions regarding the setup of the simulations, and Dr. Alexio Alexiou, for his invaluable advice.

I am grateful for the constant support of my parents and my brother throughout my studies. Finally, I would like to thank my friends for the cherished times we had together along this journey. A special thanks goes to Antonio for his understanding and encouragement.



# Abstract

Air transport sector has evolved rapidly in recent years leading to a significant increase of interest around the design and optimization of the aircraft engines. More specifically, in the last decades, researchers' focus has concentrated on improving the efficiency of the already existing engines by analyzing their main components. The development of Computational Fluid Dynamics methods has assisted in this direction, since the simulation of the flow within the engine was enabled.

One of the parts of the turbofan engine which has attracted the interest of the scientific community is the intermediate compressor duct. This duct, which is S-shaped, guides the flow from the low to the high-pressure compression system. Due to its curvature, an adverse radial pressure gradient and centrifugal forces are generated causing the flow to separate. The flow patterns developed within the duct, have been explored in detail by the researchers, and are significantly influenced by its geometry, the existence of load-carrying struts and the inlet flow. Furthermore, several techniques have been proposed to optimize the performance of the S-shaped duct, either by optimizing its shape or by adopting a more integrated design approach. All these methods aim to improve the efficiency of the duct and reduce its total pressure losses.

In this work, the ducts of seventeen existing turbofan engines have been examined. The geometry of the duct for each case was obtained by the digitization of its section view. The reconstructed ducts were analyzed to determine the basic parameters used to accurately describe its geometry. For the radii and the area along the duct, non-dimensional distributions were generated, using quadratic and cubic polynomial functions, respectively. The curvature of the duct walls could be derived from the coefficient of the quadratic term of the shroud radius distribution,  $a_{2_{\text{shroud}}}$ , which combined with the non-dimensional parameters  $\Delta R/L$ ,  $h_{\text{in}}/L$ ,  $R_{\text{min}}/L$ ,  $A_{\text{out}}/A_{\text{in}}$  and the length  $L$  could be used to parametrize the duct's geometry. This process is named Parametrization Process I. For the second procedure proposed, Process II, the  $a_{2_{\text{shroud}}}$ ,  $(R_{\text{hub}}/R_{\text{shroud}})_{\text{in}}$ ,  $(R_{\text{hub}}/R_{\text{shroud}})_{\text{out}}$  and  $M_{\text{in}}$ ,  $M_{\text{out}}$  should be given.

For a  $10^\circ$  sector of the digitized and parametrized ducts CFD flow simulation were conducted, using ANSYS CFX, to obtain the total pressure loss factor  $DP/P$ . The base case examined corresponded to the duct of GE90. After carrying out a grid independence study, a refined mesh was used with the  $y^+$  value maintained lower than 2. The turbulence model selected for the simulation was the Shear Stress Transport  $k-\omega$  model. At the inlet of the duct the total pressure and temperature were specified, while for the outlet the total mass

flow rate was determined. The total pressure loss factor and the inlet Mach number were determined with both being within the expected range.

The purpose of this work was to develop a model capable of providing an accurate estimation of the pressure losses depending on the duct's geometry and operating point. To acquire the expressions included in the model, a parametric study was conducted. Analytically, the influence of the non-dimensional variables used to parametrize the duct was examined through CFD simulations. It was observed that the losses were reduced for increasing  $a_{2_{\text{shroud}'}}$  while their correlation with  $\Delta R/L, h_{\text{in}}/L, R_{\text{min}}/L$  was independent of the radii distribution coefficient. An exponential relation between the losses and the mass flow rate, as a percentage of the design value for the duct, was also discovered. The exponent used in this function was varying with the curvature of the duct's walls.

After developing the model, it was validated by comparing its results for four different cases with the CFD simulation results obtained using the Parametrization Process II. The deviations calculated for the factor  $DP/P$  were insignificant, leading to the conclusion that the model is accurate. . Finally, based on the model's estimations a parametric study was conducted, resulting in conclusions for the selection of the input geometric values in order to maintain the pressure loss and the overall duct's weight within the desired range.

# Table of Contents

<b>Acknowledgements</b> .....	<b>iii</b>
<b>Abstract</b> .....	<b>v</b>
<b>Nomenclature</b> .....	<b>x</b>
<b>List of Tables</b> .....	<b>xii</b>
<b>List of Figures</b> .....	<b>xiii</b>
<b>Chapter 1 Introduction</b> .....	<b>1</b>
1.1 Review of Air Transports' Evolution.....	1
1.2 Thesis Purpose and Outline .....	2
<b>Chapter 2 Intermediate Compressor Duct</b> .....	<b>4</b>
2.1 Modern Aircraft Engines.....	4
2.2 The Intermediate Compressor Duct .....	7
2.3 Performance Parameters of Intermediate Duct .....	7
2.4 Fundamental Factors Affecting S-Duct Performance.....	9
2.4.1 Duct Geometry .....	9
2.4.2 Wall Curvature .....	11
2.4.3 Upstream Compressor Stage .....	13
2.4.4 Struts.....	14
2.4.5 Inlet Flow Conditions .....	16
2.5 Enhancement Techniques.....	17
2.5.1 Shape Optimization .....	17
2.5.2 Integrated Design.....	20
2.5.3 Flow Controlling Devices .....	22
<b>Chapter 3 Analysis and Parametrization Process of Existing Turbofan Engines</b> ...	<b>24</b>
3.1 Digitization of Turbofan Engines .....	24
3.2 Analysis of Digitized Data .....	26
3.2.1 Calculation of Main Geometric Parameters.....	26
3.2.2 Radius Distribution.....	27
3.2.3 Area Distribution .....	31
3.3 Parameterization Process.....	33
<b>Chapter 4 Flow Simulation in CFX</b> .....	<b>35</b>
4.1 Mesh Generation .....	35

4.1.1	Mesh Method .....	36
4.1.2	Inflation .....	37
4.1.3	Sizing.....	39
4.1.4	Match Control.....	39
4.2	Simulation Setup at CFX-Pre .....	40
4.2.1	Physical Models .....	40
4.2.2	Boundary Conditions.....	42
4.2.3	Solver Control.....	44
4.3	Post Processing.....	45
4.4	Flow Simulation for the Base Case.....	47
4.4.1	Mesh Independence Study.....	47
4.4.2	Boundary Conditions.....	49
4.4.3	Results .....	50
<b>Chapter 5</b>	<b>Development and Validation of Model for Estimation of Losses.....</b>	<b>54</b>
5.1	Parametric Study .....	54
5.1.1	Influence of <b>a2shroud</b> .....	54
5.1.2	Influence of <b><math>\Delta R/L</math></b> .....	57
5.1.3	Influence of <b>hin/L</b> .....	61
5.1.4	Influence of <b>Rmin/L</b> .....	64
5.1.5	Off-Design Mass Flow Rate.....	67
5.2	Development of Algebraic Model.....	70
5.3	Validation of Model.....	71
5.3.1	Case 1 .....	72
5.3.2	Case 2 .....	73
5.3.3	Case 3 .....	74
5.3.4	Case 4 .....	75
5.4	Parametric study based on the model's results.....	76
5.4.1	Variation of <b>a2shroud</b> .....	77
5.4.2	Variation of Length.....	78
5.4.3	Variation of <b>Rhub/Rshroud</b> .....	80
5.4.4	Variation of Mach Numbers.....	83
<b>Chapter 6</b>	<b>Conclusions and Future Work.....</b>	<b>87</b>
6.1	Overview.....	87
6.2	Conclusions.....	87
6.3	Future Prospects .....	89
<b>Appendix A:</b>	<b>Digitized Turbofans' Engines.....</b>	<b>90</b>
<b>Bibliography</b>	<b>.....</b>	<b>94</b>
<b>Εκτεταμένη Περίληψη Διπλωματικής Εργασίας</b>	<b>.....</b>	<b>98</b>
Η ροή εντός του αγωγού.....		98
Ανάλυση και Παραμετροποίηση αγωγών υπαρκτών κινητήρων τύπου Turbofan .....		100
Προσομοίωση της ροής στο λογισμικό ANSYS CFX.....		103
Δημιουργία Μοντέλου Εκτίμησης Απωλειών Πίεσης.....		105
Επαλήθευση Μοντέλου .....		109
Παραμετρική Μελέτη για Ελαχιστοποίηση Απωλειών.....		110



Συμπεράσματα..... 113

---

# Nomenclature

<i>ICAO</i>	International Civil Aviation Organization
<i>IATA</i>	Air Transport Association
<i>ATAG</i>	Air Transport Action Group
<i>CFD</i>	Computational Fluid Dynamic
<i>HPC</i>	High Pressure Compressor
<i>IPC</i>	Intermediate Pressure Compressor
<i>LPC</i>	Low Pressure Compressor
<i>CC</i>	Combustion Chamber
<i>HPT</i>	High Pressure Turbine
<i>IPT</i>	Intermediate Pressure Turbine
<i>LPT</i>	Low Pressure Turbine
<i>ICD</i>	Intermediate Compressor Duct
<i>BPR</i>	Bypass Ratio
<i>OPR</i>	Overall Pressure Ratio
<i>TIT</i>	Turbine Inlet Temperature
<i>OGV</i>	Outlet Guide Vanes
<i>IBL</i>	Inlet Boundary Layer
<i>ANN</i>	Artificial Neural Networks
<i>DOE</i>	Design of Experiments
<i>FFD</i>	Free Form Deformation
<i>GA</i>	Genetic Algorithm
<i>RSM</i>	Response Surface Methodology
<i>TS</i>	TABU Search Algorithm
<i>VG</i>	Vortex Generator
<i>DNS</i>	Direct Numerical Simulation
<i>RANS</i>	Reynolds Averaged Navier Stokes
<i>SST</i>	Shear Stress Transport
<i>RSM</i>	Reynolds Stress Model
<i>LES</i>	Large Eddy Simulation
<i>A</i>	Area
$\alpha$	Non-dimensional area
<i>c</i>	Strut chord
$h_{in}$	Duct inlet height
<i>L</i>	Length
<i>R</i>	Radius
<i>r</i>	Non-dimensional radius
<i>t</i>	Strut thickness

---

$\Delta R$	Radial Offset
$C_p$	Static pressure coefficient
$DC$	Secondary Flow Distortion Coefficient
$DP/P$	Total pressure loss coefficient
$S_{io}$	Non-uniformity index
$\varepsilon$	Duct effectiveness
$\omega$	Total pressure loss coefficient
$C_f$	Skin friction coefficient
$C_p$	Specific heat under constant pressure
$C_v$	Specific heat under constant volume
$e$	Energy
$h$	Enthalpy
$I$	Turbulence Intensity
$k$	Kinetic Energy
$\dot{m}$	Mass Flow Rate
$M$	Mach number
$P$	Pressure
$R$	Universal gas constant
$Re$	Reynolds Number
$T$	Temperature
$U$	Velocity
$u$	Time-varying component of velocity
$u^+$	Near wall velocity
$y^+$	Non-dimensional wall distance
$\gamma$	Gas constant
$\delta$	Boundary layer thickness
$\Delta y$	Wall distance
$\varepsilon$	Dissipation energy
$\lambda$	Thermal conductivity
$\mu$	Dynamic viscosity
$\rho$	Density
$\tau_w$	Wall shear stress
$\omega$	Dissipation rate

## List of Tables

Table 2.1 Typical values of geometric parameters [12].	10
Table 3.1 Characteristics of examined turbofan engines.	25
Table 3.2 Main geometric parameters of the analyzed engines.	27
Table 3.3 Coefficients of the radius distribution.	28
Table 3.4 Coefficients of the area distribution.	31
Table 4.1 Basic Dimensions of GE90's duct.	47
Table 4.2 Grid Independence Study.	48
Table 4.3 Pressure Losses for different $y^+$ .	48
Table 4.4 Calculated Boundary Conditions.	49
Table 4.5 Results for Mach and losses.	50
Table 5.1 Reference Values.	54
Table 5.2 Losses Factor for different $a_2$ shroud.	55
Table 5.3 Variation of loss factor with $\Delta R/L$ .	60
Table 5.4 Variation of loss factor with $h_{in}/L$ .	63
Table 5.5 Variation of loss factor with $R_{min}/L$ .	66
Table 5.6 Variation of loss factor with mass flow rate.	68
Table 5.7 Cases examined for the validation of the model.	72
Table 5.8 Input Parameters for Case 1.	72
Table 5.9 Reference Pressure losses and exponent of Case 1.	72
Table 5.10 Comparison of $DP/P$ at design point for Case 1.	72
Table 5.11 Comparison of $DP/P$ at off-design points for Case 1.	73
Table 5.12 Comparison of exponent for Case 1.	73
Table 5.13 Comparison of $DP/P$ at design point and exponent for Case 2.	74
Table 5.14 Comparison of $DP/P$ at off-design points for Case 2.	74
Table 5.15 Comparison of $DP/P$ at design point and exponent for Case 3.	75
Table 5.16 Comparison of $DP/P$ at off-design points for Case 3.	75
Table 5.17 Comparison of $DP/P$ at design point and exponent for Case 4.	75
Table 5.18 Comparison of $DP/P$ at off-design points for Case 4.	76

# List of Figures

Figure 1.1 Annual growth of global air passengers from 2004 to 2021 [1].	1
Figure 1.2 Worldwide air freight traffic from 2004 to 2021 [2].	2
Figure 2.1 Components of Turbofan Engines [3].	4
Figure 2.2 Historical Growth in engine bypass ratio [5].	5
Figure 2.3 Engine Efficiency trend related to bypass ratio [4].	6
Figure 2.4 Historical Growth of Pressure Ratio [5].	6
Figure 2.5 Historical Growth of Turbine Inlet Temperature [5].	6
Figure 2.6 Schematic of the Intermediate Compressor Duct [6].	7
Figure 2.7 Empirical Range of Total Pressure Loss Factor and Mach number [8].	8
Figure 2.8 Main geometrical parameters of S-shaped Duct [7], [10].	9
Figure 2.9 Different duct lengths examined in [14].	11
Figure 2.10 Separation regions for reduced lengths [14].	11
Figure 2.11 Axial Static Pressure Coefficient Distribution [16].	12
Figure 2.12 Flow Evolution Within the Duct [19].	12
Figure 2.13 Flow Phenomena Due to OGV Wakes [7].	14
Figure 2.14 Schematic of duct pressure fields around strut [22].	15
Figure 2.15 Secondary Flow (a)Strut Leading Edge (b)Strut Trailing Edge (c)Downstream [10].	15
Figure 2.16 Streamline distribution for swirling inlet flow [6].	17
Figure 2.17 Optimization Flowchart [27].	18
Figure 2.18 Hub wall parameterization [14].	19
Figure 2.19 Axial shape parameterization [12].	19
Figure 2.20 Non axisymmetric endwall contouring (Red: uplift, Blue: lowering) [14].	20
Figure 2.21 Pareto Fronts for the integrated systems [31].	21
Figure 2.22 Duct with splitter blade [29].	21
Figure 2.23 Schematic for the location of bleed pipe [33].	22
Figure 3.1 Digitized Points along the (a) Hub and (b) Shroud of GE90.	25
Figure 3.2 Comparison of digitized and real duct's geometry for GE90.	26
Figure 3.3 S-Duct geometry acquired by digitization for GE90.	26
Figure 3.4 Non dimensional shroud radius distribution.	29
Figure 3.5 Non dimensional hub radius distribution.	29
Figure 3.6 Linear correlation between shroud and hub's coefficients.	30
Figure 3.7 Comparison of Estimated and real duct's geometry.	30
Figure 3.8 Non dimensional area distribution along the duct.	32
Figure 3.9 Comparison of estimated and real duct's area distribution.	32
Figure 4.1 3D model of the duct's 10° sector.	35
Figure 4.2 Menu of mesh controls.	36
Figure 4.3 Selection of Mesh method.	37
Figure 4.4 Selection of boundary surfaces.	37
Figure 4.5 Defining the inflation options.	38

Figure 4.6 Mesh sizing options. ....	39
Figure 4.7 Match control options.....	40
Figure 4.8 Definition of cylindrical coordinate system.....	40
Figure 4.9 Definition of fluid properties.....	41
Figure 4.10 Selection of the heat transfer model. ....	41
Figure 4.11 Selection of the turbulence model. ....	42
Figure 4.12 Boundary conditions for duct walls. ....	42
Figure 4.13 Conditions at the periodic interface.....	42
Figure 4.14 Inlet boundary conditions. ....	43
Figure 4.15 Outlet boundary conditions. ....	43
Figure 4.16 Fluid domain with the boundary conditions visible. ....	44
Figure 4.17 Selection of advection scheme. ....	45
Figure 4.18 Selection of residual type and target. ....	45
Figure 4.19 Definition of additional planes.....	46
Figure 4.20 Definition of expressions. ....	46
Figure 4.21 Sketch of the modelled duct and its dimensions.....	47
Figure 4.22 Grid Independence Study. ....	48
Figure 4.23 Generated Mesh. ....	49
Figure 4.24 Mesh inflation near the wall.....	49
Figure 4.25 Applied Boundary Conditions. ....	50
Figure 4.26 Velocity (a)Streamlines and (b)Contour.....	51
Figure 4.27 (a)Total Pressure and (b)Static Pressure Distribution.....	51
Figure 4.28 Static Pressure Coefficient Distribution. ....	52
Figure 4.29 Velocity Profiles. ....	52
Figure 4.30 $Y^+$ distribution. ....	53
Figure 5.1 Duct's shapes for different $a2shroud$ . ....	55
Figure 5.2 Streamlines for $a2shroud$ (a) -0.63, (b)-0.4, (c)-0.1, (d)0.5. ....	56
Figure 5.3 Correlation of $DP/P$ and $a2shroud$ . ....	57
Figure 5.4 Streamlines for (a)80%, (b)100%, (c)150%, (d)200% of duct's reference length. ....	58
Figure 5.5 Streamlines for (a)120%, (b)100%, (c)50% of reference radial offset. ....	59
Figure 5.6 Correlation of $DP/P$ and $\Delta R/L$ for different $a2shroud$ . ....	60
Figure 5.7 Correlation of $DP/P$ and $\Delta R/L$ . ....	61
Figure 5.8 Streamlines and $C_p$ distribution for (a)62%, (b)100%, (c)124%, (d)139% of $hin/Lref$ . ....	62
Figure 5.9 Correlation of $DP/P$ and $hin/L$ for different $a2shroud$ . ....	63
Figure 5.10 Correlation of $DP/P$ and $hin/L$ . ....	64
Figure 5.11 Streamlines for ducts with (a)88%, (b)100%, (c)125% of $Rmin/Lref$ . ....	65
Figure 5.12 Correlation of $DP/P$ and $Rmin/L$ for different $a2shroud$ . ....	67
Figure 5.13 Correlation of $DP/P$ and $Rmin/L$ . ....	67
Figure 5.14 Correlation of $DP/P$ and $m$ for different $a2shroud$ . ....	69
Figure 5.15 Comparison of generated curve to the commonly used one for $a2shroud = -0.2$ . ....	69
Figure 5.16 Variation of Exponent with $a2shroud$ . ....	70
Figure 5.17 Schematic representation of the developed model. ....	71
Figure 5.18 Comparison of curves generated by the model and the CFD results for Case 1. ....	73
Figure 5.19 Comparison of curves generated by the model and the CFD result for Case 2. ....	74
Figure 5.20 Comparison of curves generated by the model and the CFD result for Case 3. ....	75
Figure 5.21 Comparison of curves generated by the model and the CFD result for Case 4. ....	76

---

Figure 5.22 Diagram for variation of $a2shroud$ and different $m$ .....	77
Figure 5.23 Non-Dimensional diagram for variation of $a2shroud$ .....	78
Figure 5.24 Diagram for variation of length and $m = 100kg/s$ .....	79
Figure 5.25 Diagram for variation of length, different $m$ and $a2shroud = 0.3$ .....	79
Figure 5.26 Duct's Shapes for 100% $L_{ref}$ and different mass flow rates.....	80
Figure 5.27 Different geometries produced for varying $R_{hub}/R_{shroudin}$ .....	80
Figure 5.28 Diagram for variation $R_{hub}/R_{shroudin}$ and $m = 100kg/s$ .....	81
Figure 5.29 Diagram for variation $R_{hub}/R_{shroudin}$ , different $m$ and $a2shroud = 0.3$ .....	81
Figure 5.30 Different geometries produced for varying $R_{hub}/R_{shroudout}$ .....	82
Figure 5.31 Diagram for variation $R_{hub}/R_{shroudout}$ and $m = 100kg/s$ .....	82
Figure 5.32 Diagram for variation $R_{hub}/R_{shroudout}$ , different $m$ and $a2shroud = 0.3$ .....	82
Figure 5.33 Different geometries produced for varying $Min$ .....	83
Figure 5.34 Diagram for variation $Min$ and $m = 100kg/s$ .....	84
Figure 5.35 Diagram for variation $Min$ , different $m$ and $a2shroud = 0.3$ .....	84
Figure 5.36 Different geometries produced for varying $Mout$ .....	85
Figure 5.37 Diagram for variation $Mout$ and $m = 100kg/s$ .....	85
Figure 5.38 Diagram for variation $Mout$ coinciding for different $m$ and $a2shroud = 0.3$ .....	85

# Chapter 1 Introduction

## 1.1 Review of Air Transports' Evolution

Air transport sector is one of the most rapidly growing transport sectors, moving more than 4 billion passengers and 50 million tons of freightage per year. By 2035, it is estimated that both passenger traffic and freight volume should be doubled, according to the International Civil Aviation Organization (ICAO), with a growth rate of approximately 6% per year. The main reasons for this increase in air traffic are the economic and demographic growth alongside with the rise in global carrying capacity. According to the International Air Transport Association (IATA), the total value of cargo transported during 2020 was \$128.2 billion, while the revenues from passenger flights were estimated around \$600 billion in 2019. It is clear that aviation contributes significantly to international economic prosperity and to the development of world trade.

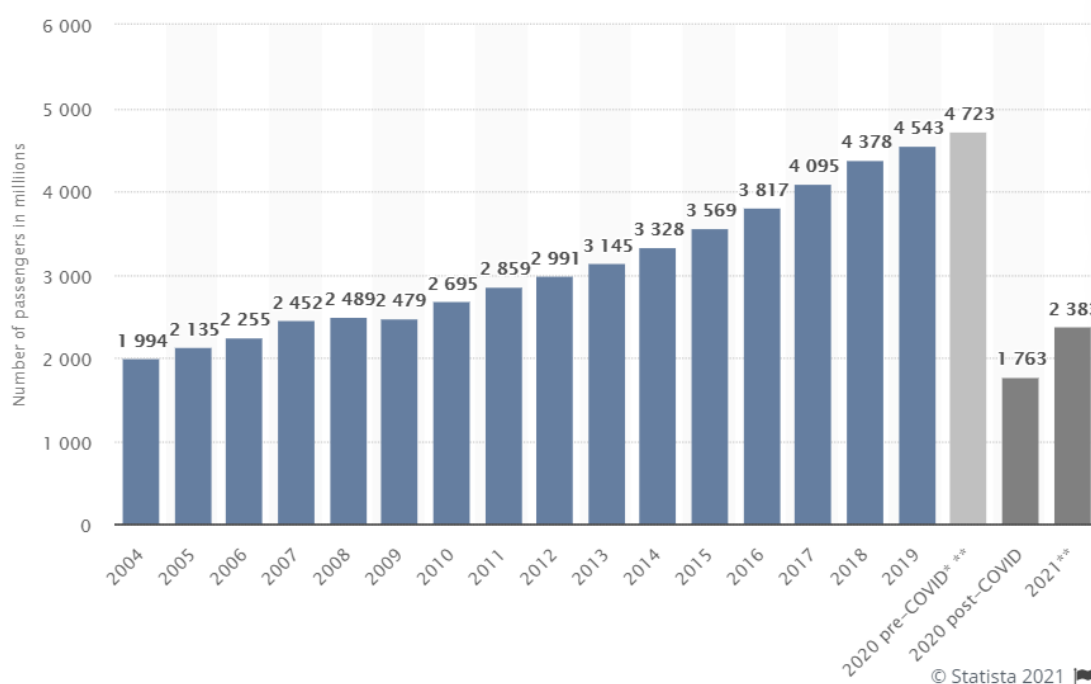


Figure 1.1 Annual growth of global air passengers from 2004 to 2021 [1].



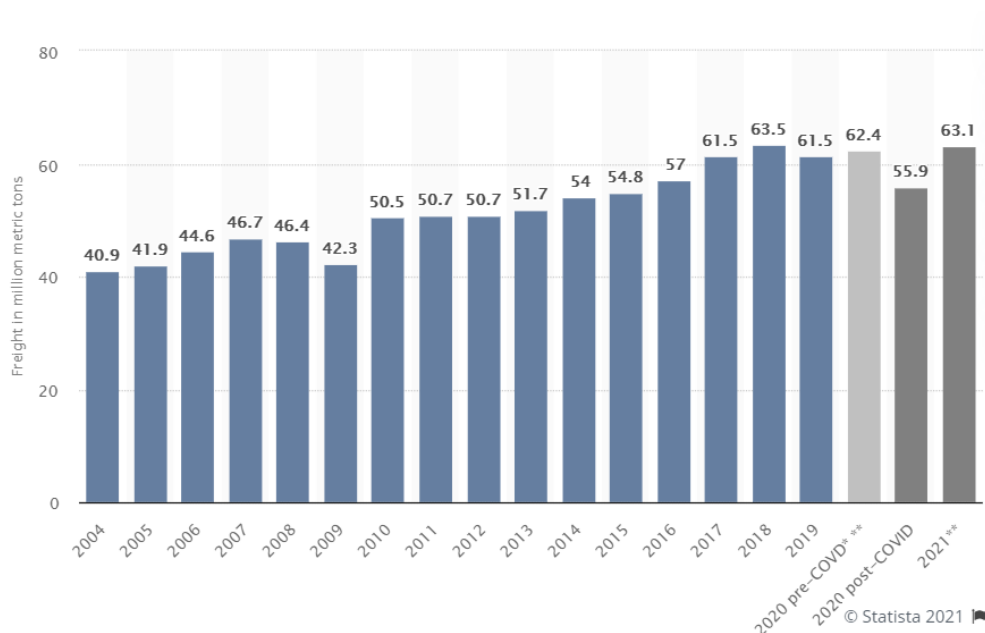


Figure 1.2 Worldwide air freight traffic from 2004 to 2021 [2].

This growth of air traffic over the last decades, has led to an increase in the environmental impact of aviation. More specifically, aviation is responsible for 12% of the CO<sub>2</sub> emissions from all transport sources, with the goal of reducing the net carbon emissions by 50% until 2050, as mentioned by the Air Transport Action Group (ATAG). The target of the industry was to improve the aircrafts' fuel efficiency by 1.5%, until 2020, in order to reach this goal over \$1 trillion were spent to purchase new aircrafts. Nevertheless, the high cost of these purchases makes this solution unviable, considering the rising demand in the sector. Thus, to make air transport more sustainable continuous performance improvements of the already existing aircrafts and engines are needed.

Most of the aircrafts designed over the last 40 years are powered by gas turbine engines, mostly turbofan or turboprop engines. The efficiency of such engines has been improved remarkably, especially due to the use of computational methods, such as Computational Fluid Dynamics (CFD). These methods have made it possible to design turbofan engines of higher bypass and overall pressure ratio, leading to high efficiencies, higher aircraft velocities and low noise levels. However, further efficiency improvements are now harder to achieve for the individual engine components and industry is now focusing on more integrated design processes, taking into consideration the interactions between components.

## 1.2 Thesis Purpose and Outline

In the present diploma thesis, a model for the estimation of the pressure losses across the S-shaped intercompressor duct of turbofan engines is developed, based on the results of

flow simulations conducted with ANSYS CFX. The purpose of this model is to simplify the process of loss factors' approximation, including the influence of the duct's geometric parameters and thus providing more accuracy than merely using the empirical values. Such a model requires as inputs the variables that could be used to effectively describe the geometry of the S-shaped duct. As a result, an inextricable part of this work is devoted to the development of the parametrization process for the ducts of digitized, existing turbofan engines. A detailed outline of the work presented in the following chapters, is given below.

In **Chapter 2**, an introduction to the specifications of the modern turbofan engines and the role of the intermediate compressor duct is made. The most important factors that influence the performance of the S-shaped ducts, such as the wall curvature and the inlet flow, as well as the expected flow phenomena within it, are explained. In addition, the methods proposed in bibliography for the optimization of its performance are presented.

**Chapter 3** is dedicated to the description of the digitization and parametrization processes. More specifically, the data acquired by the digitization of existing turbofan engines are presented and used to determine the necessary variables for the reconstruction of the ducts' geometries. Furthermore, two parameterization procedures, with different inputs, are proposed.

In **Chapter 4**, the settings applied in ANSYS CFX to conduct the flow simulations are shown. The generation of the mesh, as well as, the selection of the turbulence model, its variables and the boundary conditions are presented in detail. The parameters used for the post processing are also demonstrated. In the last Section of the chapter the flow simulation for the base case duct and the results obtained are analyzed.

In **Chapter 5**, the process followed for the development of the model is explained. The influence of the different parameters on the total pressure losses is examined and the expressions used for the correlations observed are derived. These expressions combined are implemented for the loss estimation. The model is validated, and the selection of the input parameters to minimize the duct's losses, based on the model's results, is discussed.

Finally, in **Chapter 6** the main conclusions derived from this diploma thesis and some of the possible future uses of the model are presented.

## Chapter 2 Intermediate Compressor Duct

### 2.1 Modern Aircraft Engines

Modern high bypass ratio turbofan engines consist of six major aerodynamic components. The fan is located in the engine inlet and it draws the air flow inside the engine, from which 80-90% is exhausted through the fan nozzle to provide most of the thrust. The rest of the air is led to the engine's core and is either mixed with fuel and burned in the combustor or it is used for cooling. In the front part of the core, the low (LPC), intermediate (IPC) and high-pressure (HPC) compressors are located and through them the compressed air is guided to the combustion chamber (CC), where the fuel is injected, and the mixture is ignited. The energy of the exhaust gases is extracted in the high (HPT), intermediate (IPT) and low-pressure (LPT) turbines and it is mainly used to generate the mechanical energy that turns the shafts and drives the compressors. Finally, the core flow exits from a nozzle, either separately or mixed with the bypass flow. The primary difference between the turbofan and turboprop is that the latter uses a propeller in free air to produce thrust rather than the fan in the engine nacelle.

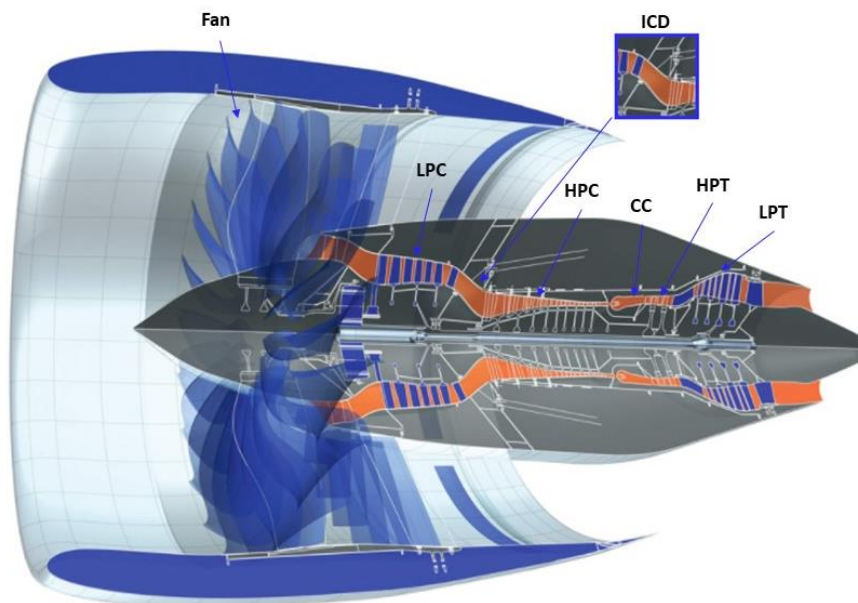
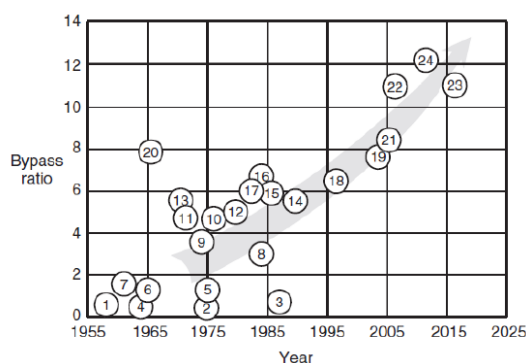


Figure 2.1 Components of Turbofan Engines [3].

The number of compressors and turbines, as well as the connection between them, depend on the spool configuration of the engine. In a two-spool or boosted two-spool turbofan engine, both LPC and the Fan are attached to the low-pressure spool, which is rotated with lower angular velocity, driven by LPT, while HPT is responsible for the rotation of HPC. Typical examples of twin spool turbofan engines are GE90, CF6, JT9D and PW4000. In a three-spool engine configuration, commonly used by Rolls-Royce, an intermediate pressure spool is used to connect IPC and IPT. Another variant of the conventional turbofan engine is the geared turbofan, like TFE731 and PW1000G. In this configuration a reduction gearbox is installed between the Fan and the LPC to allow the first to turn at a different rotational speed. The gearbox is designed to optimize the speed of all components resulting in the need of fewer compressor and turbine stages.

Many of the parts of aircraft engines have been individually optimized in order to improve the overall efficiency of the engine. Overall efficiency refers to the efficiency with which the engine converts the power in the fuel flow to propulsive power, as it is clearly stated in [4]. The efficiency is the product of thermodynamic or thermal efficiency and propulsive efficiency, which correspond to the efficiency of the conversion of fuel flow to shaft power and the conversion of shaft power to propulsive power, respectively.

A more efficient engine means lower fuel consumption and as a result reduced emissions. The bypass ratio (BPR) is inextricably linked with the concept of efficiency, as the higher the ratio the more efficient the engine. This ratio indicates how much air, entering the nacelle, passes through the combustor and how much is directed to the fan nozzle. As it is described in Figure 2.2 the BPR has risen dramatically over the years, from around 2:1 in the 1960s, to 12:1 in PW1000G. A similar rise can be observed in the efficiencies, in Figure 2.3.



LEGEND			
1 RR Conway	7 PW JT3D	13 PW JT9D	19 RR Trent900
2 GE F404	8 RR Tay	14 IAE V2500	20 GE TF39
3 E.J200	9 TFE331	15 CFM56	21 GE90
4 RR Spey	10 RR RB211-584	16 PW2037	22 RR Trent1000
5 PW F100	11 RR RB211	17 GE CF6	23 CFM LEAP-X
6 PW JT3D	12 GE CF34	18 PW4077	24 PW1000G

Figure 2.2 Historical Growth in engine bypass ratio [5].

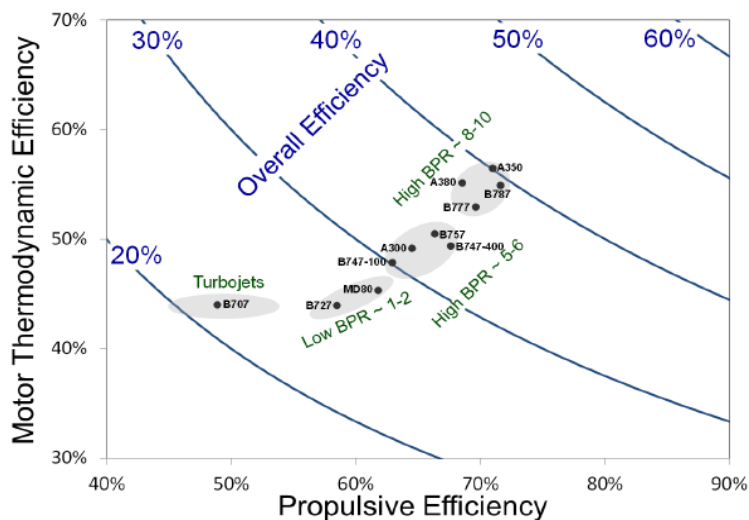
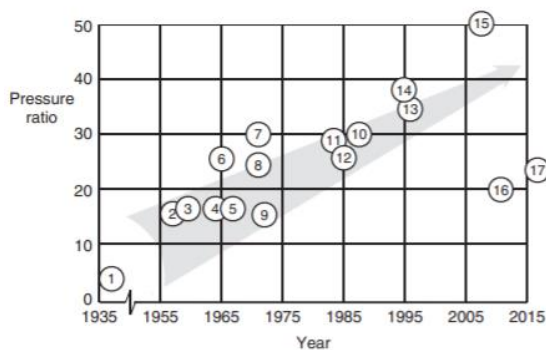


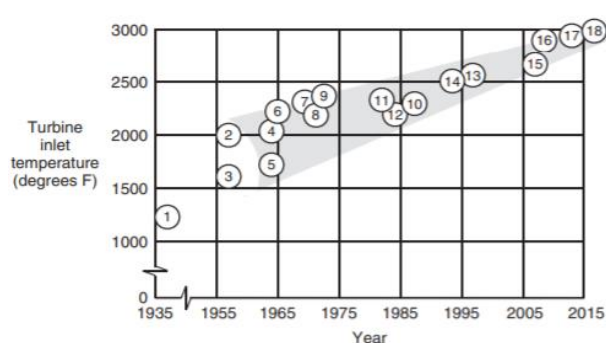
Figure 2.3 Engine Efficiency trend related to bypass ratio [4].

Other parameters that affect the efficiency of turbofans are the overall pressure ratio (OPR) and the turbine inlet temperature (TIT). These are the principal cycle design parameters for any gas turbine, and their values have increased significantly through the years, as shown in Figure 2.4 and Figure 2.5.



Legend		
1 Whittle	7 GE CF6	13 PW 4084
2 RR Conway	8 PW JT9D	14 GE90
3 PW JT3D	9 TFE731	15 RR Trent1000
4 RR Spey	10 IAE V2500	16 PW 1000G
5 PW JT8D	11 RB211-524	17 CFM LEAP
6 GE TF39	12 PW 2037	

Figure 2.4 Historical Growth of Pressure Ratio [5].



LEGEND		
1 Whittle	7 GE CF6	13 PW 4084
2 RR Conway	8 PW JT9D	14 GE90
3 PW JT3D	9 TFE731	15 RR Trent900
4 RFSpey	10 IAE V2500	16 RR Trent1000
5 PW JT8D	11 RB211-524	17 PW 1000G
6 GE TF39	12 PW 2037	18 CFM LEAP

Figure 2.5 Historical Growth of Turbine Inlet Temperature [5].

The aerodynamic components and the concepts discussed above have been already studied and improved to a great extent. However, there has not been as much focus on optimizing auxiliary and stationary components, such as intermediate ducts, located between the compressors and the turbines of the engine.

## 2.2 The Intermediate Compressor Duct

The intermediate compressor duct (ICD) is an annular duct located between the LPC and the HPC. The purpose of this duct is to guide the flow from the larger exit radius of the low-pressure system to the smaller inlet radius of the high-pressure system. The shape usually resembles to an “S”, that is the reason why it is called S-Shaped or Swan Neck Duct. Stationary blades, called struts, can be integrated inside the duct aiming to provide structural support as well as oil and cooling services.

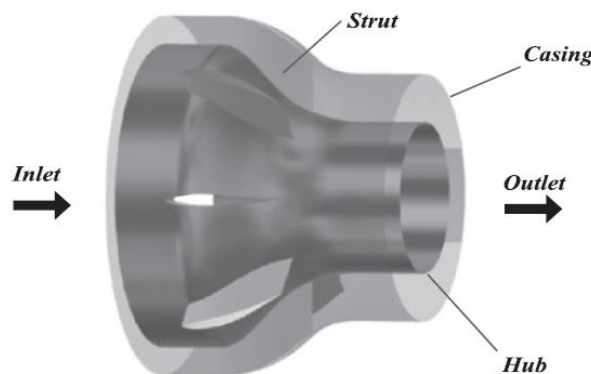


Figure 2.6 Schematic of the Intermediate Compressor Duct [6].

While designing and optimizing an S-shaped ICD there are many different parameters to be considered. The duct should force the air flow through the radial offset within the shortest possible axial length, because of the engine’s weight and size penalties. Additionally, in modern turbofan engines, due to higher bypass ratios, the radial offset of the duct is larger, which means that there is need for more aggressive ICDs. Ideally, as it is mentioned in [7], all of the radius change should be achieved in the duct while maintaining the upstream compressor’s radius constant, with the purpose of reducing the loading of the compressor stages and increasing the overall spool efficiency. In this kind of aggressive ducts, strong adverse pressure gradients are developed making the flow prone to separation. However, the flow at the exit of the duct should be as undisturbed as possible to avoid mechanical vibrations, increased losses and unexpected surge in the downstream compressor.

## 2.3 Performance Parameters of Intermediate Duct

To quantify the performance of S-shaped ducts a set of non-dimensional parameters is commonly used. The most widely used ones are the static pressure and the stagnation pressure loss coefficients. The coefficient of static pressure  $C_p$  expresses the energy transformation within the passage and is calculated in (2.1). The total or stagnation pressure loss coefficient,  $\lambda$ ,  $\omega$  or  $Y_p$ , depicts the amount of total pressure lost due to the turbulent and viscous effects and is defined in (2.2).

$$C_p = \frac{P_s - \tilde{P}_{sref}}{\tilde{P}_{tref} - \tilde{P}_{sref}} \quad (2.1)$$

$$\omega = \frac{\tilde{P}_{tin} - \tilde{P}_{tout}}{\tilde{P}_{tin} - \tilde{P}_{sin}} \quad (2.2)$$

As the reference pressure it could be used the one at the inlet of the duct. In both expressions the denominator stands for the dynamic pressure, which in this case cannot be expressed with the use of the flow velocity. The stagnation and static pressures used, noted as  $\tilde{P}$ , are derived by mass weighting the appropriate values.

$$\tilde{P} = \frac{1}{m} \int P dm \quad (2.3)$$

The total pressure losses can also be expressed as a fraction of the total pressure at the inlet of the duct, as seen in (2.4).

$$\frac{DP}{P} = \frac{\tilde{P}_{tin} - \tilde{P}_{tout}}{\tilde{P}_{tin}} \quad (2.4)$$

The suggested range of the pressure loss factors is shown in Figure 2.7.

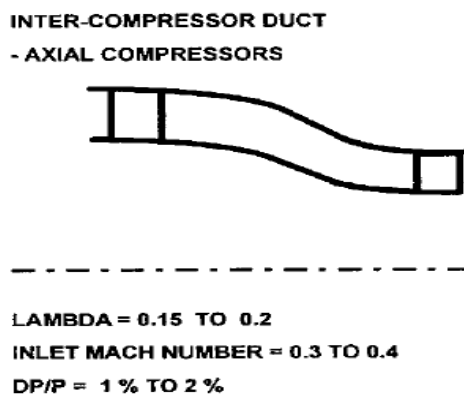


Figure 2.7 Empirical Range of Total Pressure Loss Factor and Mach number [8].

In literature the ideal static pressure coefficient  $C_{pi}$  corresponding to the pressure recovery of an ideal frictionless and uniform duct flow, is calculated based on the area ratio  $AR$  of the duct. The comparison of the ideal and the real static pressure coefficients indicates the effectiveness of the duct  $\varepsilon$ , shown in (2.6).

$$C_{pi} = 1 - \frac{1}{(AR)^2} \quad (2.5)$$

$$\varepsilon = \frac{C_p}{C_{pi}} \quad (2.6)$$

Furthermore, in order to quantify the amount of flow distorted at a specified location due to the existence of secondary flow the distortion coefficient is used. In (2.7)  $\bar{P}$ ,  $\bar{q}$  indicate the mean values of total pressure and dynamic pressure and  $\phi$  represents the degrees of the sector examined.

$$DC = \frac{\bar{P}_{tout} - \bar{P}_{tout}(\phi)}{\bar{q}} \quad (2.7)$$

Non-uniformity index is often used to describe the percentage of secondary flow in a region within the duct. It is calculated based on the non-axial velocities at the location.

$$S_{io} = \frac{(\sum \sqrt{V_y^2 + V_z^2})}{nU_{avg}} \quad (2.8)$$

Finally, in some cases, as in [9] the swirl angle, defined as the ratio between the tangential and the axial components of the velocity vector, can be used to describe the flow at the inlet and the exit plane of the duct.

## 2.4 Fundamental Factors Affecting S-Duct Performance

The flow physics within the S-shaped duct has been examined by several researchers. As it is explained in literature, flow within the annular ICD is influenced by wall curvature, the existence of struts, the wakes produced by the upstream compressor, turbulence, Reynolds number and inlet flow conditions.

### 2.4.1 Duct Geometry

The main geometrical parameters that affect the performance of the intermediate compressor duct is the radial offset  $\Delta R$ , which can also be described by the angle of turn  $\alpha$ , the exit area ratio  $AR$ , the inlet duct height  $h_{in}$ , the aspect ratio, defined as length to diameter ratio, and the axial length of the duct.

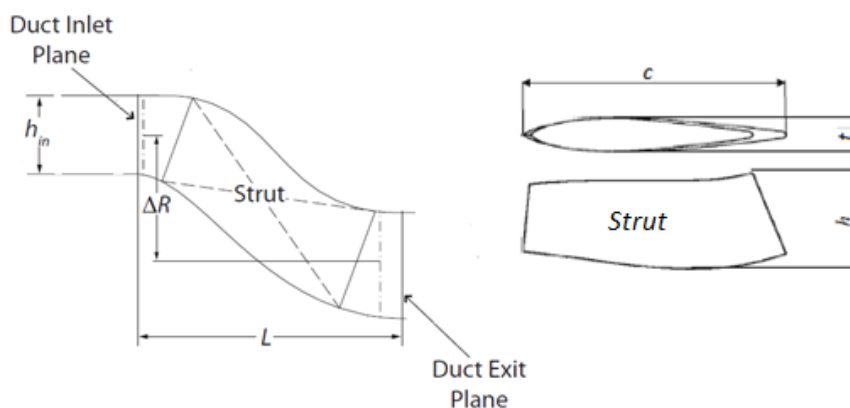


Figure 2.8 Main geometrical parameters of S-shaped Duct [7], [10].



Usually, these parameters are used in a non-dimensional form to express the aggressiveness of the duct. More specifically, as described by Walker et al. in [11] the radius change  $\Delta R/L$  reflects the severity of the curvature responsible for the development of the pressure gradients. The area ratio  $A_{ex}/A_{in}$  shows the expected acceleration of the fluid through the duct or deceleration when it is referred to a diffuser. The non-dimensional length  $L/h_{in}$  indicates the axial pressure gradient that is expected to appear in the duct. Finally, for the description of the geometry of the strut the thickness to chord ratio  $t/c$  is used. The aggressiveness of the duct, and thus the chance of separation, is increasing by reducing the length, raising the radial offset or using struts with higher thickness to chord ratio. The typical values for ducts used in current engines are shown in Table 2.1.

Parameter	Typical Value
$\Delta R/L$	0.30-0.45
$h_{in}/L$	0.1-0.3
$r_{in}/L$	1.5-1.7
$t/c$	0.14-0.30
$A_{ex}/A_{in}$	0.6-0.7

Table 2.1 Typical values of geometric parameters [12].

The effect of length on the performance of S-shaped ducts has been investigated by Duenas et al. [13]. The authors examined three different duct lengths, 100%, 74% and 64%, and aimed at finding the optimum turning angle to minimize the pressure loss. It was found that as the duct becomes shorter the loss is more sensitive to the geometric turning angle with the flow in the duct with 64% of the initial length being always separated. In order to minimize the loss, for each length, it was proven that the lowest duct turning angle that maintains fully attached flow should be chosen. Another interesting conclusion of their study was that the loss associated with the outer wall of the duct was more dependent on the length, even though most of the loss occurred near the inner wall in all the cases.

Sturzebecher et al. in [14] also explored the possibility to shorten the duct and attempted to optimize its shape in order to maintain the loss in low levels. The lengths examined as well as the flow patterns developed in every case are shown in Figure 2.10.

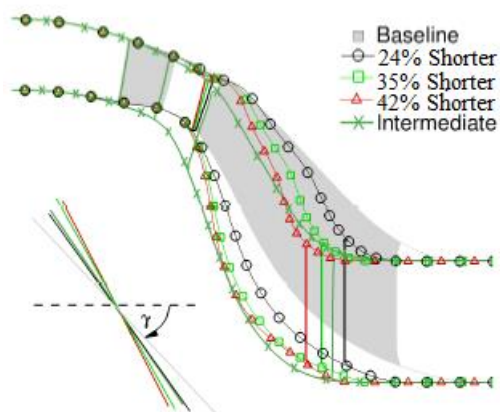


Figure 2.9 Different duct lengths examined in [14].

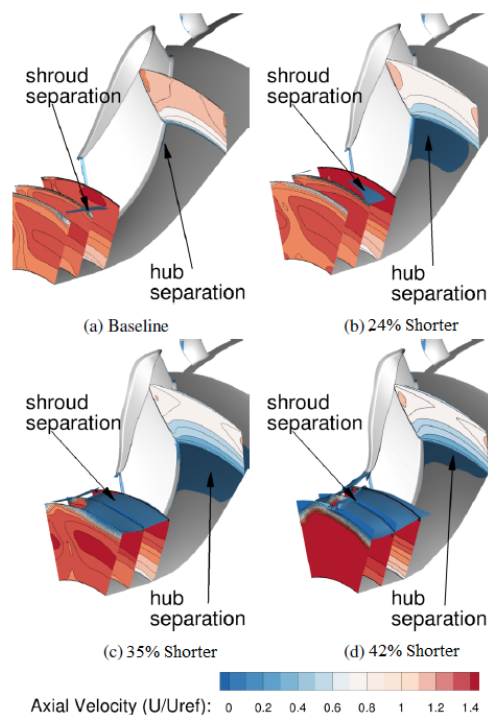


Figure 2.10 Separation regions for reduced lengths [14].

## 2.4.2 Wall Curvature

The inner wall, or hub, of the compressor intermediate duct consists of convex followed by concave curvature and the outer wall, or shroud, is made of concave followed by convex curvature, as shown in Figure 2.11. These curvatures influence significantly the flow developed in the S-shaped duct, as it is underlined by Britchford et al. in [15], because the fluid is subjected to a radial pressure gradient combined with the centrifugal forces developed within the duct.

The radial static pressure gradient occurs due to the adjustment of wall pressure distributions in order to provide the necessary turning forces. Bailey et al in [16] explain that, as the flow approaches the first bend the pressure close to the outer wall gets higher than the one adjacent to the hub, directing the flow towards the latter. This situation is reversed in the second bend of the duct, where the fluid should return to its initial axial direction. This way both streamwise and radial pressure gradients are produced which are responsible for the boundary layer development near the walls and the mixing of the wakes entering the duct from the blades of the upstream compressor. Bradshaw in [17] suggested that, because of the imbalance between the centrifugal acceleration of the fluid and its surrounding pressure field, increased turbulence mixing is observed over the concave surface whereas turbulence levels are significantly lower over the convex curvature, leading to flow separation. The axial variation of static pressure coefficient for various heights across the duct, as evaluated in [16], is presented in Figure 2.11.

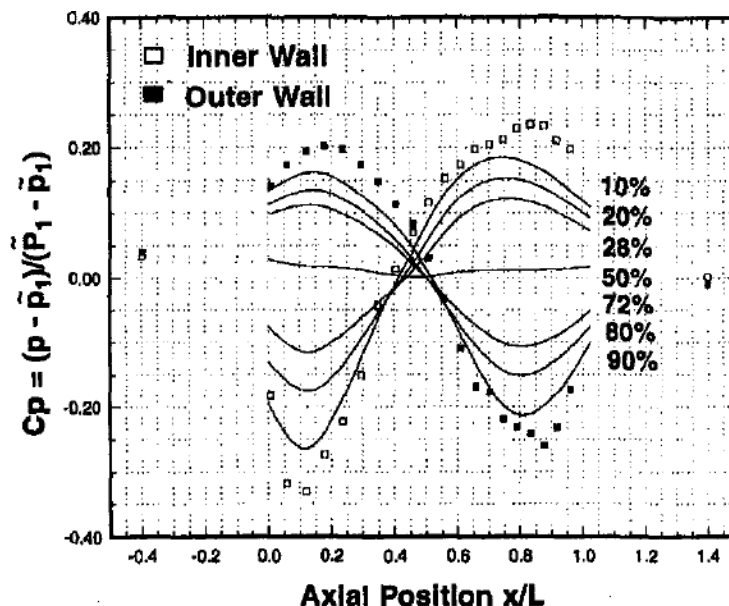


Figure 2.11 Axial Static Pressure Coefficient Distribution [16].

At the same time, the fluid at the central axis of the duct has higher velocity than the one moving in the near wall region, thus, it is subjected to a larger centrifugal force, as mentioned by Ng et al. in [18]. As a result, it moves away from the center of the duct towards the outer wall of the first bend, where, as described above, an adverse pressure gradient exists, forcing the fluid to slow down. Since this, low energy, fluid cannot overcome the pressure gradient, it starts moving around the periphery of the duct and finally towards its center.

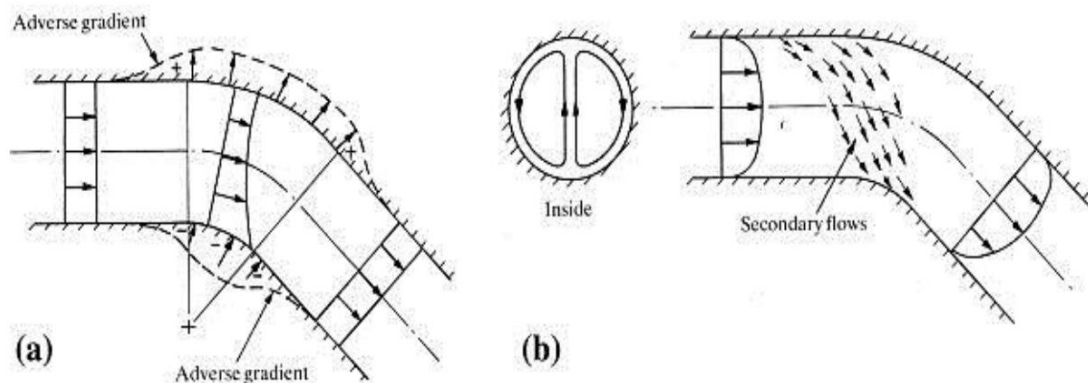


Figure 2.12 Flow Evolution Within the Duct [19].

The secondary flow and the vortices developed induce a high level of total pressure loss, which depends on the curvature as well as on the duct shape. Moreover, Taylor et al. [20] proved that, for S-shaped duct with both square and circular cross sections, the secondary flow formed is larger for laminar flow. This is attributed to the thicker boundary layer of the laminar case, which occupies approximately 25% of the passage height, in comparison with the turbulent layer, which covers 10-20% of the height, depending on the shape of the duct. In all cases boundary layer separation is more likely to occur in the inner wall of the

first bend, where the large adverse pressure gradient is located. Finally, wall curvature affects the flow distortion at the exit of the duct, which can be considered as uniform only if the magnitude of secondary flow is less than 10% of the average velocity [19].

### 2.4.3 Upstream Compressor Stage

The last decades, many researchers tend to adopt an integrated design strategy in order to extend the limits of the design space and explore the possibility of using more aggressive ICDs. Therefore, it is now necessary to examine more engine representative inlet conditions, thus the way the upstream compressor affects the performance of the S-shaped duct.

Britchford et al. in [15], after conducting experiments with a complete compressor stage placed at the inlet of the examined duct, observed that the adverse pressure gradient along the inner wall was significantly lower. Furthermore, the author suggested that the main factors influencing the wall static pressure distribution, except for the ones already discussed in the previous paragraph related to flow curvature, are the inlet kinetic energy flux and the mixing out of the blade wakes. More specifically, the radial pressure gradient at the inlet drives the wake radially inward. The wake fluid also has a total pressure deficit which is, however, lower than the one of the inner wall boundary layer, and it reenergizes it, leading to a reduction in the likelihood of flow separation. This phenomenon suggests that the duct loading could be increased, thus its length shortened, without making it more prone to separation. According to Bailey et al. [16], a slight reduction in the shape parameter, characterizing the boundary layer, along the outer wall can also be noticed due to the higher velocities. Additionally, due to rotor tip leakage effects, a large amount of turbulent energy is observed close to the shroud of the duct.

Although the rapid mixing of the compressor outlet guide vanes' (OGVs) wakes reduces the occurrence of separation, it is responsible for the additional pressure losses measured for the duct. The addition of the inlet compressor stage reduces the losses near the outer wall while close to the hub the pressure losses rise, as mentioned by Karakasis et al. in [7], and a finite loss is present in the center of the duct. Karakasis et al. also investigated the effect of non-axisymmetric endwall profiling for a strutted duct with a compressor stage located upstream of it. The results indicated that non-axisymmetric design suppressed the strut-hub corner separation, which will be analyzed in the next Section, while the pressure loss, related to the wake mixing, increased only by 28%, compared to 54% for the axisymmetric duct.

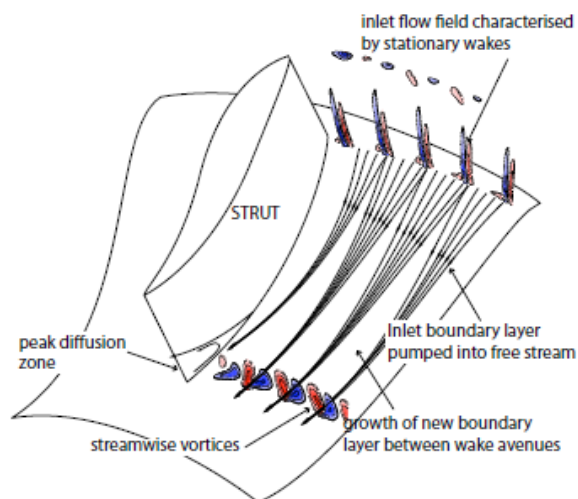


Figure 2.13 Flow Phenomena Due to OGV Wakes [7].

Walker et al. in [21] proposed an approach to integrate OGV into S-shaped duct with the purpose of saving at least 20% of the system's length while keeping the upstream rotor performance unaffected. The OGV row was placed downstream the first bend of the duct, with the produced wakes found throughout the duct passage and not only in the first bend, as it happens when the blade row is outside the duct. Even though the available length for mixing out is reduced it turned out that the level of mixing, the depth of wakes and the level of non-uniformity are quite similar to the simple design. Finally, the OGV loss was slightly reduced with the overall loss remaining at the same levels.

#### 2.4.4 Struts

Many modern compressor transition ducts are occupied with radial struts which have a load-carrying role, against the forces developed from the surrounding components, and can function as paths for some essential engine services. These struts create an aerodynamic blockage to the flow resulting in an additional pressure gradient and to modification in the flow field of the duct.

Naylor et al. in [22] explain that as the flow approaches the strut, placed near the second bend, stagnates. Then the flow is accelerated until it reaches the rear side of the strut, where it is being decelerated. For the shroud the deceleration occurring at the trailing part of the strut takes place in the region where the curvature causes an acceleration of the flow. On the contrast, near the hub wall, in this region curvature causes the flow to slow down and combined with the effect of the strut a large flow deceleration is generated. Consequently, the flow is more likely to separate in the hub-strut corner.

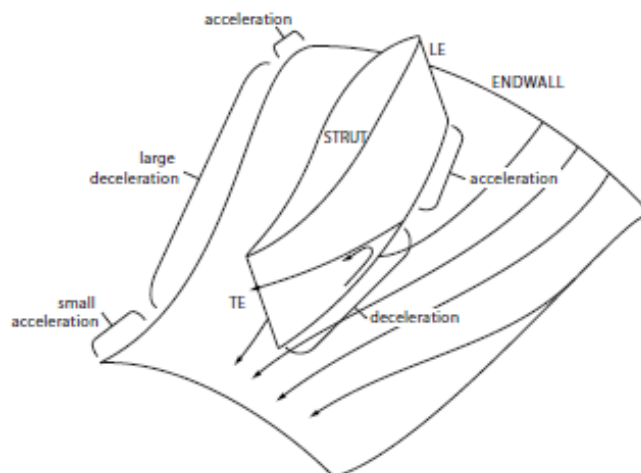


Figure 2.14 Schematic of duct pressure fields around strut [22].

The flow around the strut has been presented with further details by Bu et al. in [10]. It is described that a horseshoe vortex is formed ahead of the strut leading edge near the outer wall, where a stagnant point exists. From this point a separation line emerges and is extended, diverging, downstream the strut. Another similar separation line is formed near the trailing edge of the strut with a larger divergence angle. Near the inner duct wall, the flow pattern is expected to resemble that of the shroud. The secondary flows near the walls turn towards the strut surface forming counter-rotating vortices. The vortex pairs generated develop rapidly along the duct occupying an important percentage of its height, as it is observed in Figure 2.15.

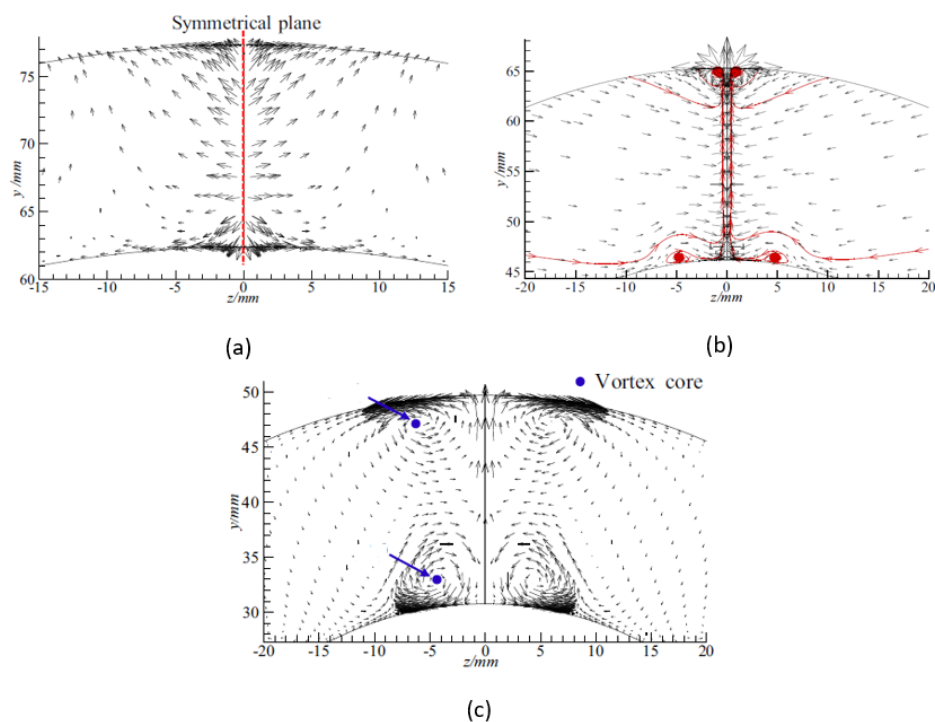


Figure 2.15 Secondary Flow (a)Strut Leading Edge (b)Strut Trailing Edge (c)Downstream [10].

As it is mentioned in [16] the influence of a single strut on the overall performance of the duct is relatively small, causing a rise of approximately 5% to the pressure loss coefficient. However, usually a cascade of struts is installed within the duct, which creates an interaction between them. Sharma and Baloni in [19] underline that the suction side of each strut interacts with the pressure side of the other creating additional vortices which can lead to premature separation of the flow. This phenomenon causes increased losses, as proved in [23], and asymmetric distortions which affect the downstream components.

Walker et al. in [24] examined the integration of lifting, or turning, struts within the duct, which would behave like the outlet guide vane row of the upstream component. Same effects on the flow, as the ones for the simple struts, were observed with the overall duct loading increasing significantly. It should be underlined that the pressure loss rise was not as high compared to the system with a non-turning strut row, including the OGV.

#### 2.4.5 Inlet Flow Conditions

In addition to the factor described above, the flow within the S-shaped transition duct is also sensitive to the inlet conditions, which are determined mostly by the upstream compressor.

One parameter that affects the performance of the duct is the *inlet swirl* of the flow, which is usually attributed to insufficient straightening before entering the S-duct. According to Bailey and Carotte [25], if swirling flow could pass through the intermediate duct the system's length would be reduced and the overall performance improved. They investigated the effects of inlet swirl by removing the OGV row from the upstream compressor stage. As it is explained, due to the swirl, the fluid is subjected to an additional centripetal acceleration with components both in streamwise and normal direction. It was observed that the swirl component of the velocity increased through the duct, as the mean radius is decreased, due to the conservation of tangential momentum. The greatest increase was located near the hub wall, where the relative change of radius is more significant. Moreover, the streamwise pressure gradient along the inner wall of the duct is smaller, indicating that flow separation is less likely to occur. The pressure loss was even higher than the one obtained with OGV, analyzed in the previous paragraphs, and can be attributed to the increased levels of turbulence generated by the swirling flow.

In [6], Gao et al. investigated the way the pre-swirl angle influenced the flow near the duct's struts. It was observed that a backflow region was formed in the leeward side of the strut, as shown in Figure 2.16, which enlarges as the angle is increased. For smaller angles only one clockwise vortex is formed in the surface of the strut with a second, anti-clockwise one appearing for higher angles. The presence of pre-swirl leads to static pressure distortion and thus to non-uniform flow at the exit of the duct. In the same work the effect of *inlet Mach number* on the duct flow was explored. As the Mach number rises a decrease in the total pressure recovery coefficient and exit flow uniformity was noticed. This deterioration

of the duct's performance is attributed to the sharp mixing of the strut wake with the wall boundary layer, resulting in more loss.

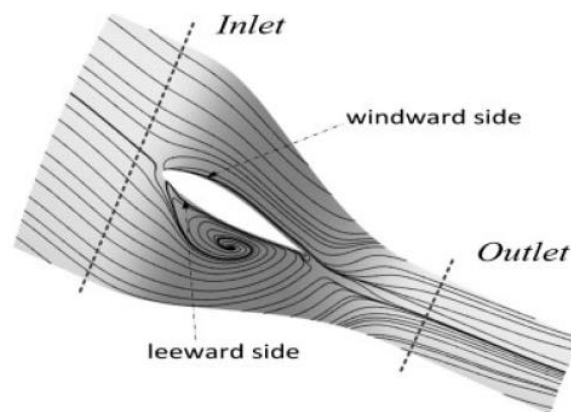


Figure 2.16 Streamline distribution for swirling inlet flow [6].

Another important parameter that has been presented in literature is the **thickness of the inlet boundary layer** (IBL). Sonoda et al. in [26] examined the flow developed within the duct for thin and thick IBL, occupying 5% and 30% of the passage inlet height, respectively. In the case of the thick IBL the thickness of the boundary layers formed near the duct's walls was increased and a vortex pair was observed near the hub wall, leading to a rise in loss. On the other hand, for the thin IBL a single vortex was developed at the same location. The increase in overall pressure loss, due to the different IBL, accounted for almost 30%.

**Reynolds number** ( $Re$ ) is considered to have a less significant impact on the curved duct's performance. More specifically, as mentioned in [13], for a turbulent fully attached boundary layer the pressure loss varies with  $Re^{-1/5}$ . Consequently, a noticeable decrease in duct's pressure recovery for Reynolds numbers higher than  $10^5$ .

## 2.5 Enhancement Techniques

In order to avoid flow separation and enhance the performance of the duct several techniques have been examined, including shape optimization, integrated design methods and the use of flow controlling devices.

### 2.5.1 Shape Optimization

The existing need to continuously increase the efficiency of aircraft engines leads researchers to explore various CFD-based optimization techniques to achieve the design of aggressive S-shaped ducts with minimized pressure loss. Curved ducts are usually parametrized with the non-dimensional parameters mentioned in Section 2.4.1, which should be varied to achieve the optimal performance.



A typical optimization process followed by many researchers is illustrated in Figure 2.17. Experiments are conducted to determine the suitable levels for each of the factors or responses examined. For most of the cases, the objective in Design of Experiments (DOE) are the aerodynamic performance parameters, like the pressure loss coefficient and the flow distortion factor. The Response Surface Methodology (RSM) is used to approximate the multi-variable objective function of the optimization problem. This method can be based on a linear function, as in [22], or on a polynomial one, like in [27]. A Genetic Algorithm (GA) is commonly employed to solve the multi-objective optimization problem. Some researchers also use TABU search algorithm (TS), [28], [29], for the optimization process, since it is designed to be implemented in “difficult regions” of the design space where local minima or infeasible solutions could be located. After the optimization steps a Pareto optimal front is obtained which describes the trade-offs between the parameters of the design problem. The optimal aerodynamic performance of the designed duct can also be predicted by an Artificial Neural Network (ANN), combined with the GA, trained with the use of experimental and CFD results, as suggested in [12].

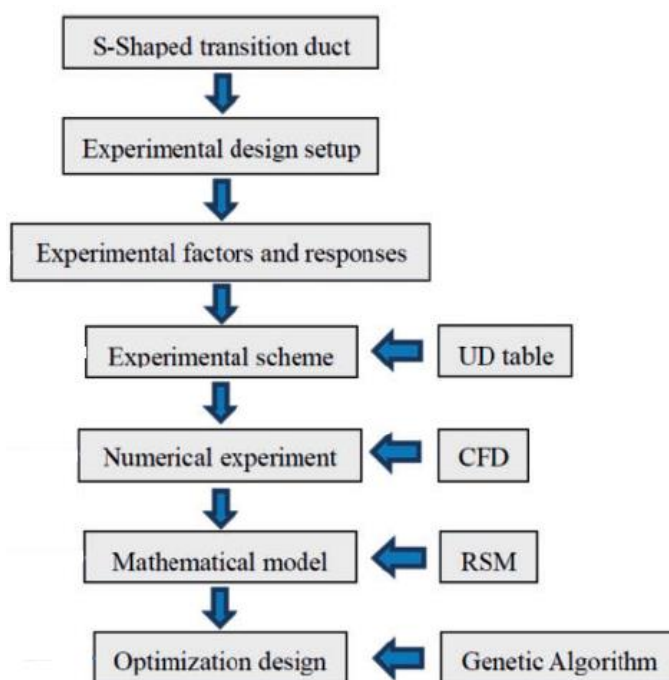


Figure 2.17 Optimization Flowchart [27].

To optimize the shape, and consequently the performance, of the intermediate compressor duct, its geometry should be parameterized. The goal of the parameterization is to reduce the number of variables, and thus to reduce the computational cost of the optimization process. Free Form Deformation (FFD) method is widely used for this purpose. According to this approach the entire geometry can be described by the external surface of the duct and is determined by the position of a few control points. The control points' displacements are subjected to certain constraints based on the tangential condition that should be maintained at the inlet and outlet, as presented in [30].

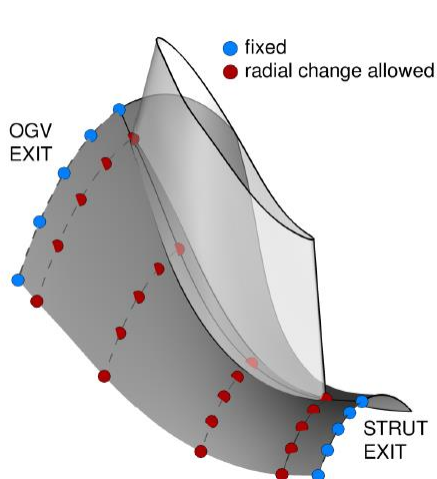


Figure 2.18 Hub wall parameterization [14].

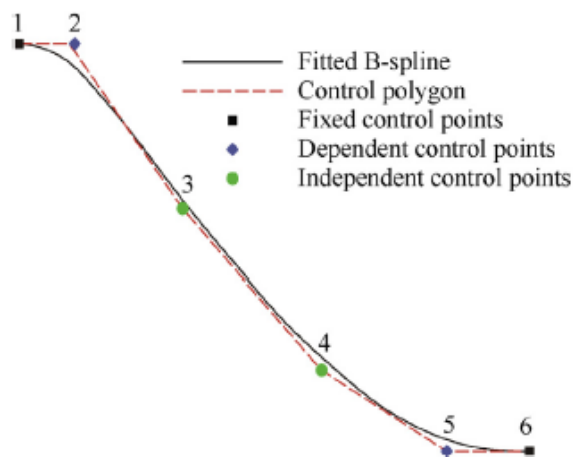


Figure 2.19 Axial shape parameterization [12].

For axisymmetric ducts, Chiereghin et al. [9] predicted that the process could result to a reduction of approximately 20% of the total pressure loss and 10% of the exit swirl, depending on which parameter the optimization is aiming for. D'Ambros et al. in [30] suggested that the decrease in the exit swirl angle of the duct could reach 70%, with the pressure loss remaining at the same level.

Naylor et al. [22] focused on the design of non-axisymmetric duct to minimize the loss caused by the presence of struts. The method used, known as “Area Ruling”, is based on the adjustment of the streamwise area distribution to compensate for the blockage created by struts. Inner and outer walls are moved in the region near the strut to cancel the extra deceleration created, as described in Section 2.4.4. The result was to lower the wall in the front of the duct and raise it in the rear portion, as shown in Figure 2.20. In the optimized duct no reverse flow region was formed on the strut’s surface and the loss associated with strut-hub corner separation was decreased. Overall, the end wall contouring implemented gave the possibility of designing a duct of 34% higher radial offset with only 11% rise in loss, 16% lower than the one of the axisymmetric case for the same  $\Delta R/L$ .

A similar method was followed by Sturzebecher et al. [14] aiming to the axial shortening of the duct and the decrease in losses, expressed by the entropy rise coefficient. It was observed that for the optimized duct the separation regions were limited and located mainly at the trailing edge of the strut and the suction side of the OGVs.

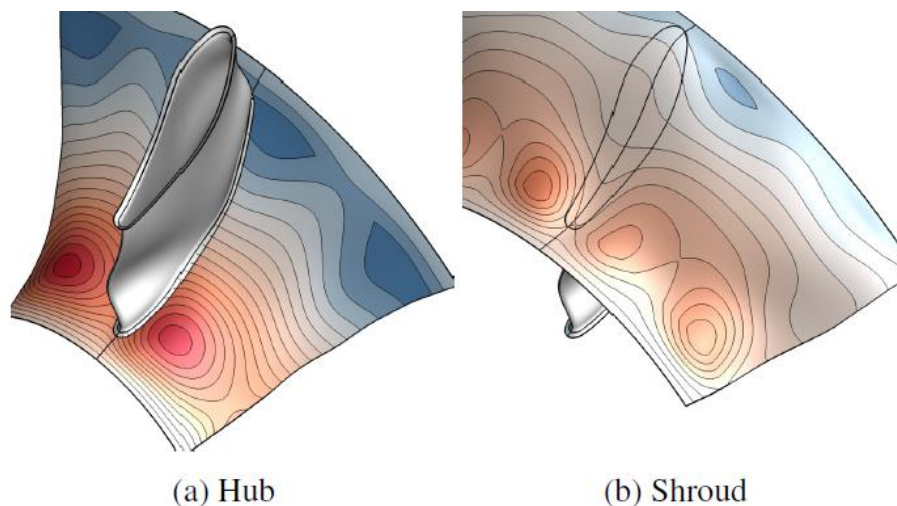


Figure 2.20 Non axisymmetric endwall contouring (Red: uplift, Blue: lowering) [14].

In [7] the endwall profiling was only used for the hub wall. Indeed, as it is demonstrated by Donghai et al. [12], using this technique for the inner wall has similar results as using it for both the inner and the outer walls, with lower computational cost.

### 2.5.2 Integrated Design

In the conventional design method, each module of the aircraft engine is optimized separately, without taking advantage of the systems' interactions. This process leads to limited improvements in the overall efficiency of the engine. However, as Ghisu et al. in [31] suggest, an integrated approach could eliminate the intermodular constraints and expand the limits of the available design space.

In [31] the optimization of the whole core compression system is attempted. More specifically, the compression system examined consisted of the IPC, the S-shaped intermediate duct and the HPC with the optimization variables being the surge margin and the isentropic efficiency of the system. The IPC and the duct were optimized separately, without imposing any constraints on their exit planes, and compared with the results of the integrated optimization. It was observed that in the latter case the performance was improved at the price of a more highly loaded duct. An additional improvement of 0.5% in the system's efficiency could be obtained by incorporating the HPC to it.

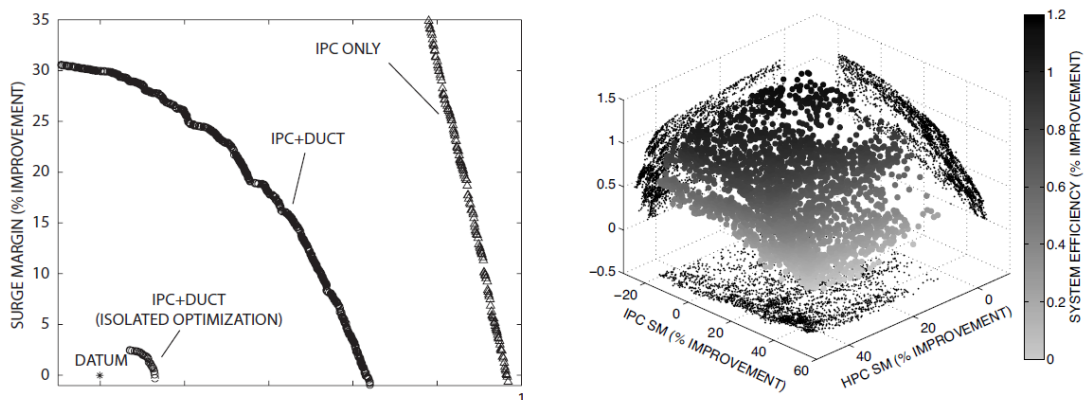


Figure 2.21 Pareto Fronts for the integrated systems [31].

Other designs explored in literature, involve the integration of OGV blades in the transition duct. This approach was investigated by Walker et al. in [21]. The concept of lifting struts, which have both a structural role and replace the OGVs of the low-pressure system, has been proposed in [24]. These ideas are presented in detail in Sections 2.4.3 and 2.4.4, respectively. In both cases the design of a more aggressive S-shaped duct was possible, with the level of losses remaining at the desired levels.

Finally, the integration of a splitter blade within the S-duct was suggested by Taylor et al. in [29]. The circumferential blade could assist to the flow turning, reduce the overall duct loading, prevent strut and endwall separation, aiming to minimize the duct length. The CFD experiments conducted showed that such a design could reduce the duct loss by 20% and lower the distortion coefficient.

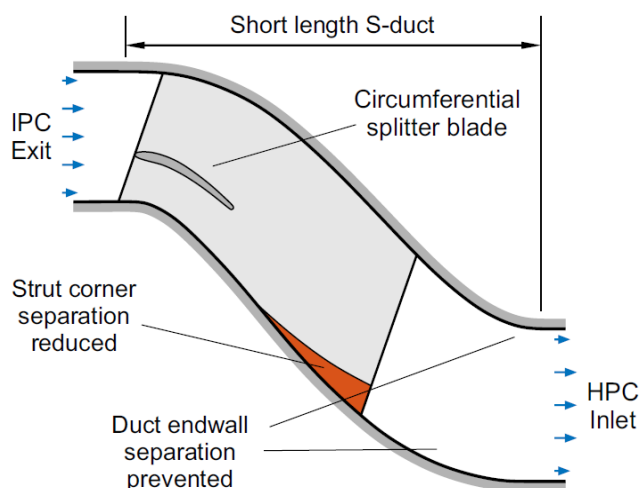


Figure 2.22 Duct with splitter blade [29].

### 2.5.3 Flow Controlling Devices

The flow separation, which is likely to occur within the duct, near its walls, affects negatively on its performance. Hence, it is of great significance to control the evolution of such effects in order to design more aggressive intermediate compressor ducts with larger radial offset. Therefore, many researchers have focused on the development of flow control devices. With respect to the technique used the devices are classified as active or passive. The most common passive devices are using vanes or plates, for example submerged vortex generators (VGs) and span-wise cylinders. Active methods usually involve synthetic jet actuators, with the most well-known being vortex generators jet (VGJs) and the injection of higher energy fluid to reenergize the boundary layer.

Passive vortex generators have already been used to control the separation of the boundary layer and improve the total pressure recovery, as mentioned in [32]. However, active methods present many advantages, explained in [19]. Their actuation is simple, and they can respond quickly to prevent the appearance of separation. Another important benefit of such control devices is that their drag penalty is almost negligible.

In addition to the use of specialized devices, the possibility of designing a bleed system to re-energize the boundary layer has been investigated by Walker et al. in [11]. The idea was inspired by a similar system developed by the authors for combustor pre-diffusers. The function of the system is based on two mechanisms. Firstly, the bleed flow is accelerated through the bleed duct, and it is gaining streamwise momentum. This momentum is transported through the turbulent shear layer to the mainstream flow re-energizing it and assisting it to remain attached to the hub wall. The second mechanism is based on the radial pressure gradient created by the entrance of the bleed flow to the duct flow, which enhances the transfer of higher momentum to it. Although the determination of the location and the mass flow of the system required preliminary predictions the results were promising. The best location was at 35-40% of duct length with a bleed flow rate of 5%. A length reduction of 30-40% was possible with the flow within the S-duct remaining fully attached.

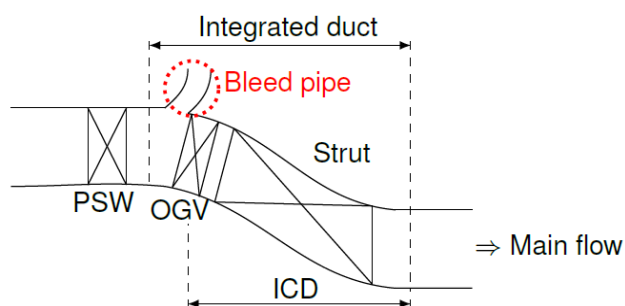


Figure 2.23 Schematic for the location of bleed pipe [33].

Siggeirsson et al. in [33] compared the impact of different bleed fraction rates to the performance of the intermediate duct. The bleed pipe was placed upstream of the duct and

the OGVs as seen in Figure 2.23. It was observed that for the lower bleed fraction, 10%, the flow was more prone to separation as stronger adverse pressure gradients were developed. On the contrary for a bleed rate of 30% due to the extraction of larger amount of mass flow the velocity in the bleed pipe was decreased and the pressure gradient was reduced. Finally, the authors suggested that the CFD prediction for the flow developed near the inner wall was less accurate for the higher bleed rate and the simulation more unstable.

## Chapter 3 Analysis and Parametrization Process of Existing Turbofan Engines

In this Chapter the results of the analysis of existing turbofan engines are discussed. Based on the observations made for the intermediate compressor ducts of the different engines a parametrization process is proposed. The aim of this is to specify the parameters required by the user to estimate, as accurately as possible, the pressure losses associated with the duct design.

### 3.1 Digitization of Turbofan Engines

To analyze the geometry of the intermediate compressor ducts the digitization of already existing turbofan engines was required. The configuration coordinates of seventeen turbofan engines were obtained, from their section images, using Plot Digitizer. In Table 3.1, some of the main specifications and dimensions available for the engines examined are presented. The aim was to focus on engines with higher bypass ratios since, as it is explained in Section 2.2, in these cases more aggressive ducts are used, leading to higher losses.

<i>Engine</i>	<i>Stages</i>		<i>Rotor Speed (RPM)</i>		<i>Dimensions (m)</i>		<i>Performance</i>	
	<i>LPC/IPC</i>	<i>HPC</i>	<i>LPC/IPC</i>	<i>HPC</i>	<i>Fan Diameter</i>	<i>Overall Length</i>	<i>BPR</i>	<i>OPR</i>
<i>PW1000G</i>	3	8	10500	18000-20000	2.05	3.401	12.5	-
<i>PW1000G (Early Version)</i>	3	5	-	-	2.1	3.184	-	-
<i>PW8000</i>	3	5	-	-	1.93	3.15	10	
<i>GE90</i>	3	10	2261.5	9332	3.12	7.29	8.4-9	40
<i>TRENT900</i>	8-Jan	6	2900/8300	12200	2.95	5.478	8.5-8.7	37-39
<i>GP7275</i>	4	9	-	-	2.95	4.5466	8	46
<i>GP7176</i>	2	10	-	-	2.794	4.2926	7.8	-
<i>CFM56-5C</i>	4	9	4784	14460	1.84	2.622	6.4-6.5	37.4-38.3
<i>PW4084</i>	6	11	-	-	2.84	4.84	5.8-6.4	34.2-42.8
<i>CF34-10</i>	3	9	6325	18018	1.3462	2.3	5.4	29

V2500-A1	3	10	-	-	1.587	3.201	5.4	29.8
JT9D-7	3	11	3650	8000	2.34	3.934	4.9	21.1
PW4000	5	11	-	-	2.54	4.25	4.9	32.0-34.1
V2500-A5	4	10	-	-	1.613	3.201	4.5-4.9	26.9-33.4
BR715	2	10	6096	16661	1.47	3.738	4.55-4.68	29-32
TFE731-2	4	1	20688-21000	29692-30540	1	1.521	2.8	13-15
TFE731-5	4	1	20688-21001	29692-30541	1.029	1.666	2.8	13-15

Table 3.1 Characteristics of examined turbofan engines.

Plot Digitizer is a Java program, generally used to digitize scanned plots of functional data. For the digitization of the images the calibration of X and Y axis based on the known dimensions of each engine was necessary. The dimensions used were the fan tip diameter and the length of each engine. The data points digitized in every case were representing the input or output of a compressor or turbine stage as well as some intermediate points. The configuration points corresponding to the intermediate compressor duct for each case were extracted and further analyzed. For example, the points chosen for the core path of GE90 are clearly shown in Figure 3.1. The rest of the engines' images used for this process are presented in Appendix A.

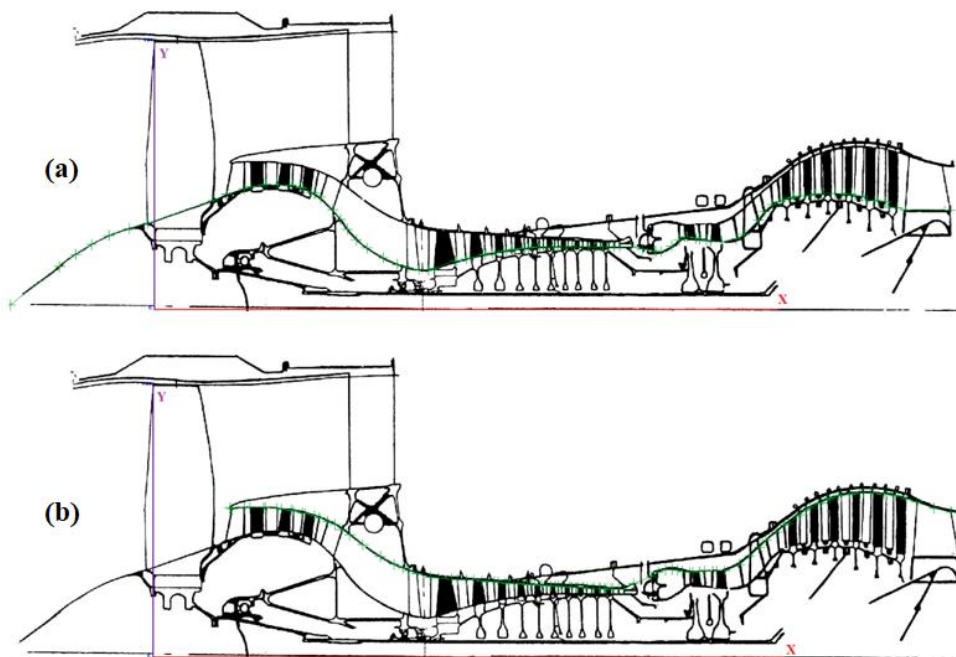


Figure 3.1 Digitized Points along the (a) Hub and (b) Shroud of GE90.



As it can be observed in Figure 3.2, the points acquired by the digitization can describe accurately the geometry of both the shroud and the hub. As a result, it is possible to plot the intermediate compressor duct along with its mean radius line, calculated by equation (3.1), as in Figure 3.3.

$$R_m = \frac{R_{shroud} + R_{hub}}{2} \quad (3.1)$$

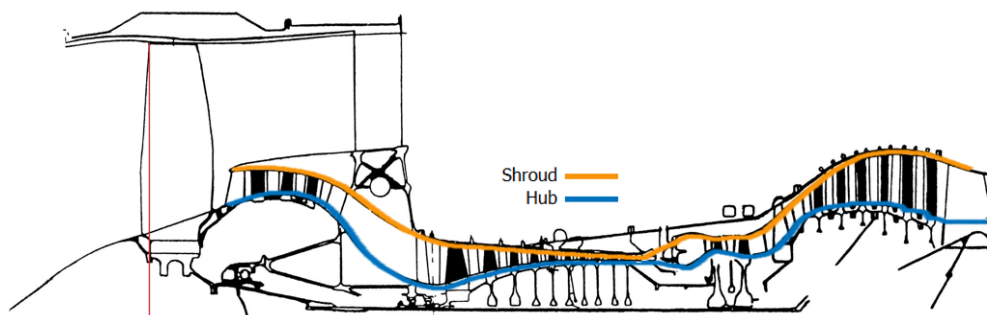


Figure 3.2 Comparison of digitized and real duct's geometry for GE90.

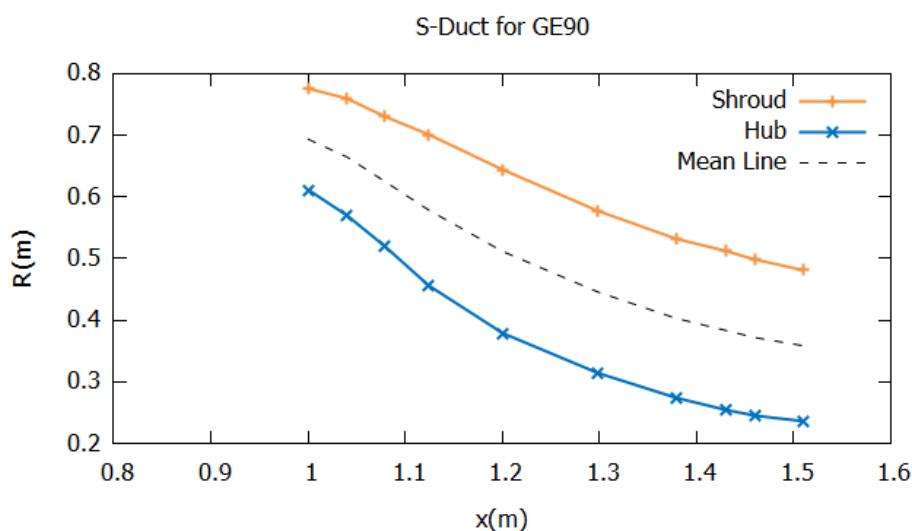


Figure 3.3 S-Duct geometry acquired by digitization for GE90.

## 3.2 Analysis of Digitized Data

### 3.2.1 Calculation of Main Geometric Parameters

For each engine's S-duct the basic geometric parameters, as presented in Section 2.4.1, should be calculated. The hub and tip radii as well as the duct's length are known, from the digitization process, so it is possible to calculate the area and the mean radii along the duct, the inlet height and its radial offset. Another parameter especially used as a design parameter for the upstream and downstream compressor is the ratio of hub to tip radius

in the inlet and the outlet of the S-duct, corresponding to the outlet of the LPC and the inlet of HPC, respectively. All the above-mentioned parameters are included in Table 3.2.

Engine	L (m)	$\left(\frac{R_{hub}}{R_{shroud}}\right)_{in}$	$\left(\frac{R_{hub}}{R_{shroud}}\right)_{out}$	$\frac{A_{out}}{A_{in}}$	$\frac{\Delta R}{L}$	$\frac{h_{in}}{L}$	$\frac{R_{min}}{L}$
<i>PW1000G</i>	0.5688	0.8049	0.7617	0.6039	0.1995	0.1413	0.6535
<i>PW1000G (Early Version)</i>	0.2564	0.8510	0.7037	0.9387	0.4535	0.2141	1.3301
<i>PW8000</i>	0.2935	0.8199	0.6215	1.1348	0.3127	0.2019	1.0203
<i>GE90</i>	0.5088	0.7880	0.4906	0.7707	0.6581	0.3232	1.3629
<i>TRENT900</i>	0.2338	0.8344	0.8290	0.6678	0.3184	0.2921	1.6174
<i>GP7275</i>	0.3477	0.8085	0.4818	0.8542	0.9060	0.3903	1.8432
<i>GP7176</i>	0.3595	0.7486	0.4822	0.8444	0.6417	0.4475	1.5564
<i>CFM56-5C</i>	0.3578	0.8189	0.7095	0.8155	0.3366	0.2170	1.0898
<i>PW4084</i>	0.4568	0.8046	0.6650	0.8143	0.3994	0.2558	1.1814
<i>CF34-10</i>	0.2099	0.8223	0.6904	0.8669	0.5234	0.3183	1.6321
<i>V2500-A1</i>	0.3956	0.7774	0.5607	0.8184	0.3912	0.2470	0.9865
<i>JT9D-7</i>	0.2740	0.7689	0.7427	0.8532	0.2274	0.4536	1.7359
<i>PW4000</i>	0.2396	0.7377	0.6689	0.7721	0.4271	0.5887	1.9504
<i>V2500-A5</i>	0.3948	0.7827	0.5539	0.8595	0.3996	0.2460	1.0092
<i>BR715</i>	0.2762	0.7885	0.5582	0.8088	0.5689	0.3209	1.3570
<i>TFE731-2</i>	0.1049	0.8164	0.6698	0.8447	0.4892	0.2889	1.4291
<i>TFE731-5</i>	0.1065	0.8229	0.6735	0.8587	0.4806	0.2698	1.3886
<b>Average</b>	-	0.7998	0.6390	0.8310	0.4549	0.3068	1.3614
<b>Min. Value</b>	-	0.7377	0.4818	0.6039	0.1995	0.1413	0.6535
<b>Max. Value</b>	-	0.8510	0.8290	1.1348	0.9060	0.5887	1.9504

Table 3.2 Main geometric parameters of the analyzed engines.

The average value for each of the examined parameters can be compared to the corresponding typical one, as given in Table 2.1. As it can be observed, most of them are close to the standard range, however there are some differentiations which can be justified since the typical values correspond to conservative duct designs. The minimum and maximum values define the range within which the user can select the value for each geometric parameter. It should be noted that even though the data acquired by the digitization can be used for the description of the S-duct's geometry there is an amount of uncertainty introduced by the way the points on the plot were chosen, thus deviations between the real or typical and the calculated values are expected.

### 3.2.2 Radius Distribution

In bibliography, various ways are proposed for the parametrization of the S-duct, including the use of B-splines or Bezier curves or even the use of sinusoidal curves. For the purpose of this work, a simplest parametrization process was desired, since the user should be able to determine the duct's geometry with as few parameters as possible.

From the digitized data, it was observed that a quadratic polynomial function could describe the distribution of the hub and tip radii accurately. More specifically, for the parametrization of the radii distribution the non-dimensional distance is used, as it is defined in equation (3.2).  $x_{real}$  is the dimensional distance from the axis origin, shown in Figure 3.1, while  $x_{in}$  and  $x_{out}$  stand for the distance of the inlet and the outlet of the intercompressor duct, respectively.

$$x = \frac{x_{real} - x_{in}}{x_{out} - x_{in}}, \quad x \in [0,1] \quad (3.2)$$

The function used to connect the non-dimensional distance to the radius is given by equation (3.3).

$$r = \frac{R - R_{in}}{R_{out} - R_{in}} = a_2 x^2 + a_1 x, \quad r \in [0,1] \quad (3.3)$$

$$a_2 + a_1 = 1 \quad (3.4)$$

Where  $R$  is the hub or shroud radius,  $r$  is the non-dimensional radius,  $R_{in}$  and  $R_{out}$  are the hub and tip radius at the inlet and the outlet of the duct and  $a_2, a_1$  are the function's coefficients. The coefficients can determine the curvature of the duct's walls. Their sum equals to unity to assure that  $r \in [0,1]$  and their values differ for each engine, as presented in Table 3.3. The plots of the different ducts suggest that the curvature is increased as  $a_2$  is decreased. For high positive values of  $a_2$  in the shroud walls the curvature can be even reversed.

Engine	$a_{2_{shroud}}$	$a_{1_{shroud}}$	$a_{2_{hub}}$	$a_{1_{hub}}$
<i>PW1000G</i> ( <i>Early Version</i> )	-0.630	1.630	-0.470	1.470
<i>PW1000G</i>	-0.600	1.600	-1.088	2.088
<i>PW4084</i>	-0.586	1.586	-0.670	1.670
<i>PW8000</i>	-0.530	1.530	-0.935	1.935
<i>GP7275</i>	-0.530	1.530	-0.678	1.678
<i>TFE731-2</i>	-0.400	1.400	-0.790	1.790
<i>GP7176</i>	-0.400	1.400	-0.780	1.780
<i>PW4000</i>	-0.377	1.377	-0.890	1.890
<i>CF34-10</i>	-0.370	1.370	-0.720	1.720
<i>GE90</i>	-0.200	1.200	-0.860	1.860
<i>CFM56-5C</i>	-0.100	1.100	-0.630	1.630
<i>JT9D-7</i>	0.090	0.910	-1.050	2.050
<i>V2500-A1</i>	0.230	0.770	-0.510	1.510
<i>V2500-A5</i>	0.250	0.750	-0.600	1.600
<i>TRENT900</i>	0.250	0.750	-0.040	1.040
<i>BR715</i>	0.500	0.500	-0.590	1.590
<i>TFE731-5</i>	0.670	0.330	-0.510	1.510

Table 3.3 Coefficients of the radius distribution.

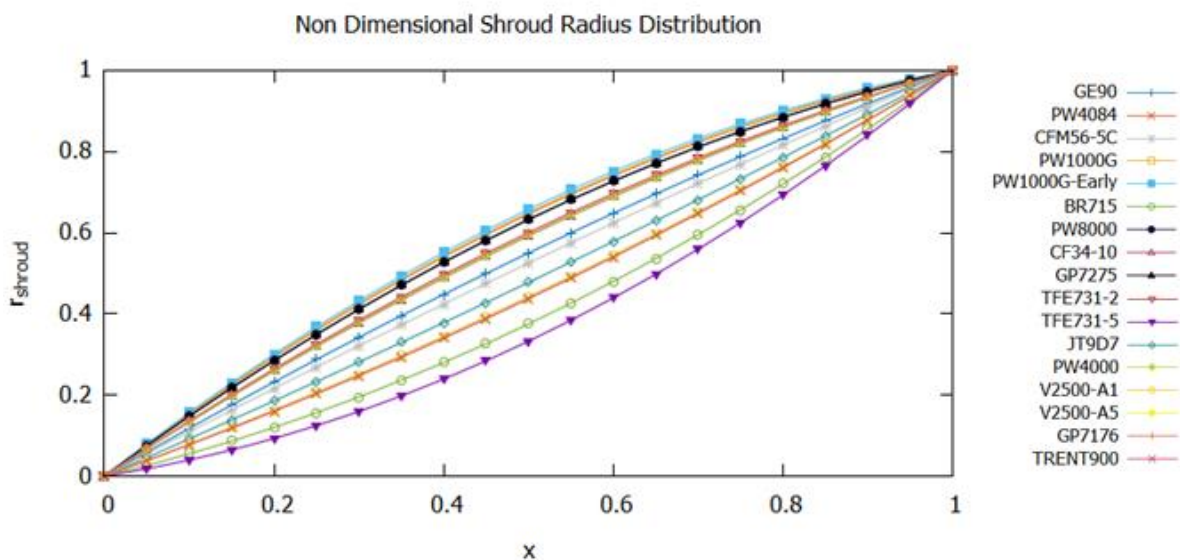


Figure 3.4 Non dimensional shroud radius distribution.

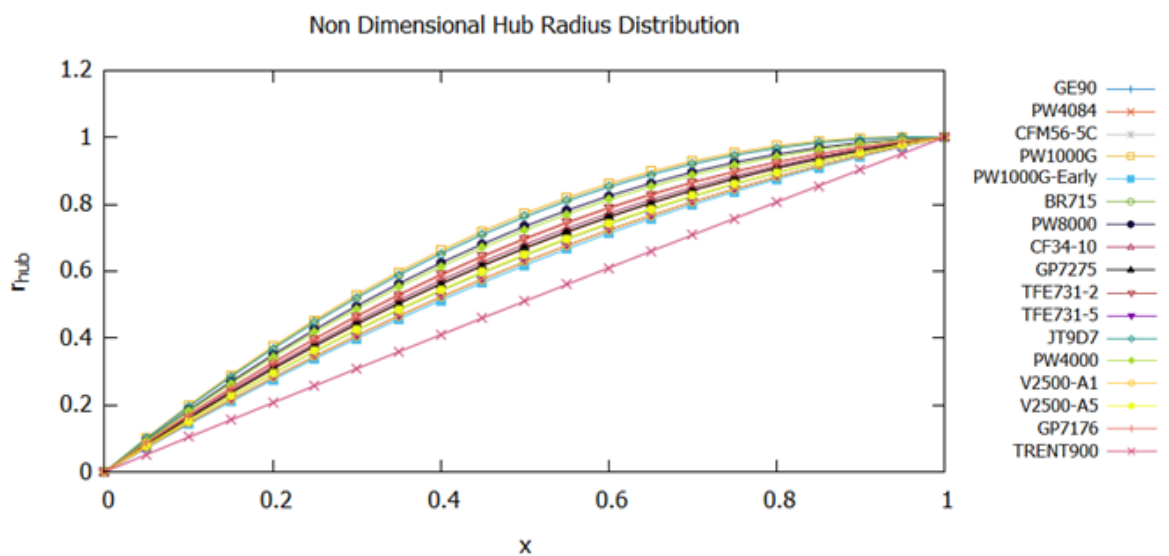


Figure 3.5 Non dimensional hub radius distribution.

In order to reduce the parameters needed to describe the geometry of the duct's walls the existence of a correlation between the shroud and hub coefficients was examined. After excluding the outliers, a linear correlation could be found between the coefficients  $a_2$  of the quadratic terms, shown in Figure 3.6 and described by equation (3.5). As a result, only  $a_{2shroud}$  is required to determine the curvature of the intermediate compressor duct for each engine.

$$a_{2hub} = 0.2417a_{2shroud} - 0.6706 \quad (3.5)$$

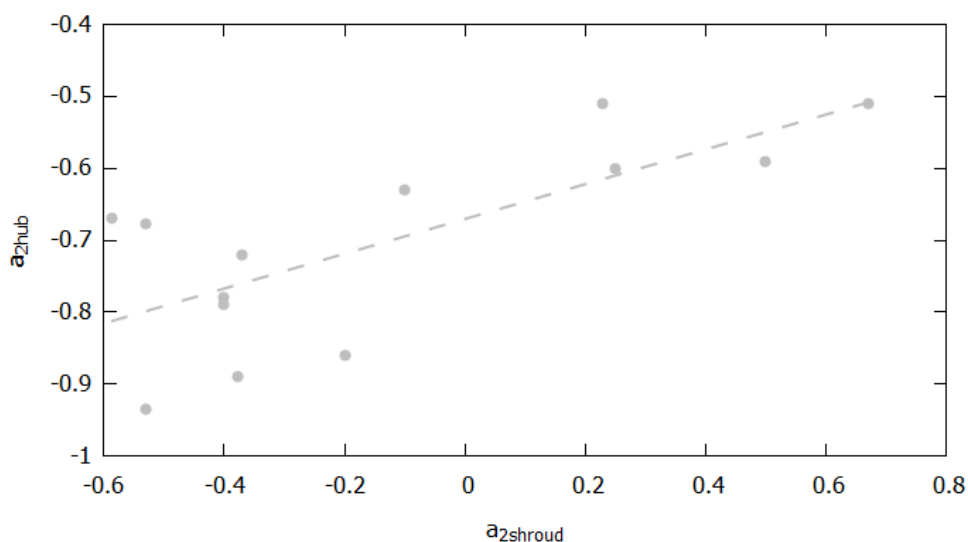


Figure 3.6 Linear correlation between shroud and hub's coefficients.

The estimated duct geometry obtained by the proposed process does not differentiate significantly from the geometry acquired by digitization, as shown for GE90 in Figure 3.7.

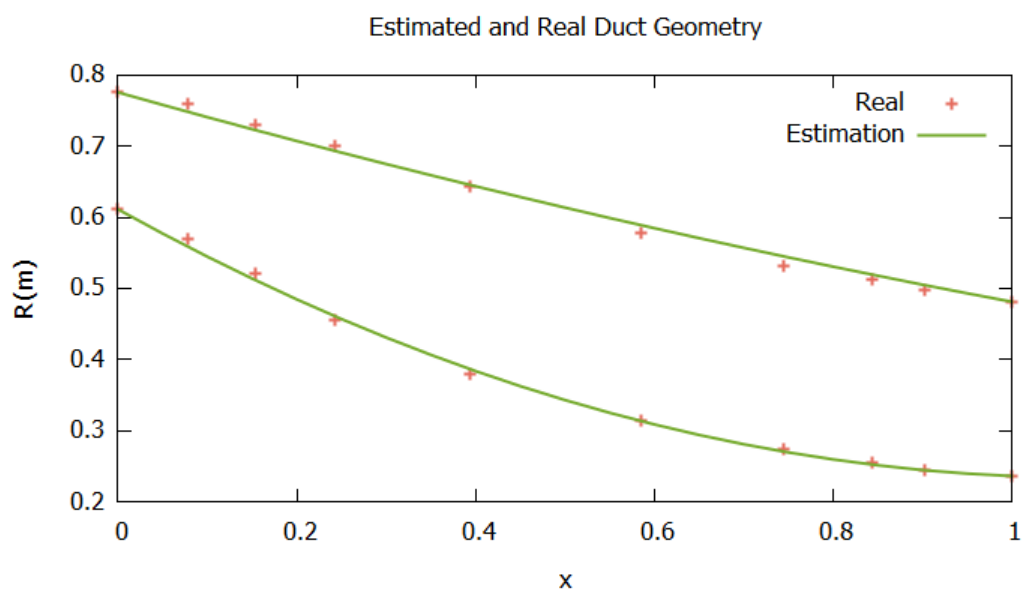


Figure 3.7 Comparison of Estimated and real duct's geometry.

Although, through the observations made this mathematical correlation is valid, in bibliography a similar connection between the geometry of the hub and shroud walls is not mentioned. For this work the use of the equation (3.5) is justifiable since constraints considered by the designers, such as the presence of struts and instrumentations, are not taken into account.

### 3.2.3 Area Distribution

A similar process was followed for the parametrization of the area distribution along the S-duct. In this case, the digitized data suggested that a cubic function could be employed for the connection of the non-dimensional area along the duct with the non-dimensional distance, given by equation (3.2)(3.6).

$$\alpha = \frac{A - A_{in}}{A_{out} - A_{in}} = b_3x^3 + b_2x^2 + b_1x, \quad \alpha \in [0,1] \quad (3.6)$$

$$b_3 + b_2 + b_1 = 1 \quad (3.7)$$

In equation (3.6),  $A, A_{in}, A_{out}$  stand for the area corresponding to the position  $x$ , the inlet and the outlet of the duct, respectively. The coefficients of the function  $b_3, b_2, b_1$  are real numbers, whose sum equals unity, and they vary, as can be observed in Table 3.4.

<b>Engine</b>	<b><math>b_3</math></b>	<b><math>b_2</math></b>	<b><math>b_1</math></b>
<i>TFE731-5</i>	-22.4190	49.8880	-26.4690
<i>TFE731-2</i>	-16.6910	27.0600	-9.3690
<i>PW1000G (Early Version)</i>	-11.9730	23.2680	-10.2950
<i>CF34-10</i>	-9.4490	16.9890	-6.5400
<i>GE90</i>	-8.7993	17.1760	-7.3767
<i>V2500-A5</i>	-5.2431	16.1350	-9.8919
<i>PW8000</i>	-4.1313	0.0410	5.0903
<i>JT9D-7</i>	-2.9586	7.2873	-3.3287
<i>V2500-A1</i>	-2.4458	9.1929	-5.7471
<i>GP7275</i>	-1.4038	5.1416	-2.7378
<i>GP7176</i>	-0.9470	4.3926	-2.4456
<i>PW1000G</i>	0.0409	0.4490	0.5123
<i>PW4084</i>	0.3758	-0.2373	0.8615
<i>CFM56-5C</i>	2.1672	1.4223	-2.5895
<i>PW4000</i>	3.1628	-3.6261	1.4633
<i>BR715</i>	4.7877	1.4524	-5.2401
<b>Average</b>	-4.6544	10.6798	-5.0254

Table 3.4 Coefficients of the area distribution.

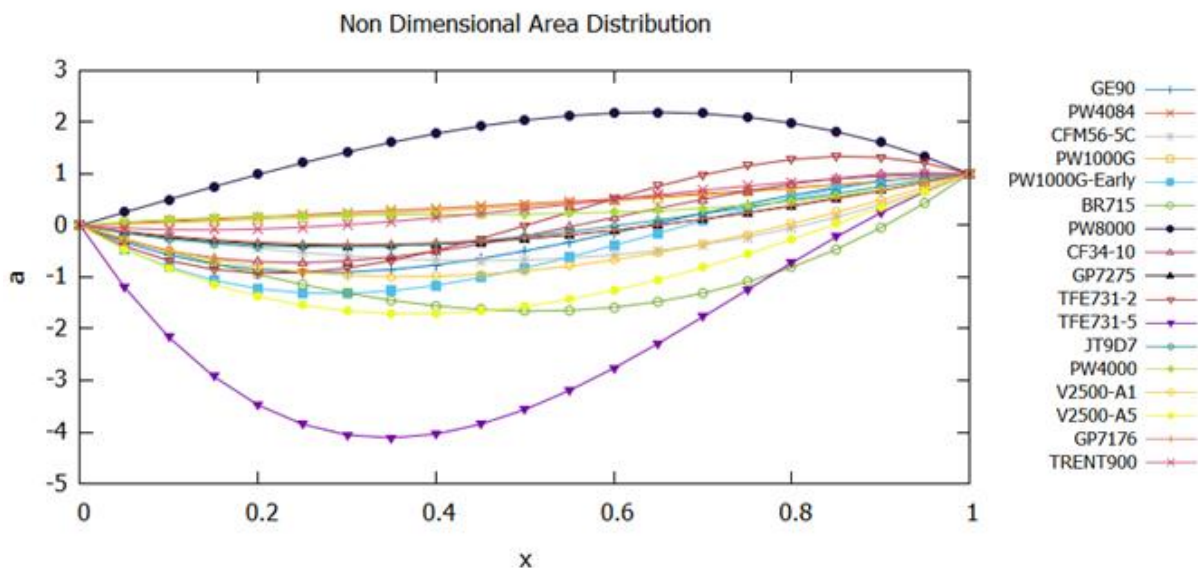


Figure 3.8 Non dimensional area distribution along the duct.

However, for the area distribution the search of a correlation between its coefficients and the coefficients related to the radii distributions was not necessary since the area at each position can be directly computed knowing the hub and tip radii from equation (3.8).

$$A = \pi(R_{shroud}^2 - R_{hub}^2) \tag{3.8}$$

As it is shown in Figure 3.9, the predicted area distribution along the S-duct is describing almost accurately the one derived from the digitization process.

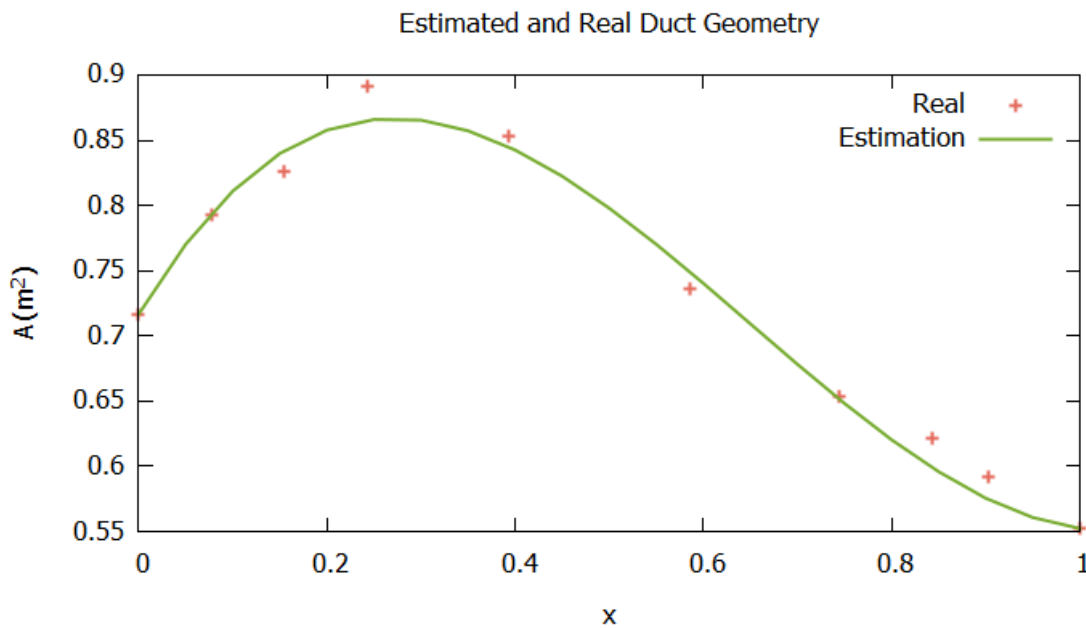


Figure 3.9 Comparison of estimated and real duct's area distribution.

### 3.3 Parameterization Process

The parameterization of the geometry is critical to choose the minimum number of variables which should be given by the user for the estimation of the duct's losses. Based on the observations, the analysis and the correlations found in the previous paragraphs two different "design" processes can be proposed. In both the processes the flow conditions in the inlet of the duct, meaning the total pressure  $P_t$ , the total temperature  $T_t$ , the mass flow  $\dot{m}$  and the properties of the fluid  $\gamma, C_p, R$ , are considered known. Their main difference is that in the first one the inputs required are only geometrical parameters, whereas in the second one the Mach number, in both the inlet and the outlet of the duct, should be specified by the user.

In the first case, referred to as *Parameterization Process I*, the user should define all the non-dimensional geometric parameters discussed in Section 3.2.1, as well as the overall length of the S-duct and the  $a_{2shroud}$  coefficient. More specifically, all the main geometric parameters of the duct, at its inlet and outlet, can be calculated knowing  $\frac{\Delta R}{L}, \frac{h_{in}}{L}, \frac{R_{min}}{L}, \frac{A_{out}}{A_{in}}, L$  by equations (3.9)-(3.14).

$$R_{hub_{in}} = R_{m_{in}} - \frac{h_{in}}{2} \quad (3.9)$$

$$R_{shroud_{in}} = R_{hub_{in}} + h_{in} \quad (3.10)$$

$$A_{in} = \pi(R_{shroud_{in}}^2 - R_{hub_{in}}^2) \quad (3.11)$$

$$R_{m_{out}} = R_{m_{in}} - \Delta R \quad (3.12)$$

$$R_{shroud_{out}} = R_{m_{out}} + \frac{A_{out}}{4\pi R_{m_{out}}} \quad (3.13)$$

$$R_{hub_{out}} = 2R_{m_{out}} - R_{shroud_{out}} \quad (3.14)$$

For the distributions of hub and shroud radii along the duct the correlation between the coefficients of the quadratic functions, given by equation (3.5), can be used.

$$R_{shroud_x} = R_{shroud_{in}} + (R_{shroud_{out}} - R_{shroud_{in}})(a_{2shroud}x^2 + a_{1shroud}x) \quad (3.15)$$

$$R_{hub_x} = R_{hub_{in}} + (R_{hub_{out}} - R_{hub_{in}})(a_{2hub}x^2 + a_{1hub}x) \quad (3.16)$$

Finally, the acquired radii distributions are used for the calculation of the dimensionless area distribution, by equations (3.6),(3.8), and the graphical acquisition of the coefficients of the cubic function. Through this process it is possible to obtain the full geometry of the S-Duct which can be directly used for the detailed calculation of pressure losses in ANSYS CFX, as it is explained in detail in Chapter 4.

For the *Parameterization Process II* the main non dimensional geometric parameters mentioned above are not given by the user, but they are derived. The inputs required for



the calculations are the main parameters usually available to designers: the ratio of hub to tip radius, both at the inlet and the outlet of the duct,  $\left(\frac{R_{hub}}{R_{shroud}}\right)_{in}$ ,  $\left(\frac{R_{hub}}{R_{shroud}}\right)_{out}$ , the Mach numbers at these positions  $M_{in}$ ,  $M_{out}$ , as well as the length of the duct  $L$ . The relation (3.17) is used for the calculation of the inlet and outlet duct area based on the corresponding flow properties.

$$A = \frac{\dot{m}}{\frac{P_t}{\sqrt{T_t}} \sqrt{\frac{\gamma}{R}} M \left(1 + \frac{\gamma-1}{2} M^2\right)^{-\frac{\gamma+1}{2(\gamma-1)}}} \quad (3.17)$$

To estimate the outlet area, knowing that the total temperature is constant along the duct, it is assumed that total pressure remains unchanged. This hypothesis is justifiable since the pressure loss is not expected to be significant. The shroud radius, at both the inlet and outlet, and consequently the hub radius, can be calculated by (3.18).

$$R_{shroud} = \sqrt{\frac{A}{\pi \left(1 - \left(\frac{R_{hub}}{R_{shroud}}\right)^2\right)}} \quad (3.18)$$

Like in *Parameterization Process I*, the user should again define the coefficient  $a_{2shroud}$  in order to be provided with the geometry of the S-Duct. This method is applied to validate the model for different design mass flows, as it is demonstrated in Section 5.3.

## Chapter 4 Flow Simulation in CFX

In this Chapter the solving process and the settings used for the flow simulation in ANSYS CFX are explained. In addition, the boundary conditions applied at the inlet and outlet of the intercompressor duct are presented. Finally, the simulation's results for the base case S-Duct are discussed.

It is worth mentioning that, since the flow inside the S-duct is characterized by circumferential periodicity, only a  $10^\circ$  sector is necessary to be solved. This approach reduces the computational cost of the simulation and allows the generation of finer meshes leading to higher accuracy. Another useful observation related to the geometry of the S-duct analyzed is that two straight parts have been added to the inlet and the outlet of the duct to assure that the flow is fully developed, as it is commonly done in the bibliography.

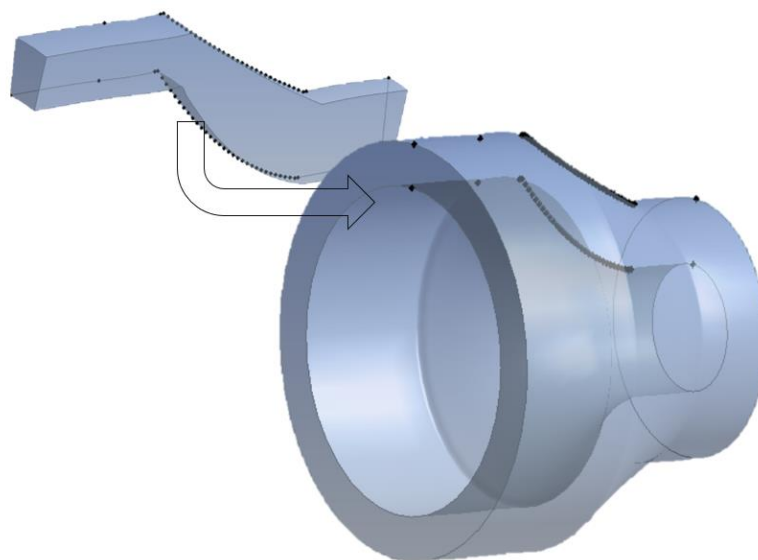


Figure 4.1 3D model of the duct's  $10^\circ$  sector.

### 4.1 Mesh Generation

The meshing process is essential for the discretization of the governing equations. More specifically, obtaining an analytical solution for the Navier-Stokes equations is possible only for simple flows and ideal conditions. For real flows, a numerical solution can be found by

replacing the equations with algebraic approximations. ANSYS, which is the program used for the CFD simulation, adopts an element-based finite volume method which involves the discretization of the flow domain using a three-dimensional mesh. Within these volumes, flow quantities, such as mass, momentum and energy, are preserved. All solution variables and fluid properties are stored at the mesh nodes, or mesh vertices, with a control volume constructed around them. To obtain the numerical solution, the Navier-Stokes differential equations are integrated over each control volume and the produced integrals are discretized within each element. The solution field and its gradients can be approximated between the mesh nodes, at integration points, using finite-element shape functions. These functions depend on the element type chosen for the mesh generation. [44]

### 4.1.1 Mesh Method

A hexahedral mesh was chosen for the section of the S-Duct, which is considered to provide speed and accuracy in cases like the one examined. Since there is only one body to be meshed, there is the possibility to control the mesh method applied for the successful generation of the mesh. For the needs of this simulation the MultiZone method is used. This meshing technique provides automatic decomposition of the body geometry into mapped and free regions. In the first ones, a hexahedral mesh is used, while in the latter, unstructured regions, where the creation of hexahedral elements is not possible, a free mesh is generated. As it is shown in Figure 4.3, for the free mesh type is not allowed, forcing the program to create a pure hexahedral mesh. [45]

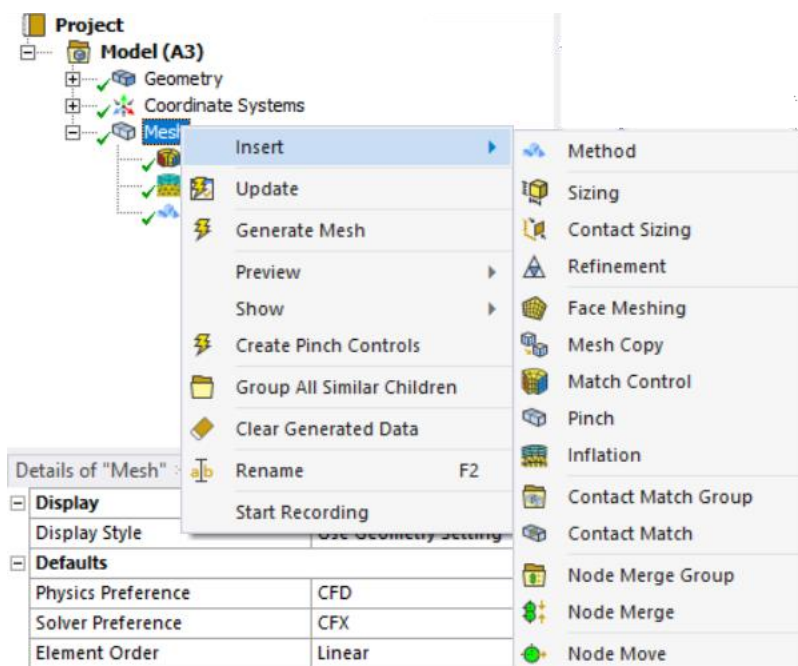


Figure 4.2 Menu of mesh controls.

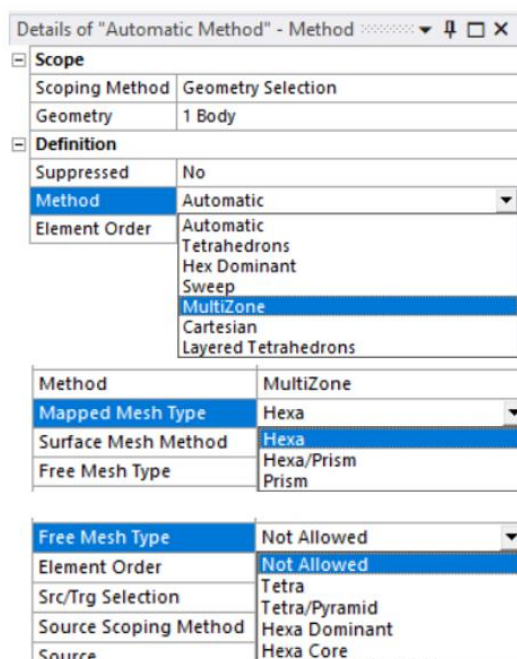


Figure 4.3 Selection of Mesh method.

### 4.1.2 Inflation

The mesh generation is followed by its refinement in certain areas. The mesh adaption locations are where the solution variables are expected to change rapidly. The refinement of mesh is of great importance for the boundary layer resolution. The specifics of the mesh in the area near the duct walls can be defined in the Inflation Tab. Firstly, the faces near which the inflation should be applied are selected. For the S-duct case these are the shroud and the hub walls, as seen in Figure 4.4.

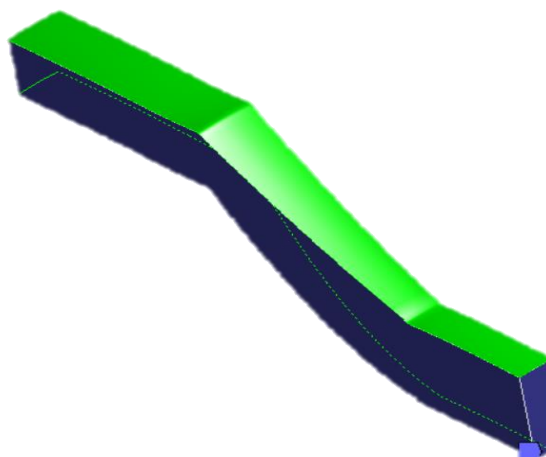


Figure 4.4 Selection of boundary surfaces.

The next step is to determine the Inflation Option suitable for each case. The available options are: *Smooth Transition*, which is the default choice and assures a smooth rate of

volume change across the boundary layer height, *Total Thickness*, for which the total thickness of the inflation layers should be selected and *First Layer Thickness*, in which the first element height should be given as an input. In order to confirm that the non-dimensional distance  $y^+$  is maintained within the desired limits the First Layer Thickness inflation method is preferred, with the correct adjustment of the First Layer Height.

A value of  $y^+ \approx 1$  is required in most of the cases to resolve accurately the viscous sublayer. In this case, the Low-Reynolds Number Method is implemented by CFX in the region with the finer mesh. The adjustment of  $y^+$  is achieved by the selection of the First Layer Height, calculated by the following equations.

$$y^+ = \frac{\rho \Delta y u_\tau}{\mu} \quad (4.1)$$

$$u_\tau = \left( \frac{\tau_w}{\rho} \right)^{\frac{1}{2}} \quad (4.2)$$

$$\tau_w = \frac{1}{2} C_f \rho U_0^2 \quad (4.3)$$

$$C_f = 0.079 Re^{-0.25} \quad (4.4)$$

$\Delta y$  is the distance of the first element from the wall,  $u_\tau$  is the friction velocity,  $\tau_w$  is the wall shear stress and  $C_f$  is the skin friction coefficient, which is determined, for internal flows by (4.4).

The Maximum Layers value controls the number of inflation layers generated, while the Growth Rate determines their relative thickness. These values should be chosen carefully for CFX to resolve the boundary layer as accurately as possible. In Figure 4.5 the settings applied at the Inflation Tab are shown.

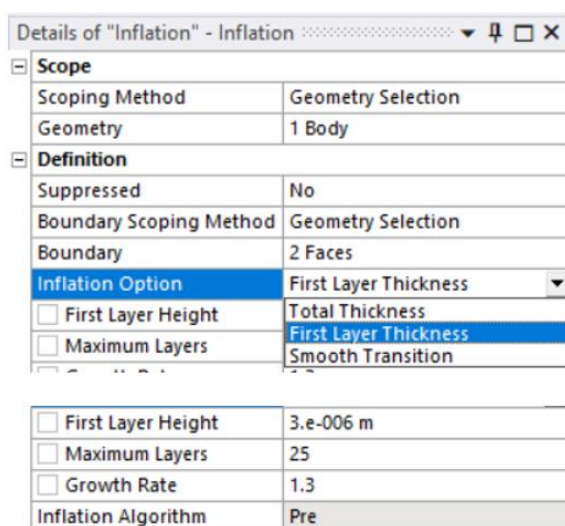
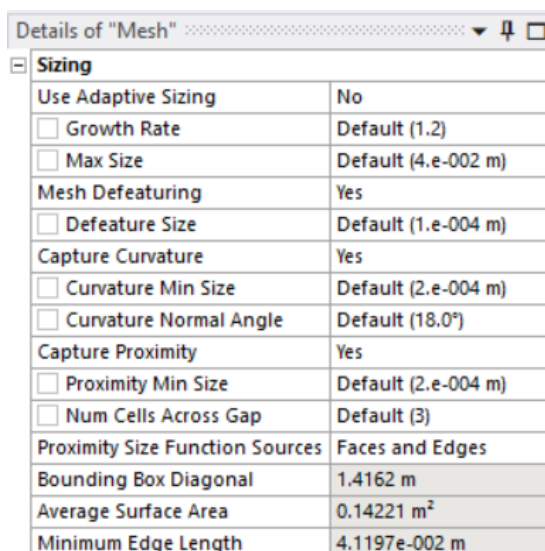


Figure 4.5 Defining the inflation options.

### 4.1.3 Sizing

As it is suggested by its name, the examined duct is S-shaped and thus the mesh should be correctly adapted to the wall curvature. ANSYS meshing offers this possibility by activating the Capture Curvature and Proximity options. The curvature size function used by the program examines the curved edges and faces and computes the element size required locally such that the maximum size or the curvature angle, automatically computed, are not violated. The proximity function is employed to compute the element layers created in “gaps” of the model, which can be either internal volumetric regions between two faces or areas between two opposing boundary edges of a face, as mentioned in [45].



Details of "Mesh"	
<b>Sizing</b>	
Use Adaptive Sizing	No
<input type="checkbox"/> Growth Rate	Default (1.2)
<input type="checkbox"/> Max Size	Default (4.e-002 m)
Mesh Defeaturing	Yes
<input type="checkbox"/> Defeature Size	Default (1.e-004 m)
Capture Curvature	Yes
<input type="checkbox"/> Curvature Min Size	Default (2.e-004 m)
<input type="checkbox"/> Curvature Normal Angle	Default (18.0°)
Capture Proximity	Yes
<input type="checkbox"/> Proximity Min Size	Default (2.e-004 m)
<input type="checkbox"/> Num Cells Across Gap	Default (3)
Proximity Size Function Sources	Faces and Edges
Bounding Box Diagonal	1.4162 m
Average Surface Area	0.14221 m <sup>2</sup>
Minimum Edge Length	4.1197e-002 m

Figure 4.6 Mesh sizing options.

Another significant parameter determined is the Element Size, which is the size used for all the edge, face and body meshing. This variable directly affects the accuracy of the simulation, and as it is shown in Section 4.4.1, is determined by conducting a grid independence study.

### 4.1.4 Match Control

As it is elucidated above, the flow in only a sector of the annular duct needs to be simulated. However, it is significant to ensure that the grid generated at the sides of the periodic domain is identical. For this purpose, Cyclic Match Control is used, which involves the copying of the first selected face mesh to the second one. To apply this control, it is necessary to define a new cylindrical coordinate system to which the axis of rotation belongs.

Details of "Match Control" - Match Control	
<b>Scope</b>	
Scoping Method	Geometry Selection
High Geometry Selection	1 Face
Low Geometry Selection	1 Face
<b>Definition</b>	
Suppressed	No
Transformation	Cyclic
Axis of Rotation	Coordinate System
Control Messages	No

Figure 4.7 Match control options.

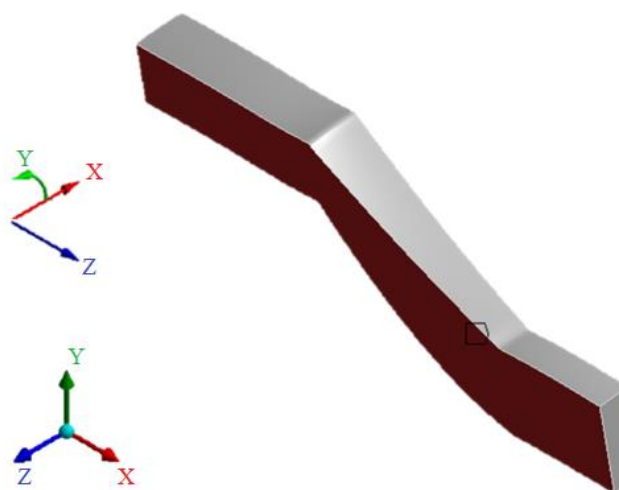


Figure 4.8 Definition of cylindrical coordinate system.

## 4.2 Simulation Setup at CFX-Pre

### 4.2.1 Physical Models

The simulations conducted for the purpose of this work are steady. This means that the flow characteristics are not expected to change with time since steady flow conditions have been reached after a relatively long-time interval. An example of a steady-state flow is after the startup of a rotating machine, which is like the case examined here. The fluid is considered to be continuous, air ideal gas, as shown in Figure 4.9, and the reference pressure is set to  $0 \text{ atm}$ , to make easier the understanding of the results. The set of governing equations solved by ANSYS CFX, are the Navier-Stokes equations which consist of the continuity, momentum and energy equations.

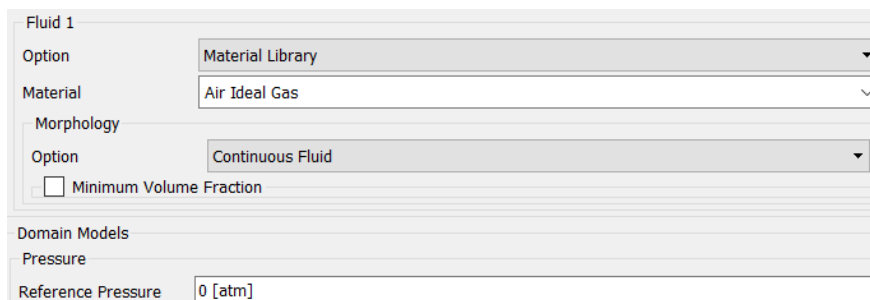


Figure 4.9 Definition of fluid properties.

A heat transfer model is used to predict the flow temperature along the duct. All possible types of heat transfer, like conduction, convection turbulent mixing and viscous work, can be modelled. The options available in CFX cover various models, however, the most suitable for the case analyzed is the Total Energy model. This model is used to consider the transport of enthalpy while taking into account the kinetic energy effects. As it is underlined in [44], it is commonly used for gas flows where the Mach number is larger than 0.3. The equation describing the mathematical model used is (4.5).

$$\frac{\partial(\rho h_{tot})}{\partial t} - \frac{\partial p}{\partial t} + \nabla \cdot (\rho \mathbf{U} h_{tot}) = \nabla \cdot (\lambda \nabla T) + \nabla \cdot (\mathbf{U} \cdot \boldsymbol{\tau}) + \mathbf{U} \cdot \mathbf{S}_M + \mathbf{S}_E \quad (4.5)$$

$$h_{tot} = h + \frac{1}{2} \mathbf{U}^2 \quad (4.6)$$

Where  $h_{tot}$  is the total enthalpy,  $\mathbf{U}$  is the velocity vector,  $\lambda$  stands for the thermal conductivity,  $T$  is the static temperature,  $\boldsymbol{\tau}$  is the shear stress and  $\mathbf{S}_M, \mathbf{S}_E$  are the momentum and energy sources, respectively. The term  $\nabla \cdot (\mathbf{U} \cdot \boldsymbol{\tau})$  represents the work due to viscous stresses which is usually negligible but is activated for the heat transfer model.

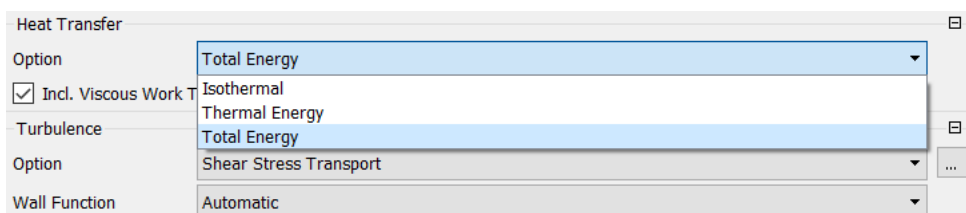


Figure 4.10 Selection of the heat transfer model.

From the RANS based turbulence models available in CFX, the Shear Stress Transport (SST) k- $\omega$  model was selected. This model is extensively used for CFD analysis in turbomachinery as it is expected to provide accurate calculations for the boundary layer, simulating both the viscous sublayer and the log-law layer, as well as valid predictions of the amount of flow separation under adverse pressure gradients, like the one existing within the intercompressor duct. If higher accuracy was desired, with no concern for the simulations' computational cost the Reynolds Stress Model (RSM) or the Large Eddy Simulation (LES) approach could have been used.



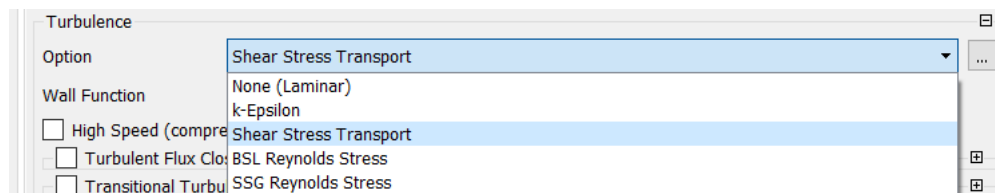


Figure 4.11 Selection of the turbulence model.

## 4.2.2 Boundary Conditions

For the hub and shroud walls the No Slip condition is used and the walls are, ideally, considered to be smooth. The periodic interfaces of the domain are “connected” via a rotational periodicity condition, as seen in Figure 4.13.



Figure 4.12 Boundary conditions for duct walls.

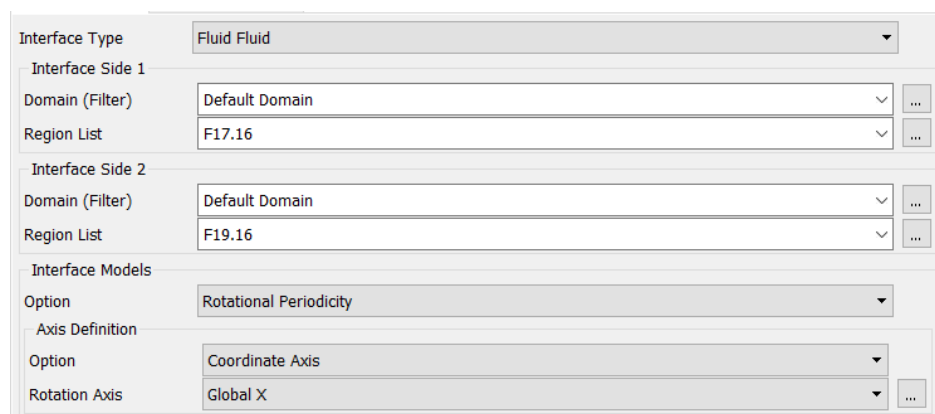


Figure 4.13 Conditions at the periodic interface.

The subsonic inlet flow is set to be normal to the boundary, in terms of cartesian components. This choice is valid since an extended straight part has been added to the inlet of the duct which allows the flow to be directed correctly towards the S-duct. The total pressure and total temperature are specified at the inlet of the duct and their values are calculated for the simulated engine as explained in Section 4.4.2.

The turbulence intensity should also be specified in this tab. The intensity is defined as in (4.7), where  $u$  is the fluctuating velocity component due to turbulence and  $U$  is the velocity magnitude.

$$I = \frac{u}{U} \quad (4.7)$$

The intensity is set to Medium or 5%, which is common value for HPC and is suggested to be used when there is not enough available information for the inlet turbulence. [44]

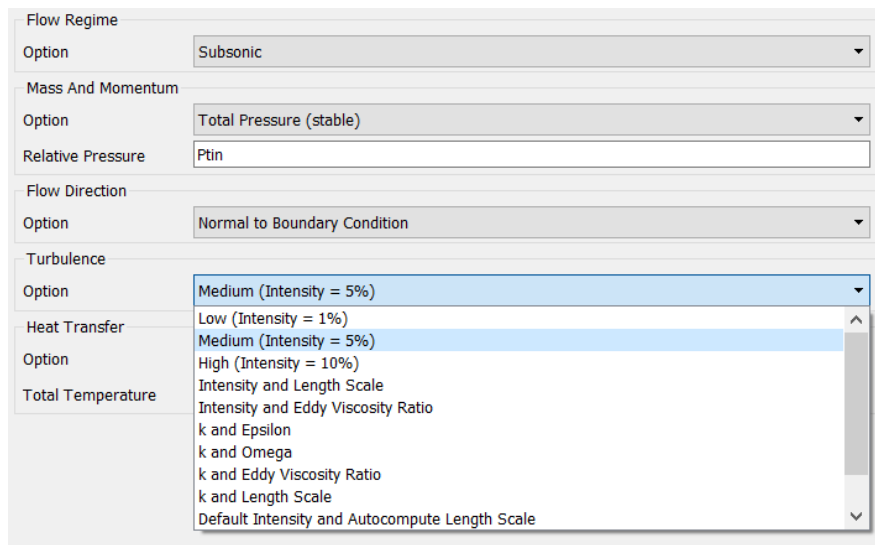


Figure 4.14 Inlet boundary conditions.

For the subsonic outlet the total mass flow rate is specified. Since only a slice of the annular duct is simulated the respective mass flow should be given. However, by setting the Mass Flow Rate Area to “Total for All Sectors”, as observed in Figure 4.15, the rotational periodicity is considered and the total mass flow rate for the duct can be used as input.



Figure 4.15 Outlet boundary conditions.

After applying all the boundary conditions the fluid domain is shown in Figure 4.16.

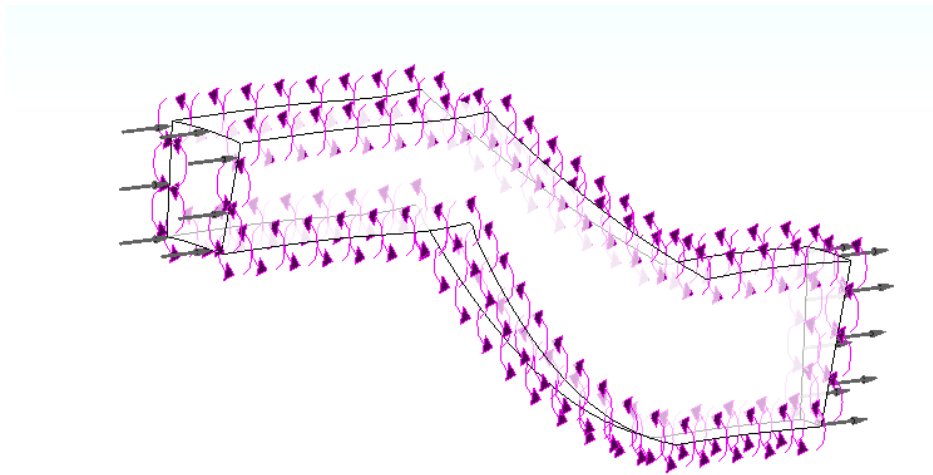


Figure 4.16 Fluid domain with the boundary conditions visible.

### 4.2.3 Solver Control

In the solver control tab of CFX-Pre the first option that need to be defined is the Advection Scheme used. More specifically, at the solving numerical process the variables' values at the integration points are approximated in terms of nodal values. A general description of all the advection schemes available is given by equation (4.8).[37]

$$\varphi_{ip} = \varphi_{up} + \beta \nabla \varphi \Delta \vec{r} \quad (4.8)$$

Where  $\varphi$  represents a general scalar variable,  $ip$  and  $up$  denote the integration point and upwind node with  $\vec{r}$  being the vector from the latter to the first one. The selection of the blend parameter  $\beta$  determines the scheme used.

When  $\beta = 0$  the first order Upwind Scheme is applied. This approach is very robust but introduces significant discretization errors and thus is not the one selected for the simulation. For the Specified Blend Factor scheme the value of  $\beta$  is chosen to be between 0 and 1. The choice  $\beta = 1$  yields a second order scheme which is accompanied by a higher computational cost. In the High-Resolution Scheme, which is selected for the simulation in this work,  $\beta$  value is selected by the program based on the local solution field. In regions where the variable gradients are low the blend factor is set close to 1, to reach the desired accuracy, while in areas of sharp gradient changes,  $\beta$  is set closer to 0, to maintain robustness. The High-Resolution scheme is selected for the turbulence advection scheme, as well. The choice of this scheme is also discussed in the following Section 4.4.1.

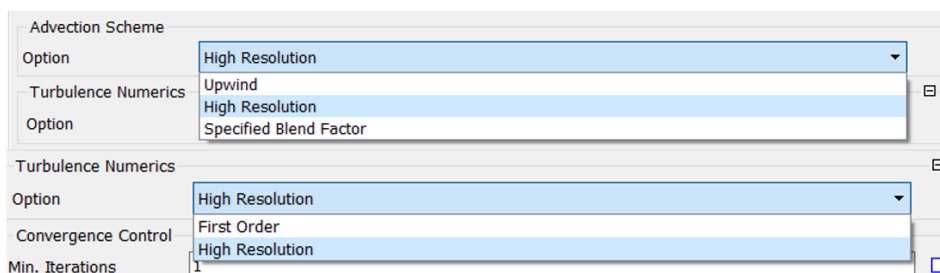


Figure 4.17 Selection of advection scheme.

Additionally, at this tab the convergence criteria of the simulation are specified with the residual type set to RMS.

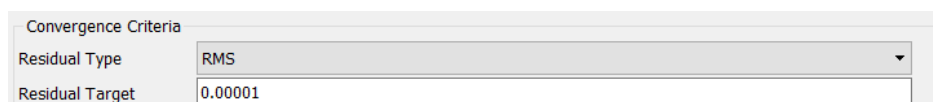


Figure 4.18 Selection of residual type and target.

Finally, CFX-Pre gives the possibility to monitor the values of interest during the numerical simulation, by creating a corresponding expression. In the case of the S-duct the value of interest is the total pressure difference at the inlet and outlet of the duct as a fraction of the total inlet pressure, as defined by equation (2.4).

### 4.3 Post Processing

ANSYS CFX offers many different post processing tools for obtaining contours, streamlines, particle tracks as well as variables' charts. To be able to take advantage of the program's possibilities the simulation results are loaded in CFX-Post where two new planes along the S-duct are created. These planes are placed at the inlet and outlet of the duct, after and before the straight extensions, correspondingly. The first plane is referred to as *InPlane* while the outlet one is called *OutPlane*.

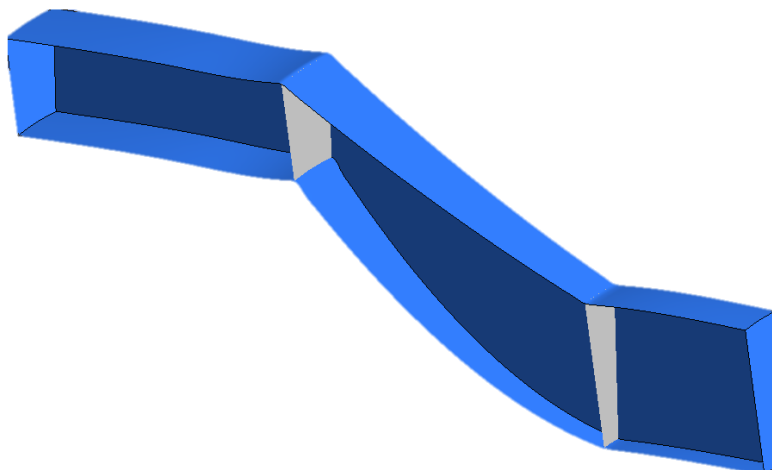


Figure 4.19 Definition of additional planes.

These additional planes are used to acquire the values for the flow variables as well as to calculate the flow losses factors. The variables of interest are defined as expressions and are calculated using the integrated functions, as seen in Figure 4.20.

	Psinduct	<i>massFlowAve(Pressure)@InPlane</i>
	Ptinduct	<i>massFlowAve(Total Pressure)@InPlane</i>
	Ptoutduct	<i>massFlowAve(Total Pressure)@OutPlane</i>
	Min	<i>massFlowAve(Mach Number)@Inlet</i>
	Mout	<i>massFlowAve(Mach Number)@Outlet</i>
	wduct	<i>(Ptinduct-Ptoutduct)/(Ptinduct-Psinduct)</i>
	dPqP	<i>(Ptinduct-Ptoutduct)/Ptinduct</i>
	ypmax	<i>maxVal(Yplus)@Default Domain Default</i>
	CpStatic	<i>(Pressure-Ptinduct)/(Ptinduct-Psinduct)</i>

Figure 4.20 Definition of expressions.

The function mostly used for the computation is *massFlowAve()* which calculates the mass flow-weighted average of the variable specified within the parenthesis. The variables  $P_{s_{induct}}$ ,  $P_{t_{induct}}$ ,  $P_{t_{outduct}}$  correspond to the static and total pressure at InPlane and the total pressure OutPlane, respectively.  $M_{in}$ ,  $M_{out}$  are the Mach number at the inlet and outlet of the duct which are considered design parameters, as explained in Section 3.2.

The variables associated with the pressure losses are  $\omega_{duct}$ , which is the total pressure loss coefficient and  $dPqP = DP/P$  that is the total pressure loss as a fraction of the total inlet pressure.  $C_{p_{static}}$  is the coefficient of static pressure which can be calculated along the streamlines inside the duct.

The expression for  $ypmax = y_{max}^+$  is defined via the function *maxVal()* which returns the maximum value of the specified variable. The maximum value of  $y^+$  in the near wall region is important since by its monitoring it can be assured that the limits set are respected, and the boundary layer is accurately resolved.

## 4.4 Flow Simulation for the Base Case

The flow in the digitized duct of the GE90 turbofan engine was the first one simulated. Through the digitization and the parametrization process it is possible to acquire the full geometry of the S-Duct, meaning the hub and shroud radii in different axial positions, which are given, in the suitable format, as inputs to ANSYS DesignModeler. This way a three-dimensional model of the intercompressor duct is generated. The basic dimensions of the GE90's S-Duct, derived as described in Chapter 3, are given in Table 4.1 and Figure 4.21.

<b>L (m)</b>	0.5088
<b>R<sub>hub<sub>in</sub></sub> (m)</b>	0.6112
<b>R<sub>shroud<sub>in</sub></sub> (m)</b>	0.7757
<b>A<sub>in</sub> (m<sup>2</sup>)</b>	0.7166
<b>R<sub>hub<sub>out</sub></sub> (m)</b>	0.3586
<b>R<sub>shroud<sub>out</sub></sub> (m)</b>	0.4812
<b>A<sub>out</sub> (m<sup>2</sup>)</b>	0.2360

Table 4.1 Basic Dimensions of GE90's duct.

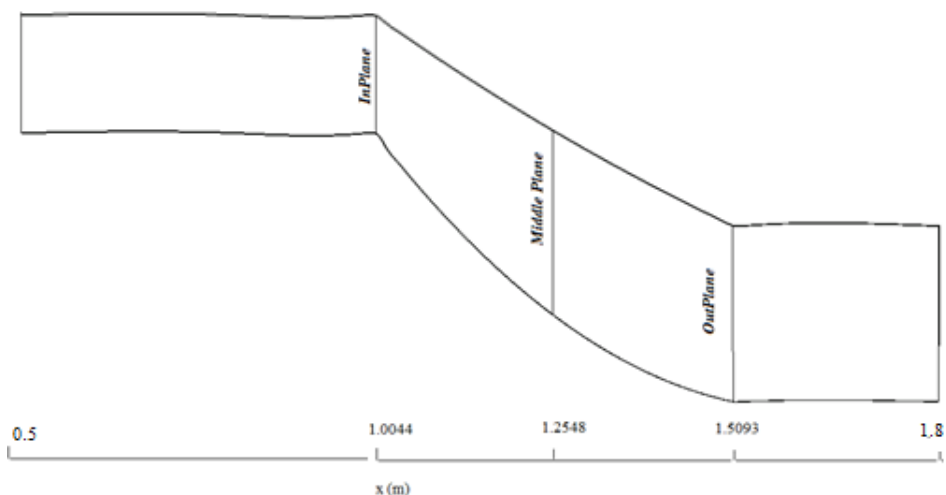


Figure 4.21 Sketch of the modelled duct and its dimensions.

### 4.4.1 Mesh Independence Study

In order to ensure the convergence of the CFD simulation certain criteria need to be satisfied. Analytically, the residual RMS Error should have an acceptable value, typically  $10^{-4}$  or  $10^{-5}$ , and the values of interest should have reached a steady solution. However, even if the simulation is converged, the solution should be independent of the mesh resolution. As a result, a mesh or grid independence study should always be carried out.

For the examined S-Duct mesh element size was used as an input parameter in ANSYS Workbench. By simulating the flow for gradually reduced element size and calculating the value of  $DP/P$ , for each case, a solution was reached that remained unchanged as the mesh

was refined. As the element size is reduced the number of mesh nodes is significantly increased leading to a higher computational cost. Thus, a compromise is made between cost and accuracy by choosing the coarser mesh possible.

The grid independence study was carried out using both the Upwind and the High-Resolution advection scheme, as presented in Table 4.2 and Figure 4.22. It is evident that for the High-Resolution scheme the mesh independence is achieved for approximately 70000 nodes, whereas for the Upwind scheme the pressure losses continue to reduce as the mesh is refined. This is in accordance with the observations made by Yurko et al. in [46] and justifies the choice of the High-Resolution convection scheme.

Mesh Statistics		Upwind Scheme		High Resolution Scheme	
Element Size (m)	Nodes	DP/P	$\omega$	DP/P	$\omega$
0.050	20088	0.02861	0.23340	0.01854	0.14219
0.030	30876	0.02863	0.23405	0.01903	0.14711
0.015	71020	0.02713	0.21805	0.01811	0.13668
0.005	795760	0.02507	0.19625	0.01814	0.13686

Table 4.2 Grid Independence Study.

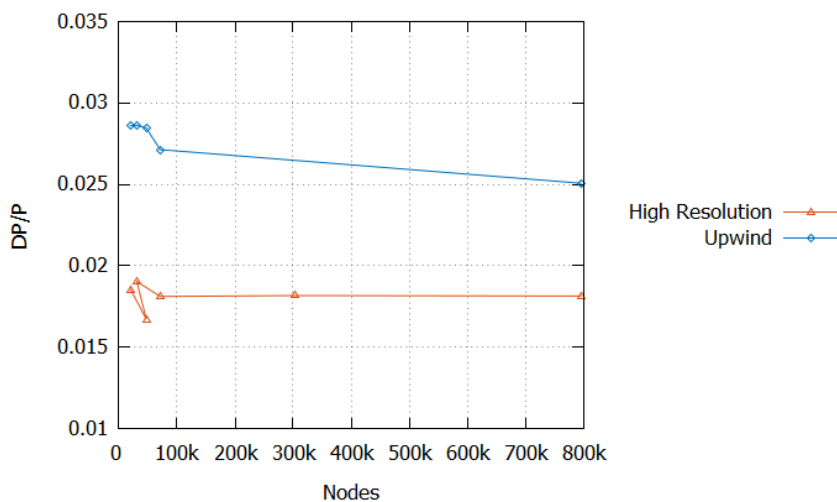


Figure 4.22 Grid Independence Study.

In all the above cases a value of  $y^+ < 2$  was maintained, for the viscous sublayer to be fully resolved. However, for the chosen element size the pressure losses were also calculated for higher values of  $y^+$ .

$y^+$	Nodes	DP/P	$\omega$
1	71020	0.01811	0.13668
20	61480	0.01816	0.13721
100	60420	0.01722	0.12696

Table 4.3 Pressure Losses for different  $y^+$ .

From Table 4.3, it is clear that for higher  $y^+$  the loss factor is underestimated since the boundary layer is not fully resolved. Although the change for  $y^+ \approx 20$  is not significant, a value approximately equal to unity was chosen to provide a more accurate estimation.

The mesh generated for the S-duct and its refinement near the wall can be observed in Figure 4.23 and Figure 4.24.

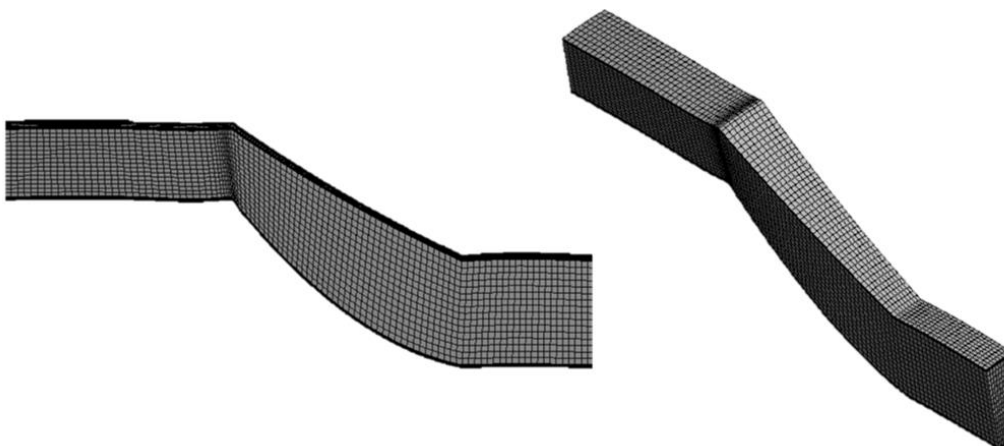


Figure 4.23 Generated Mesh.



Figure 4.24 Mesh inflation near the wall.

#### 4.4.2 Boundary Conditions

In order to define the necessary boundary conditions a MATLAB script was used. The script provided the values of the main parameters, such as total pressure, total temperature, mass flow rate, enthalpy and entropy, at every position along the turbofan engine using the basic thermodynamic equations. The data used to define the operating conditions, the fuel consumption, the pressure ratios and the efficiency of the engine's components were found in bibliography. The pressure losses in the different parts of the engine, that are not compressors or turbines with available pressure ratios, were estimated as described in [8]. The values calculated for the boundary conditions at the inlet and the outlet of the duct are included in Table 4.4.

$P_{t_{in}}$ (bar)	1.6565
$T_{t_{in}}$ (K)	329.5315
$\dot{m}$ (kg/s)	149.8941

Table 4.4 Calculated Boundary Conditions.



To facilitate the simulation the boundary conditions were converted to correspond to the standard temperature and pressure,  $P_{ref} = 1.01325\text{bar}$ ,  $T_{ref} = 288.15\text{K}$ , using equation (4.9). The final boundary conditions as defined in the setup of the flow simulation are shown in Figure 4.25.

$$\dot{m}_{eq} = \dot{m} \sqrt{\frac{P_{tin}}{P_{ref}}} \sqrt{\frac{T_{ref}}{T_{tin}}} \quad (4.9)$$

Expressions

$\sqrt{\alpha}$ Ptin	1.01325 [bar]
$\sqrt{\alpha}$ Ttin	288.15 [K]
$\frac{PP}{TCL}$ m	100 [kg s <sup>-1</sup> ]

Figure 4.25 Applied Boundary Conditions.

### 4.4.3 Results

After the convergence and the completion of the simulation the results are available for post processing, as described in Section 4.3. The main parameters of interest calculated by the program are presented in Table 4.5. These values are within the suggested, empirical, limits given in [8], shown in Figure 2.7.

Parameter	CFX Result
$M_{in}$	0.36187
$M_{out}$	0.59663
$\omega$	0.13668
$DP/P$	1.811%

Table 4.5 Results for Mach and losses.

In addition to the calculation of the flow variable CFX-Post also offers the possibility to visualize the flow within the duct through contours and streamlines, as well as to create graphs for the basic parameters. In these graphical representations the values on the X axis are the ones obtained by the digitization of the engine, seen in Figure 4.21.

A better understanding of the developed flow in the S-duct is obtained by observing the velocity streamlines and the velocity contour along it. As it is seen in Figure 4.26, a vast separation region can be identified near the hub wall after the first bend. The position where the phenomenon occurs is expected since there the fluid is subjected to a large adverse pressure gradient. In Figure 4.27 the distributions of Total Pressure and Static Pressure along the duct are shown.

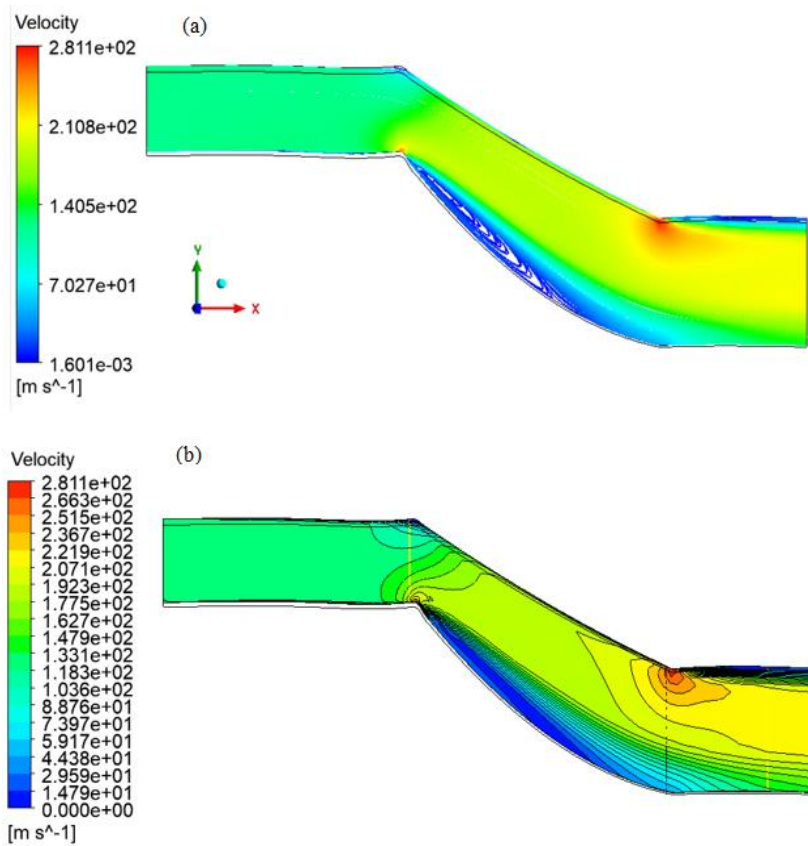


Figure 4.26 Velocity (a)Streamlines and (b)Contour.

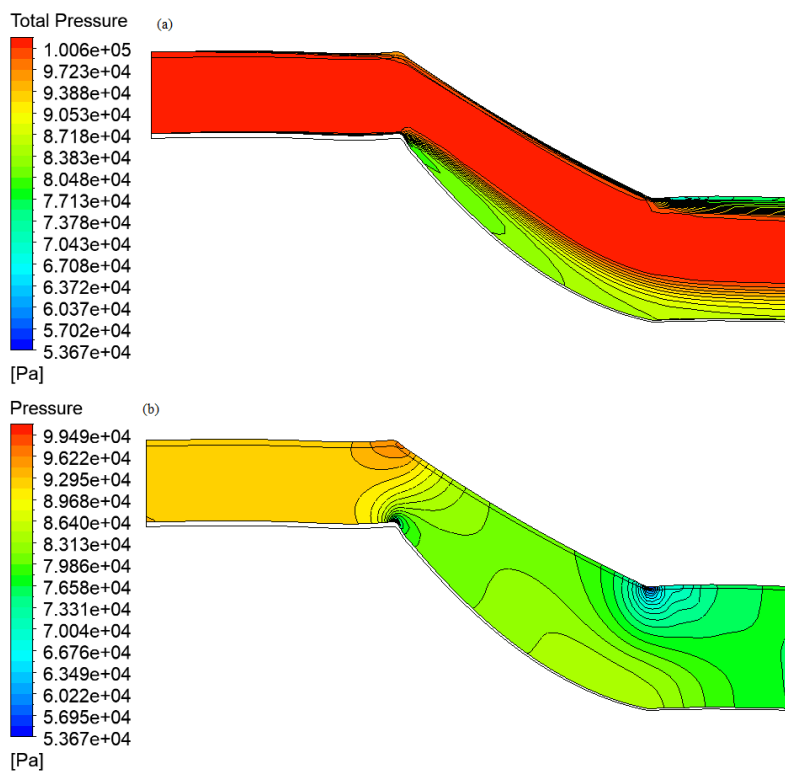


Figure 4.27 (a)Total Pressure and (b)Static Pressure Distribution.

The existence of the adverse pressure gradient at the first bend of the duct is confirmed by the chart of the axial variation of static pressure coefficient along the duct, seen in Figure 4.28. A less severe reversed adverse pressure gradient can be also noticed at the second bend, downstream where another, smaller, separation area is located, near the shroud wall.

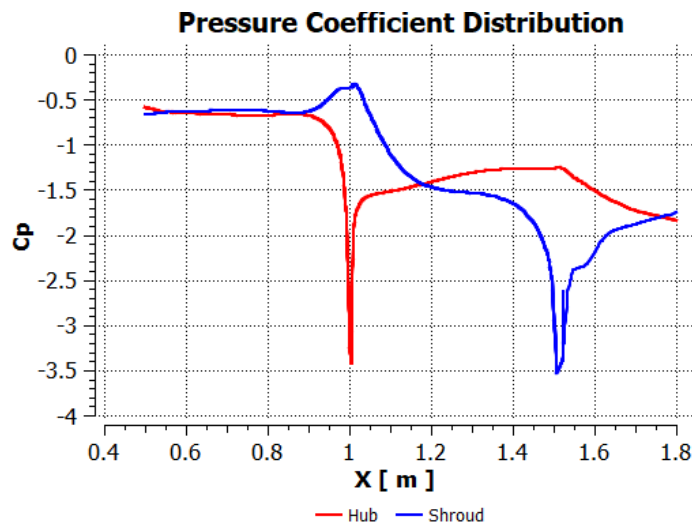


Figure 4.28 Static Pressure Coefficient Distribution.

In Figure 4.29, the outlet and middle axial velocity profile is shown. As it was expected, near the shroud and hub wall the velocity is significantly lower than in the middle of the duct's cross section due to the appearance of separation phenomena.

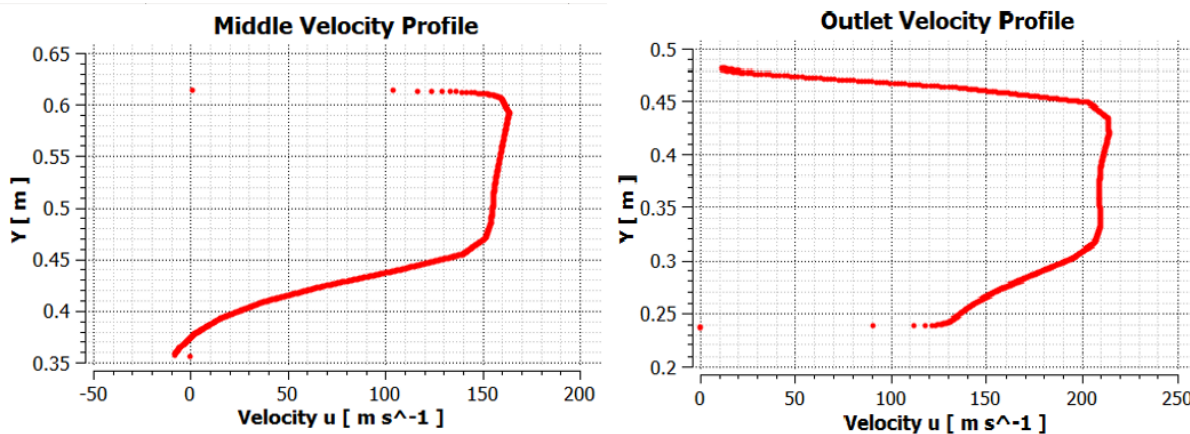


Figure 4.29 Velocity Profiles.

Finally, the  $y^+$  values along the hub and shroud wall can be plotted to confirm that the value is not larger than the desired and that the viscous sublayer of the boundary layer is fully resolved.

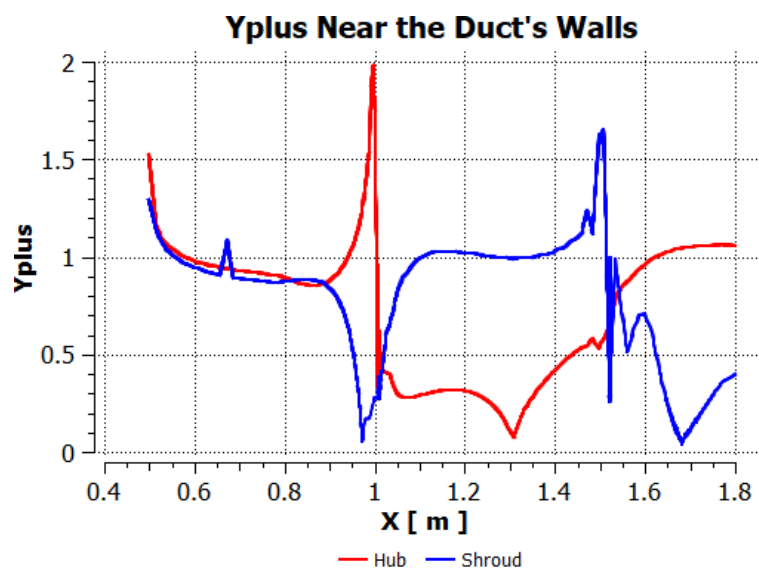


Figure 4.30  $Y^+$  distribution.

## Chapter 5 Development and Validation of Model for Estimation of Losses

In this Chapter the algebraic model created for the estimation of pressure losses within the duct is analyzed. The variation of losses with the variables used for the parametrization of the S-duct's geometry is examined and the curves fitting better to the results are presented. Finally, a validation of the produced model is presented.

### 5.1 Parametric Study

The main parameters used for the description of the intercompressor duct's geometry are introduced in Chapter 3. From them, the ones whose influence on the losses is analyzed are:  $a_{2shroud}$ ,  $\frac{\Delta R}{L}$ ,  $\frac{h_{in}}{L}$  and  $\frac{R_{min}}{L}$ . For the parameter  $\frac{A_{out}}{A_{in}}$  it was observed that the losses are not significantly affected and a clear correlation could not be found. The new geometries arising from the variation of the parameters were obtained using the processes described in Section 3.3. In addition to the above-mentioned variables, the correlation of the losses with the mass flow rate, for a fixed duct geometry, is studied.

In most of the cases examined, the parameters and the pressure loss factor are expressed as a fraction of their reference values. The reference values correspond to the ones calculated during the parametrization process for the S-duct of GE90, which was selected as the base case in this work. The values of the parameters are contained in Table 5.1.

Parameter	Reference Values
$A_{out}/A_{in}$	0.7707
$\Delta R/L$	0.6581
$h_{in}/L$	0.3232
$R_{min}/L$	1.3629

Table 5.1 Reference Values.

#### 5.1.1 Influence of $a_{2shroud}$

As it is presented in Section 3.2.2,  $a_{2shroud}$  is used to express the curvature of the duct and from it all the parameters used to describe the radii and area distributions can be derived.

Some of the different geometries generated with the variation of  $a_{2shroud}$  versus the non-dimensional distance  $x$  are shown in Figure 5.1.

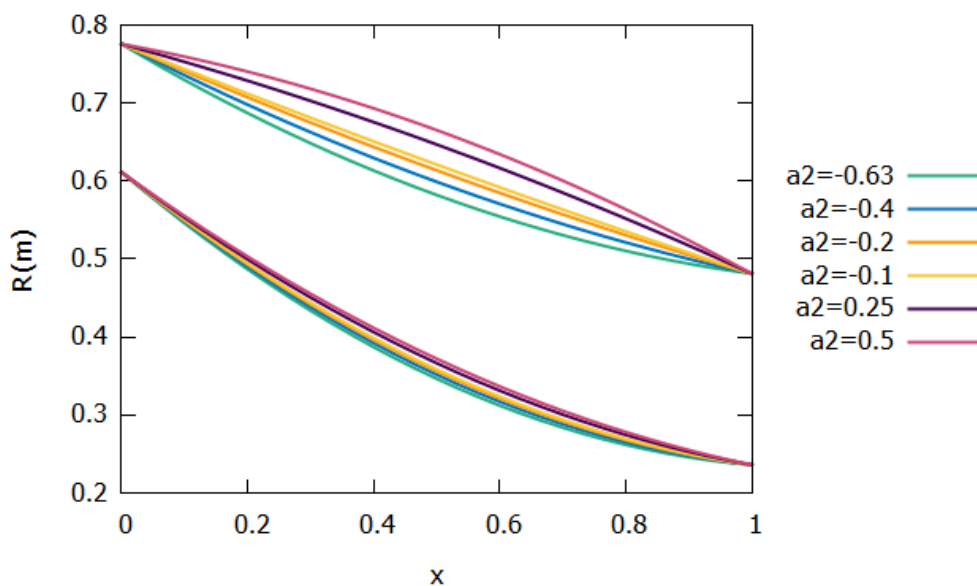


Figure 5.1 Duct's shapes for different  $a_{2shroud}$ .

The pressure loss factor for each duct was obtained from the CFD simulation for boundary conditions corresponding to the design point, given in Section 4.4.2. From the results, in Table 5.2, it is suggested that for higher values of  $a_{2shroud}$  the pressure losses are decreased. This conclusion is justifiable since, as  $a_{2shroud}$  is rising, the curvature of the shroud wall is almost reversed and the duct tends to lose its S shape, which is mainly responsible for the appearance of separation phenomena and increased losses. The flow within the different ducts is visible in Figure 5.2.

$a_{2shroud}$	$DP/P$
-0.63	2.923%
-0.4	2.144%
-0.2	1.811%
-0.1	1.774%
0.25	1.562%
0.5	1.519%

Table 5.2 Losses Factor for different  $a_{2shroud}$ .

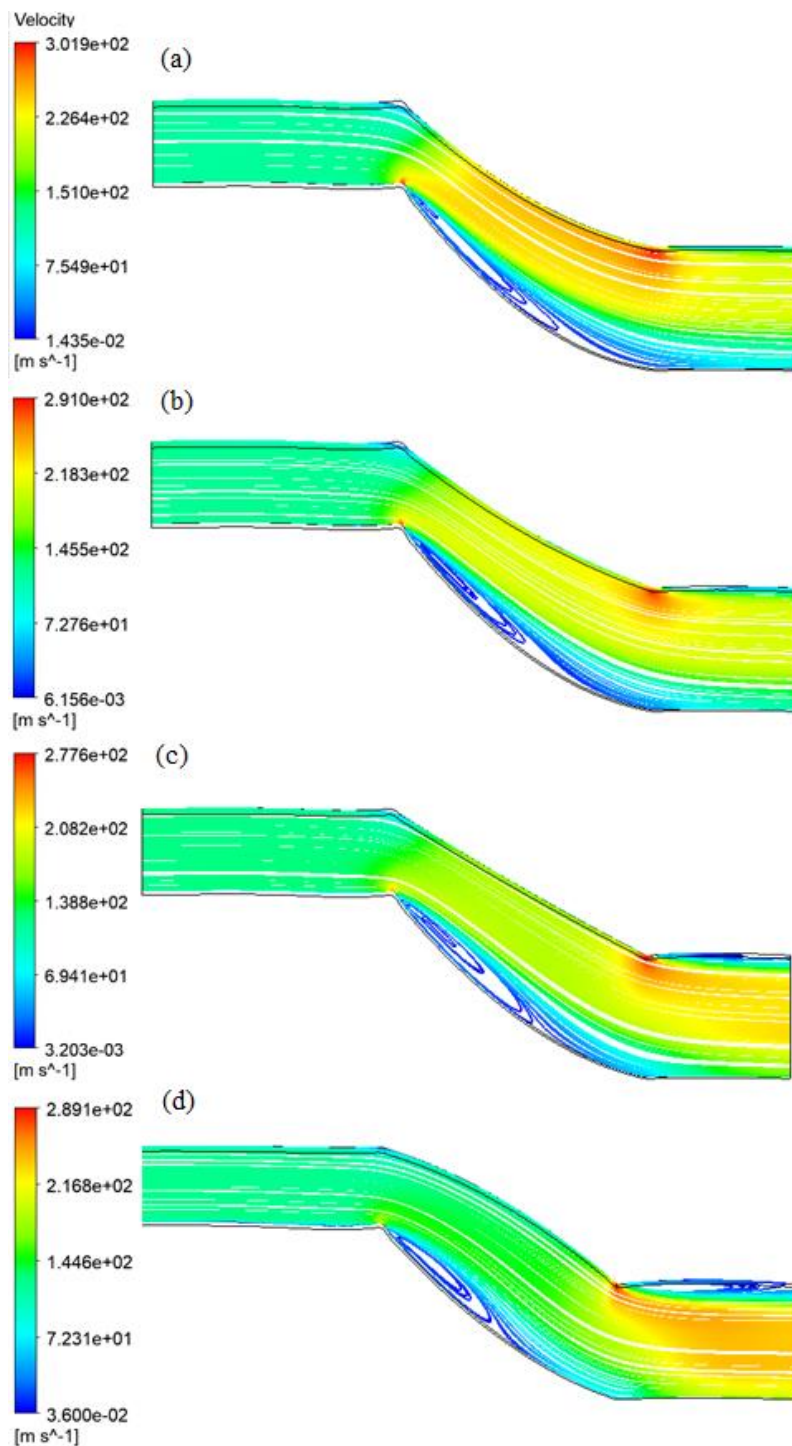


Figure 5.2 Streamlines for  $a_{2shroud}$  (a) -0.63,(b)-0.4,(c)-0.1,(d)0.5.

The second order polynomial curve given by equation (5.1) could be used to describe the correlation between  $a_{2shroud}$  and the pressure loss factor, calculated for the reference values of the design parameters. For the curve fitting a non-linear squares (NLLS) Marquardt-Levenberg algorithm was implemented.

$$(DP/P)_{ref} = 0.01691a_{2shroud}^2 - 0.00922a_{2shroud} + 0.01607 \quad (5.1)$$

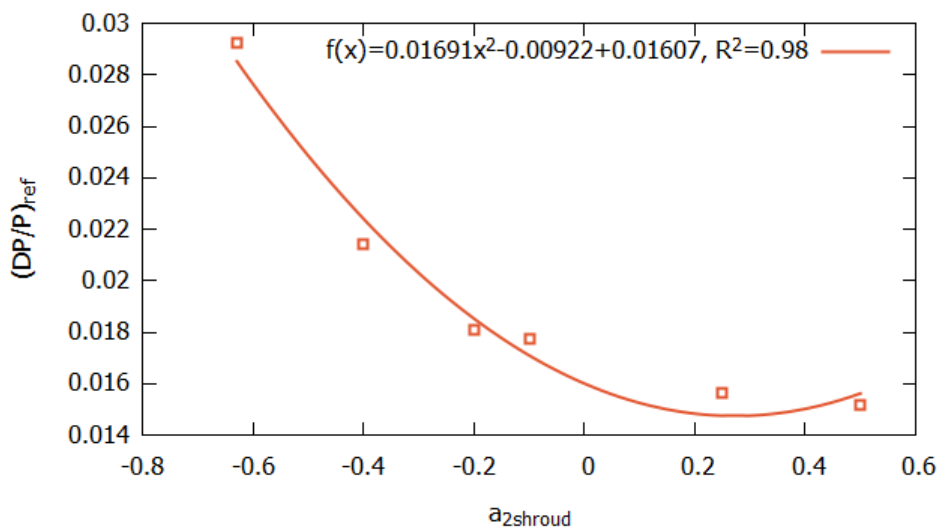


Figure 5.3 Correlation of  $DP/P$  and  $a_{2shroud}$ .

### 5.1.2 Influence of $\Delta R/L$

The parameter  $\Delta R/L$  is of great significance as it is a measure of the aggressiveness of the duct. More specifically, an increase to  $\Delta R/L$  corresponds either to larger radial offset or to a shortening of the duct. In both cases the pressure losses are expected to rise, since the separation is expanded, based on findings analyzed in the bibliography.

These assumptions are confirmed by the flow simulation conducted for intercompressor ducts of different  $a_{2shroud}$ . In Figure 5.4, the streamlines within the S-duct with  $a_{2shroud} = -0.2$  are shown for four different lengths, as percentages of the reference length of the duct. It is observed that as the total length is increased the separation area is compressed until the length is doubled, where the separation is almost non-existent.



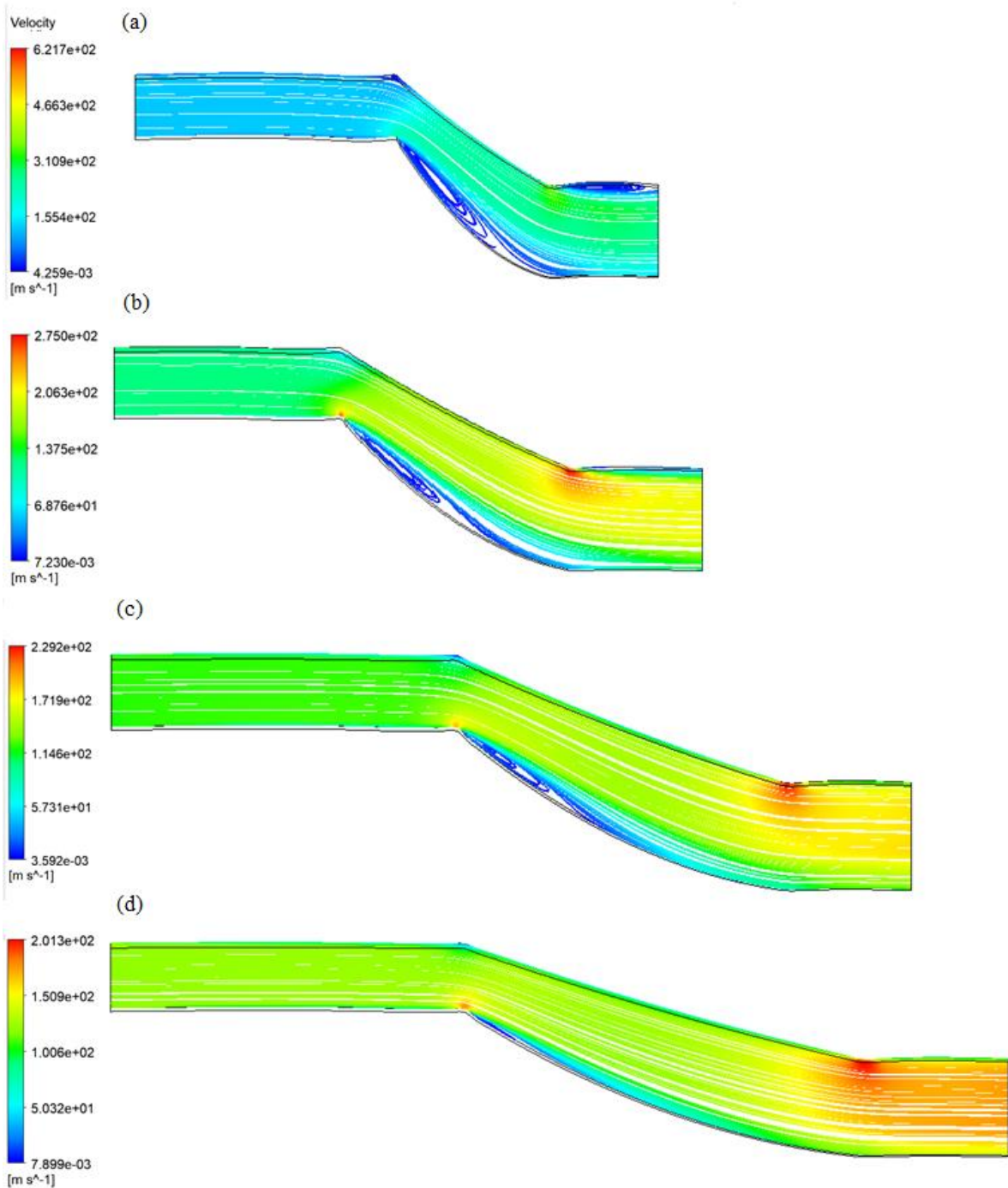


Figure 5.4 Streamlines for (a)80%, (b)100%, (c)150%, (d)200% of duct's reference length.

Similar observations can be made from Figure 5.5, where the streamlines for three different radial offsets are shown. As the radial offset is decreased the duct is considered less aggressive and the separation is constrained.

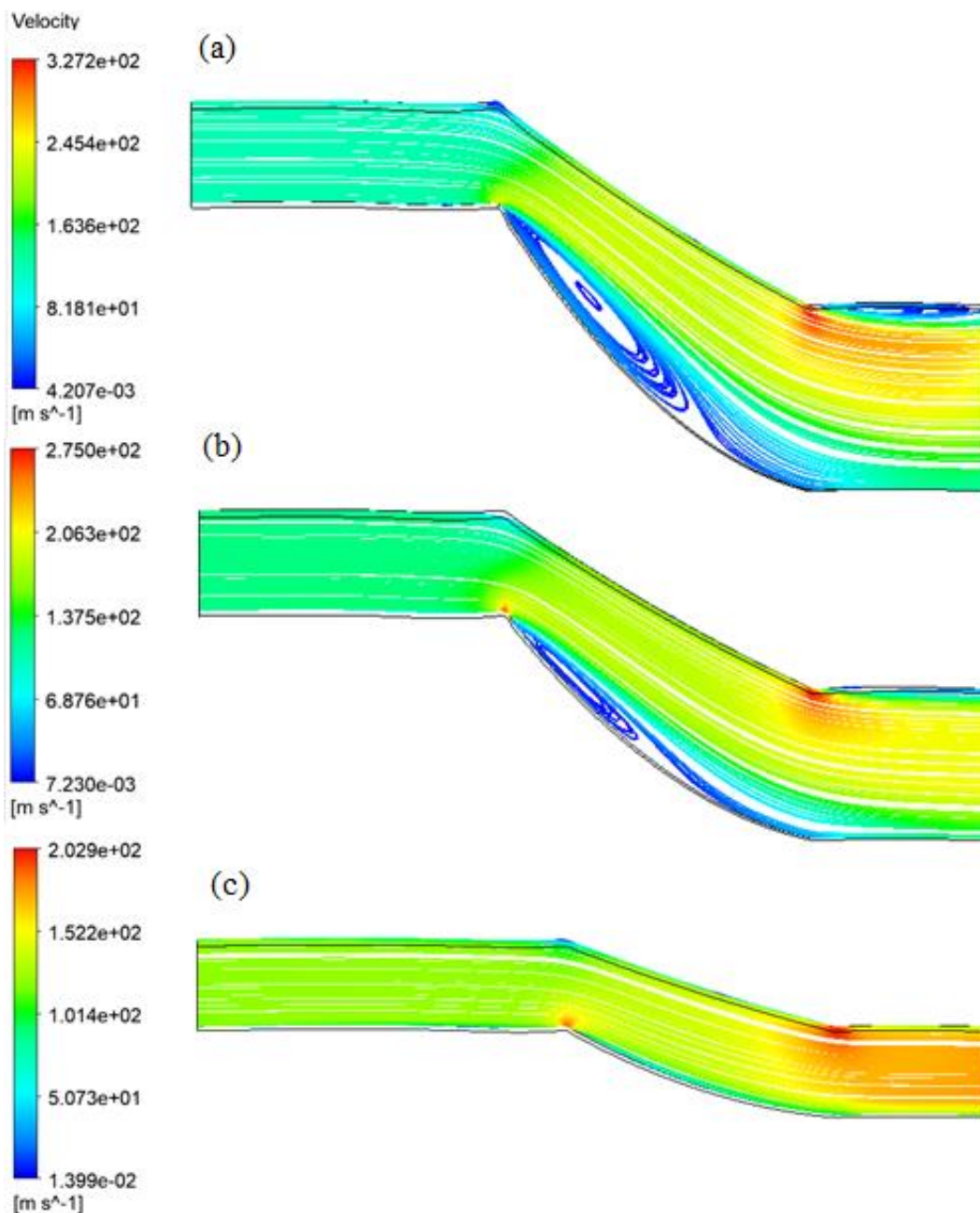
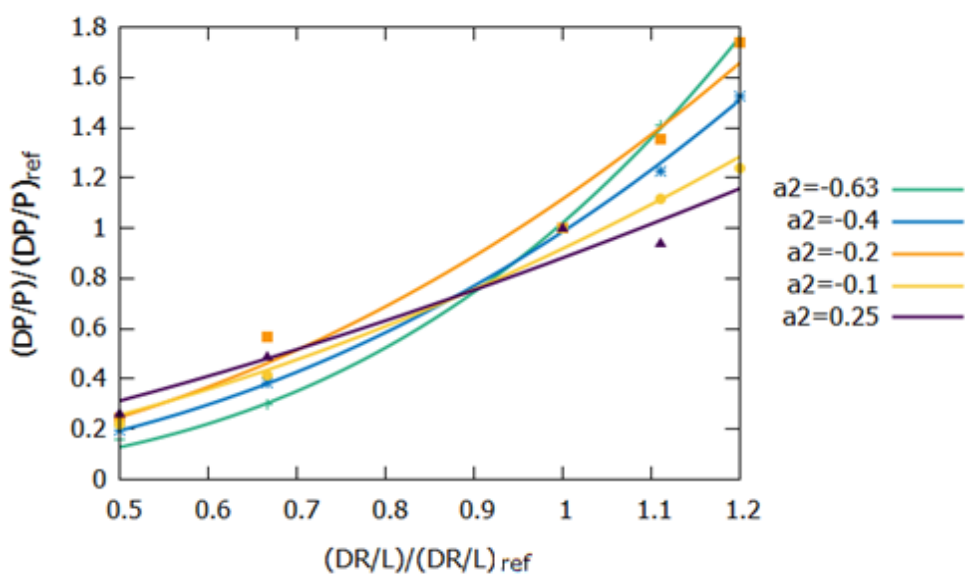


Figure 5.5 Streamlines for (a)120%, (b)100%, (c)50% of reference radial offset.

The exact non-dimensional loss factors calculated while varying the parameter  $\Delta R/L$  are shown in Table 5.3. For every geometry it is possible to describe the variation of losses with an exponential curve like (5.2), derived by least squares curve fitting.

$$\frac{DP/P}{(DP/P)_{ref}} = b_1 \left[ \frac{\Delta R/L}{(\Delta R/L)_{ref}} \right]^{b_2} \quad (5.2)$$

$a_{2_{shroud}}$	$\frac{\Delta R/L}{(\Delta R/L)_{ref}}$	$\frac{DP}{P}$	$\omega$	$b_1$	$b_2$
-0.63	111%	4.125%	0.2555	1	2.9854
	100%	2.923%	0.1858		
	67%	0.877%	0.0684		
	50%	0.459%	0.0405		
-0.4	120%	3.271%	0.2162	0.9851	2.3371
	111%	2.630%	0.1666		
	100%	2.144%	0.1489		
	67%	0.827%	0.0688		
	50%	0.415%	0.0381		
-0.2	120%	3.155%	0.2326	1.1156	2.1655
	111%	2.459%	0.1821		
	100%	1.811%	0.1367		
	67%	1.031%	0.0946		
	50%	0.447%	0.0570		
-0.1	120%	2.198%	0.1591	0.9182	1.8354
	111%	1.978%	0.1444		
	100%	1.774%	0.1411		
	67%	0.735%	0.0657		
	50%	0.393%	0.0381		
0.25	111%	1.472%	0.1222	0.8815	1.4907
	100%	1.562%	0.1418		
	67%	0.763%	0.0747		
	50%	0.412%	0.0420		

Table 5.3 Variation of loss factor with  $\Delta R/L$ .Figure 5.6 Correlation of  $DP/P$  and  $\Delta R/L$  for different  $a_{2_{shroud}}$ .

It can be noticed that there is no clear correlation of the function's coefficients and  $a_{2_{shroud}}$ , as a result an equation could be used to describe the influence of  $\Delta R/L$  on the losses without any dependence on  $a_{2_{shroud}}$ . By excluding some outliers, which are the values not fitting to the pattern found, and are usually corresponding to extreme duct geometries, it is possible to use the exponential function (5.3) to describe the connection shown in Figure 5.7.

$$\frac{DP/P}{(DP/P)_{ref}} = 1.0245 \left[ \frac{\Delta R/L}{(\Delta R/L)_{ref}} \right]^{2.2462} \quad (5.3)$$

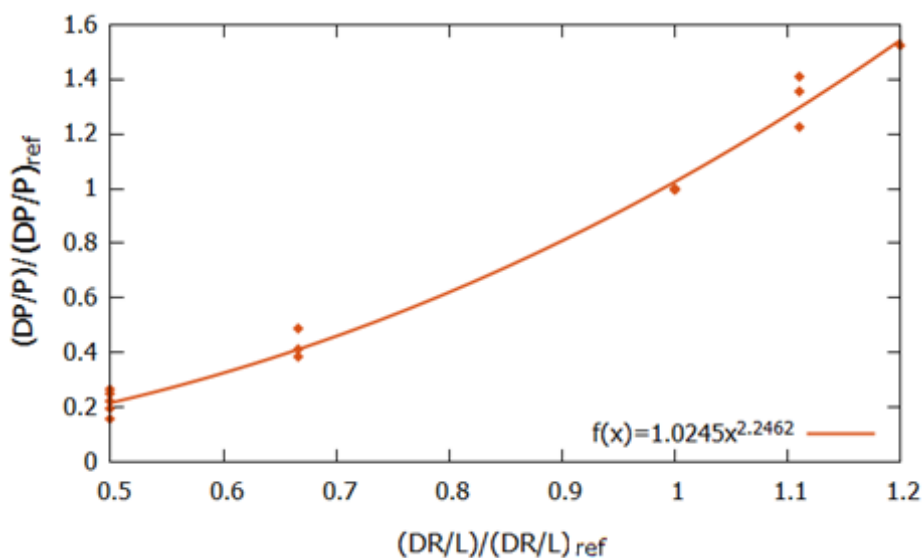


Figure 5.7 Correlation of  $DP/P$  and  $\Delta R/L$ .

### 5.1.3 Influence of $h_{in}/L$

The parameter  $h_{in}/L$ , which, reversed, is also referred to as non-dimensional length, dictates the size of any axial pressure gradient developed. The influence of this parameter on the losses for different duct geometries was examined. It should be mentioned that since  $h_{in}$  is the height at the inlet of the duct, as the parameter was reduced or increased the inlet area was also changed. As a result, to examine the flow within the duct for several values of the parameter, without increasing the Mach numbers, the mass flow rate should also be differentiated.

The values assigned to  $h_{in}/L$  are within the range found from the parametrization of the engines in Section 3.2.1. In Figure 5.8 the streamlines developed within the duct for certain non-dimensional lengths along with the corresponding static pressure coefficient distributions, are displayed. These correspond to the flow simulation for the duct with  $a_{2_{shroud}} = -0.2$ , while similar results were produced for all the examined geometries.

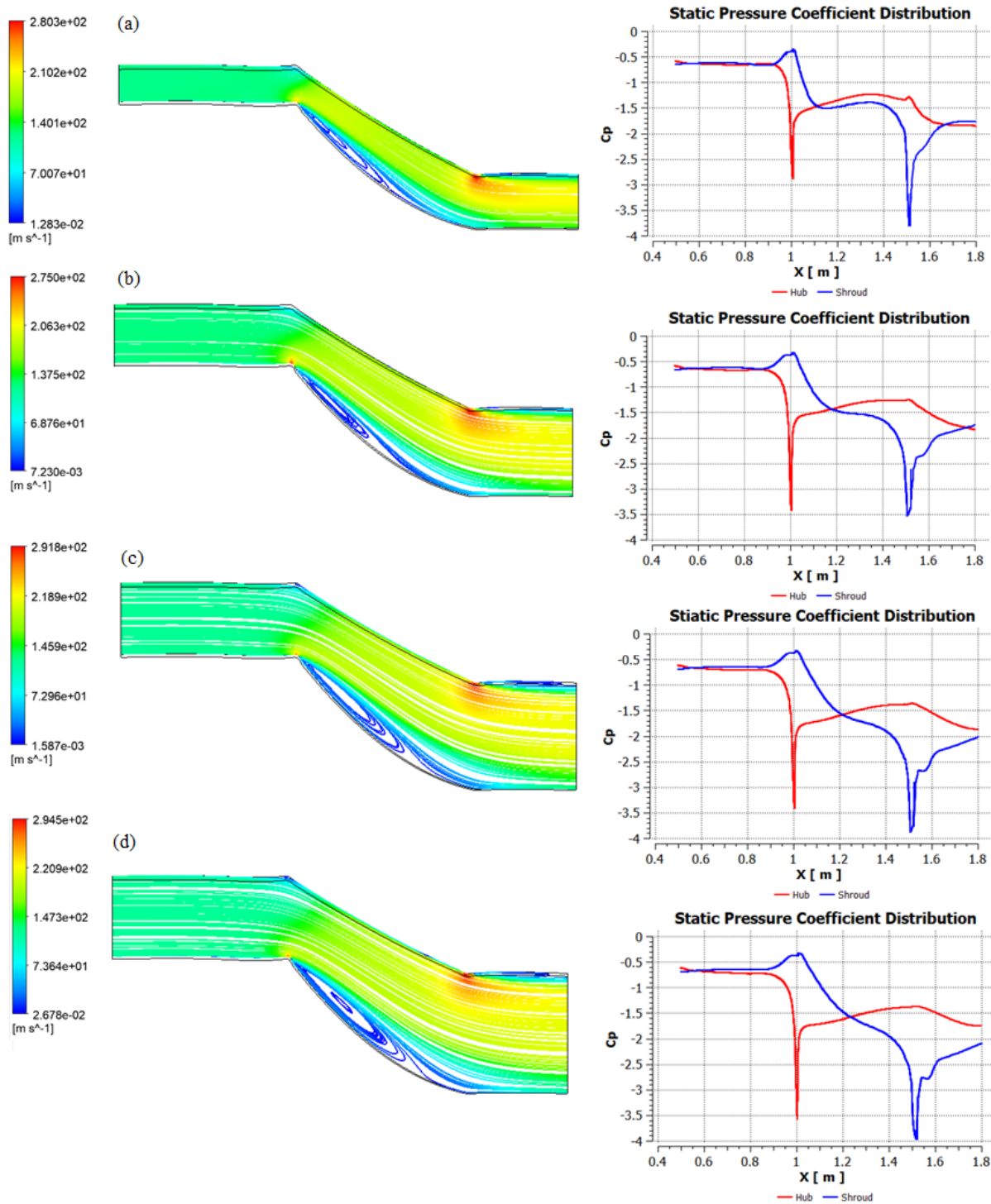
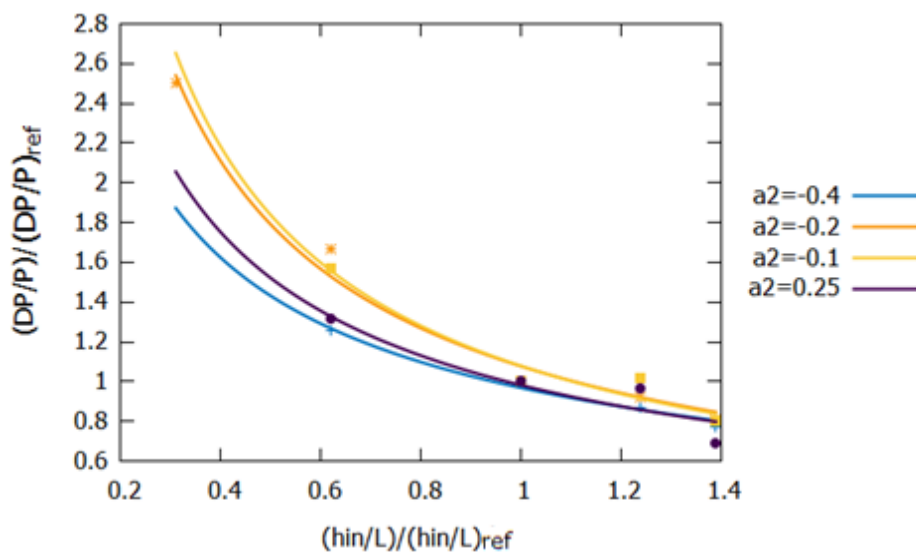


Figure 5.8 Streamlines and  $C_p$  distribution for (a)62%, (b)100%, (c)124%, (d)139% of  $(h_{in}/L)_{ref}$ .

The pressure loss factors corresponding to each case are shown in Figure 5.9 and Table 5.4. By implementing a non-linear least squares method it is possible to find an algebraic expression that describes the correlation between the examined parameter and the losses for the different  $a_{2shroud'}$  given by (5.4).

$$\frac{DP/P}{(DP/P)_{ref}} = c_1 \left[ \frac{h_{in}/L}{(h_{in}/L)_{ref}} \right]^{c_2} \quad (5.4)$$

$a_{2,shroud}$	$\frac{h_{in}/L}{(h_{in}/L)_{ref}}$	$\frac{DP}{P}$	$\omega$	$c_1$	$c_2$
-0.4	62%	3.271%	0.2162	0.9684	-0.5631
	100%	2.630%	0.1666		
	124%	2.144%	0.1489		
	139%	0.827%	0.0688		
-0.2	31%	3.155%	0.2326	1.0773	-0.7323
	62%	2.459%	0.1821		
	100%	1.811%	0.1367		
	124%	1.031%	0.0946		
	139%	0.447%	0.0570		
-0.1	62%	2.198%	0.1591	1.0789	-0.7681
	100%	1.978%	0.1444		
	124%	1.774%	0.1411		
	139%	0.735%	0.0657		
0.25	62%	0.393%	0.0381	0.9822	-0.6306
	100%	1.472%	0.1222		
	124%	1.562%	0.1418		
	139%	0.763%	0.0747		

Table 5.4 Variation of loss factor with  $h_{in}/L$ .Figure 5.9 Correlation of  $DP/P$  and  $h_{in}/L$  for different  $a_{2,shroud}$ .

In order to eliminate the dependence on  $a_{2shroud}$ , similarly to the previous parameter, one exponential expression can be used to calculate the loss factor based on  $h_{in}/L$  for every geometry, described by equation (5.5) and shown in Figure 5.10.

$$\frac{DP/P}{(DP/P)_{ref}} = 1.0135 \left[ \frac{h_{in}/L}{(h_{in}/L)_{ref}} \right]^{-0.7655} \quad (5.5)$$

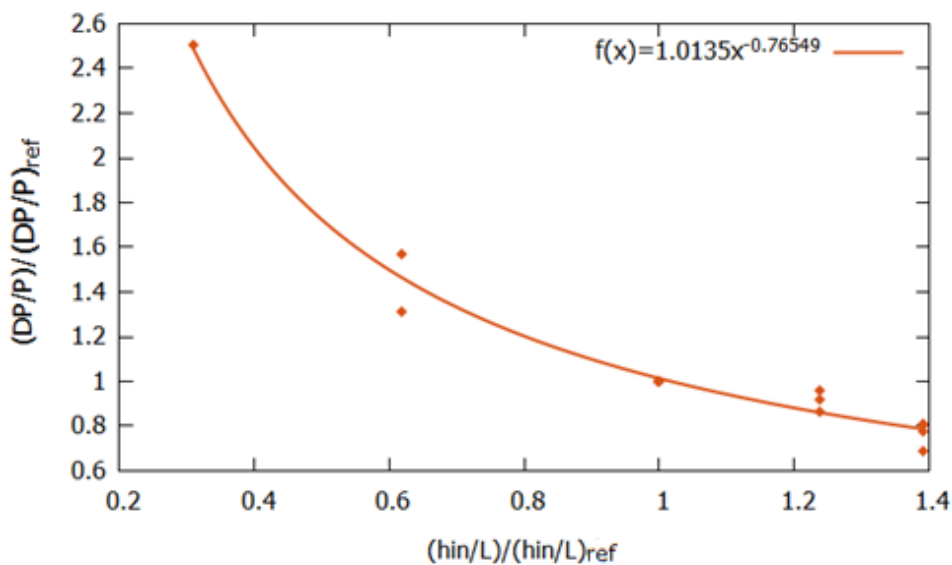


Figure 5.10 Correlation of  $DP/P$  and  $h_{in}/L$ .

#### 5.1.4 Influence of $R_{m_{in}}/L$

An analogous procedure was followed to determine the way that the change of  $R_{m_{in}}/L$  affects the S-duct's pressure losses. More specifically, as in the case of  $h_{in}/L$ , for the different values of the parameter the inlet area of the duct is influenced. To maintain the Mach number at the inlet unchanged the mass flow rate should be adjusted. For higher values the mass flow is also increased, assuming that the density at the inlet is remaining the same. The flow developed inside the intercompressor duct for  $a_{2shroud} = -0.2$  and varying  $R_{m_{in}}/L$  is demonstrated in Figure 5.11.

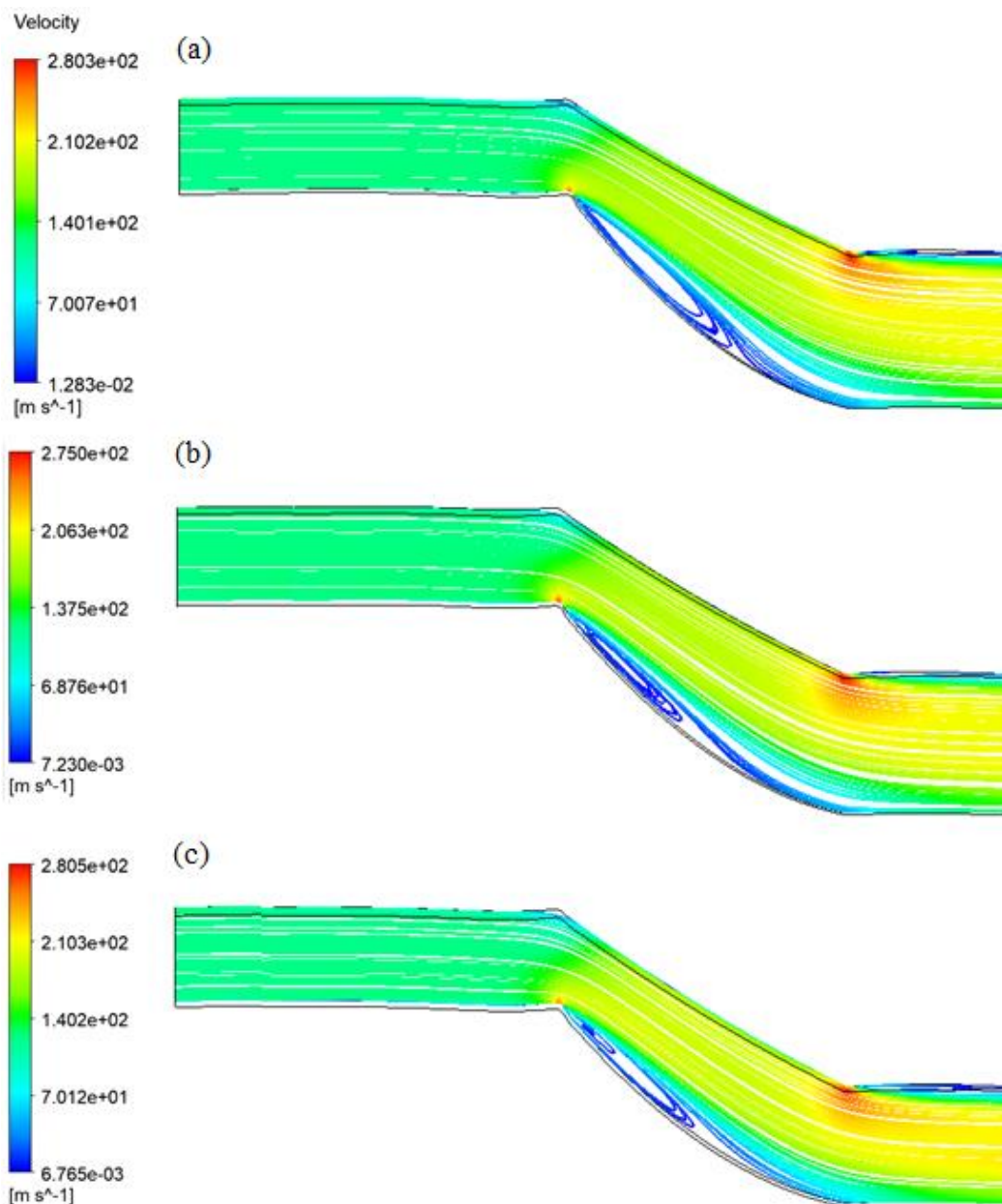


Figure 5.11 Streamlines for ducts with (a)88%, (b)100%, (c)125% of  $(R_{min}/L)_{ref}$ .

The pressure loss factors estimated by the simulation for the different geometries and values of the parameter under examination are included in Table 5.5. In most of the cases the increase in  $R_{min}/L$  leads to a small rise of the losses. However, this pattern is not clear as the changes are not considered significant. The influence of this design parameter can be represented by a second order polynomial function given by (5.6). The accuracy of this description is satisfactory as proved by the least squares fitting algorithm.



$$\frac{DP/P}{(DP/P)_{ref}} = d_2 \left[ \frac{R_{min}/L}{(R_{min}/L)_{ref}} \right]^2 + d_1 \left[ \frac{R_{min}/L}{(R_{min}/L)_{ref}} \right] + d_0 \quad (5.6)$$

$a_{2shroud}$	$\frac{R_{min}/L}{(R_{min}/L)_{ref}}$	$DP/P$	$\omega$	$d_2$	$d_1$	$d_0$
-0.4	88%	2.059%	0.1492	-2.1231	5.0691	-1.8773
	100%	2.144%	0.1489			
	110%	2.556%	0.1748			
	125%	2.416%	0.1611			
-0.2	81%	1.759%	0.1469	2.0982	-3.8479	2.6990
	88%	1.636%	0.1256			
	100%	1.811%	0.1367			
	110%	1.758%	0.1283			
	125%	2.127%	0.1563			
-0.1	88%	1.913%	0.1617	3.4048	-7.4235	4.9847
	100%	1.774%	0.1411			
	110%	1.610%	0.1222			
	125%	1.832%	0.1371			
0.25	88%	1.501%	0.1395	-2.8908	6.4076	-2.4571
	100%	1.562%	0.1418			
	110%	1.792%	0.1606			
	125%	1.597%	0.1387			

Table 5.5 Variation of loss factor with  $R_{min}/L$ .

The function (5.7), with the suitable coefficients  $d_2, d_1, d_0$ , is also found to describe accurately the correlation of  $DP/P$  and  $R_{min}/L$ , independently of  $a_{2shroud}$ . The least squares curve fitting process indicated that the equation can be used for this purpose.

$$\frac{DP/P}{(DP/P)_{ref}} = 1.0442 \left[ \frac{R_{min}/L}{(R_{min}/L)_{ref}} \right]^2 + 1.8874 \left[ \frac{R_{min}/L}{(R_{min}/L)_{ref}} \right] + 1.8099 \quad (5.7)$$

In Figure 5.12 the fitted curves for each geometry are shown while in Figure 5.13 the single curve describing all of them is presented. A single curve could be used also here since the connection of  $d_2, d_1, d_0$  to  $a_{2shroud}$  is not evident.

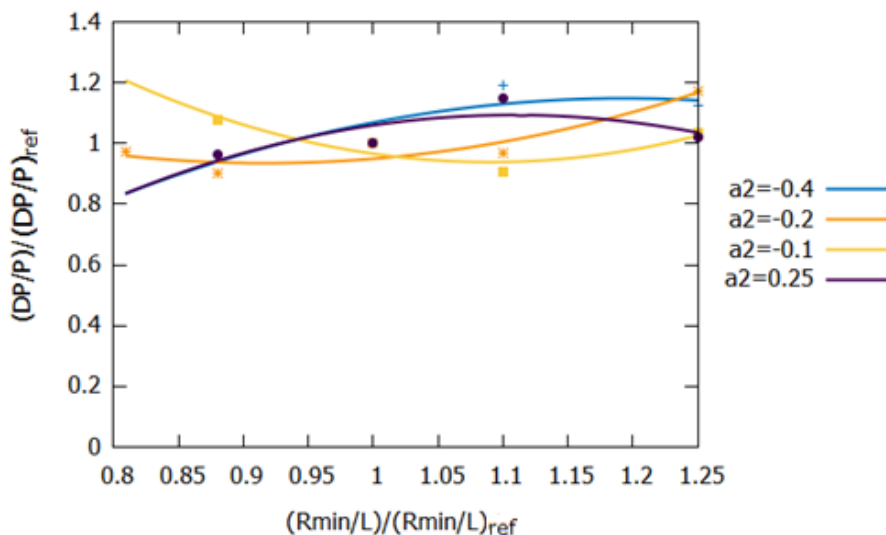


Figure 5.12 Correlation of  $DP/P$  and  $R_{min}/L$  for different  $a_{2shroud}$ .

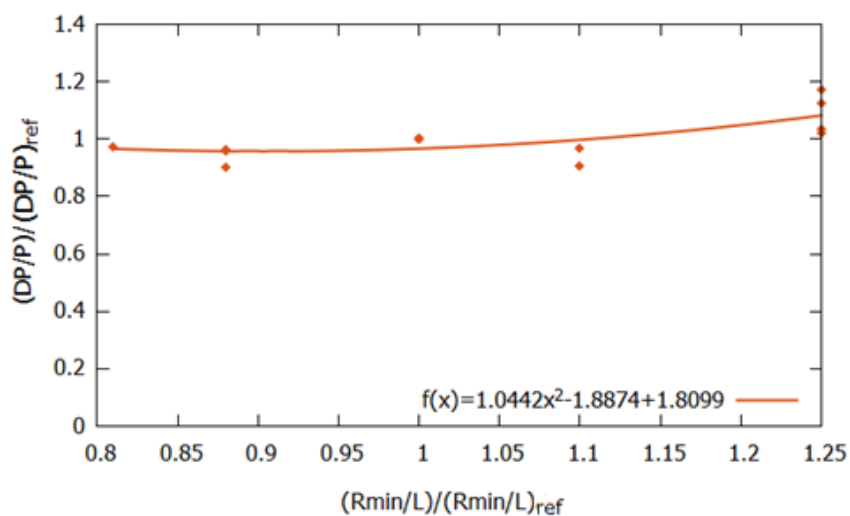


Figure 5.13 Correlation of  $DP/P$  and  $R_{min}/L$ .

### 5.1.5 Off-Design Mass Flow Rate

For the mathematical modelling of the intercompressor S-duct another crucial parameter is the inlet mass flow rate. The correlations found and the results presented in the above paragraphs correspond to the design point of the ducts. However, it is expected that for the off-design operating points, for which the mass flow rate is lower, the pressure losses will be affected. More specifically, as the mass flow rate is decreasing the pressure loss coefficient is also reduced, as shown in Table 5.6.

As it is suggested in [47], an exponential function like (5.8) could be used to describe the connection between the two values, with the exponent equal to 2, which corresponds to the case of a cylindrical duct.

$$\frac{DP/P}{(DP/P)_{des}} = \left[ \frac{\dot{m}}{\dot{m}_{des}} \right]^{\text{exponent}} \quad (5.8)$$

From the CFD simulation, conducted for the different ducts, it is observed that the exponent is closely related to the geometry of the duct, thus to  $a_{2shroud}$ . For every case the non-linear least squares algorithm is used to determine the exponent.

$a_{2shroud}$	$\dot{m}/\dot{m}_{des}$	$DP/P$	$\omega$
-0.63	100.0%	2.923%	0.1858
	75.0%	1.013%	0.1212
	50.0%	0.386%	0.1085
	37.5%	0.213%	0.1081
	25.0%	0.098%	0.1127
	10.0%	0.019%	0.1423
-0.4	100.0%	2.144%	0.1489
	75.0%	0.867%	0.1134
	50.0%	0.340%	0.1042
	37.5%	0.189%	0.1046
	25.0%	0.086%	0.1086
	10.0%	0.016%	0.1294
-0.2	100.0%	1.811%	0.1367
	75.0%	0.794%	0.1123
	50.0%	0.321%	0.1061
	37.5%	0.179%	0.1070
	25.0%	0.082%	0.1113
	10.0%	0.015%	0.1310
-0.1	100.0%	1.774%	0.1411
	75.0%	0.799%	0.1189
	50.0%	0.324%	0.1124
	37.5%	0.183%	0.1147
	25.0%	0.086%	0.1231
	10.0%	0.015%	0.1368
0.25	100.0%	1.562%	0.1418
	75.0%	0.790%	0.1344
	50.0%	0.317%	0.1250
	37.5%	0.181%	0.1283
	25.0%	0.082%	0.1313
	10.0%	0.014%	0.1370
0.5	100.0%	1.519%	0.1452
	75.0%	0.675%	0.1201
	50.0%	0.272%	0.1127
	37.5%	0.153%	0.1141
	25.0%	0.069%	0.1170
	10.0%	0.012%	0.1281

Table 5.6 Variation of loss factor with mass flow rate.

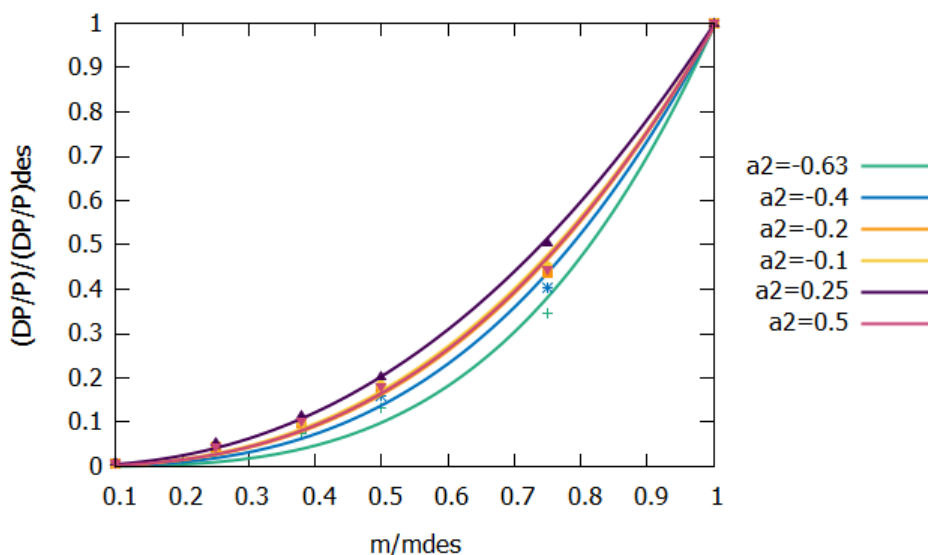


Figure 5.14 Correlation of  $DP/P$  and  $\dot{m}$  for different  $a_{2shroud}$ .

In Figure 5.15 the curve generated by the calculated exponent is compared to the one derived when the exponent is set to 2, for  $a_{2shroud} = -0.2$ , with the maximum difference between them being 10% for  $\dot{m}/\dot{m}_{des}=0.65$ . As it is visible the first curve fits better to the CFD results. Similar comparisons can be made for all the geometries.

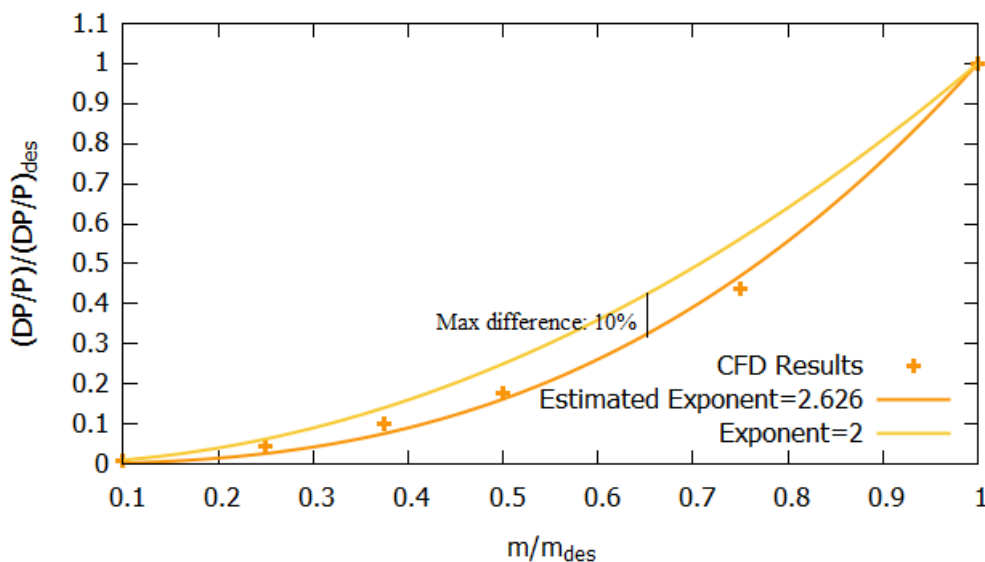


Figure 5.15 Comparison of generated curve to the commonly used one for  $a_{2shroud} = -0.2$ .

In Figure 5.16, both the exponents calculated for the geometries examined and the best fitting curve are presented. The equation (5.9) describes the existent correlation between the exponent of (5.8) and the  $a_{2shroud}$  with satisfactory accuracy.

$$exponent = 1.4822a_{2shroud}^2 - 0.5068a_{2shroud} + 2.4212 \quad (5.9)$$

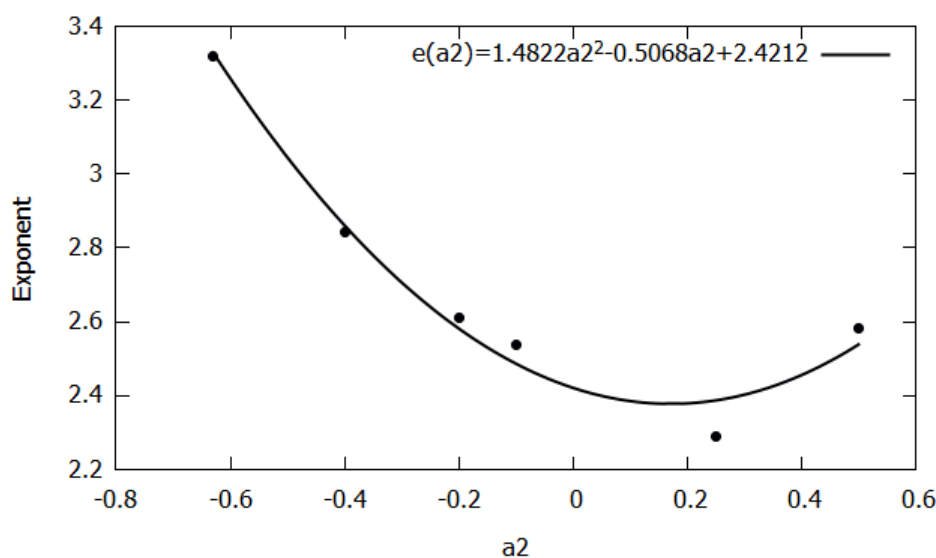


Figure 5.16 Variation of Exponent with  $a_{2shroud}$ .

## 5.2 Development of Algebraic Model

For the estimation of the pressure loss factor  $DP/P$  for a certain duct geometry all the analyzed parameters should be considered. The correlations found between the variables used for the parametrization and the losses can be used to develop an algebraic model, which is schematically presented in Figure 5.17.

Firstly, based on the  $a_{2shroud}$  of the S-duct the factor corresponding to the reference values of the parameters can be calculated via equation (5.1). The next step is to determine the parameters needed as a fraction of the reference ones, which for this work are given in Table 5.1. The expressions produced in Section 5.1 are now implemented to connect  $DP/P$  to each one of the user's inputs. More specifically, equations (5.3), (5.5), (5.7) are used for the calculation of the loss factor based on the values of  $\Delta R/L$ ,  $h_{in}/L$  and  $R_{min}/L$ , respectively. These can be either given directly by the user, from *Parameterization Process I*, or derived from  $R_{hub}/R_{shroud}$  and the Mach number, at the inlet and the outlet, if *Process II* is implemented. Through this procedure the design point pressure losses for the generated duct geometry are computed.

In addition, the design mass flow rate as well as its value at the examined operating point should be given as inputs, for both the available Parameterization Processes. Based on the  $a_{2shroud}$  the exponent of the function relating the loss factor with the mass flow can be found, by equation (5.8). Finally, (5.9) yields the value of  $DP/P$  for the intercompressor duct examined at the specified operating point.

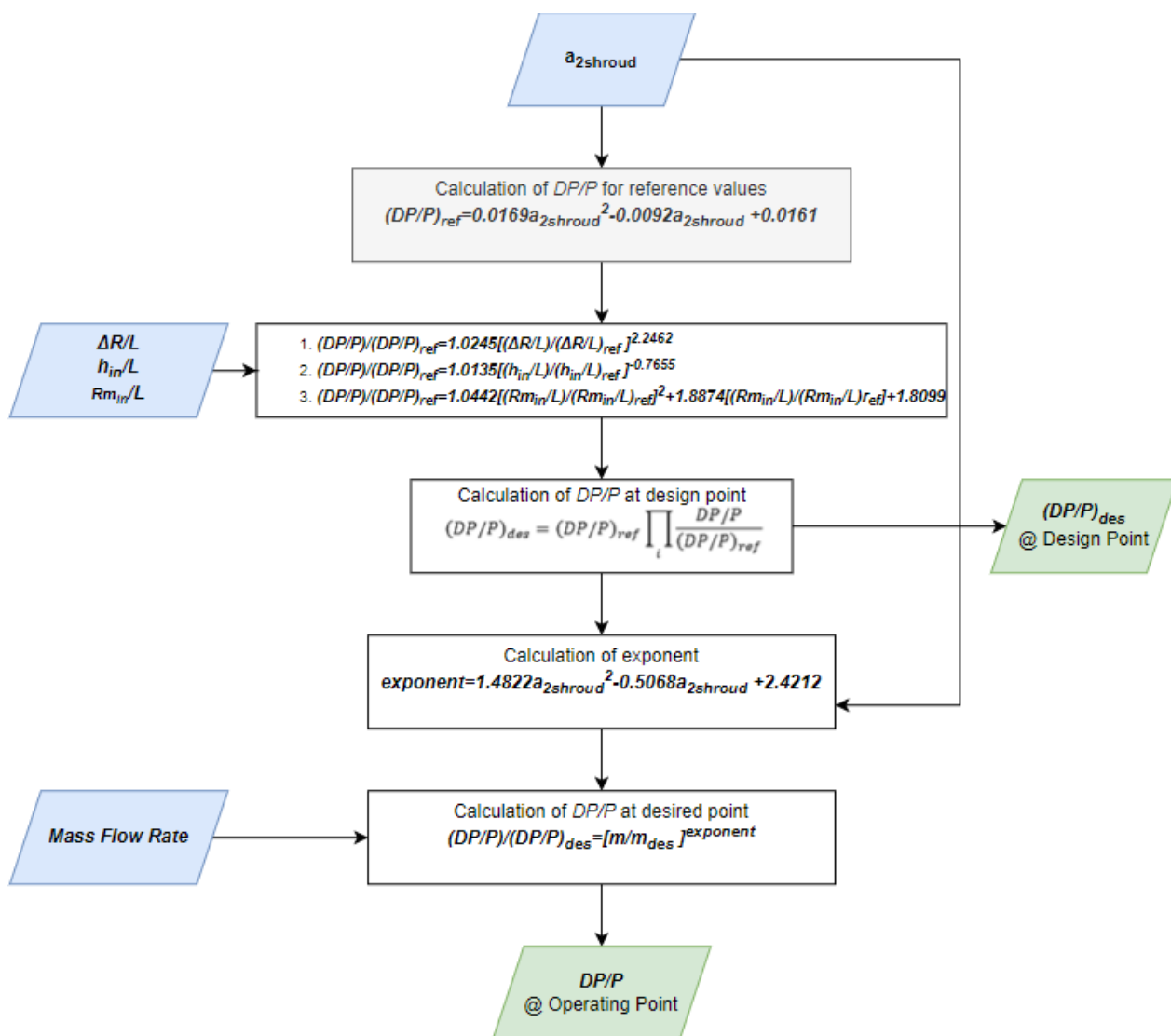


Figure 5.17 Schematic representation of the developed model.

### 5.3 Validation of Model

In order to assure that the estimations provided by the model developed are accurate, a validation process is required. Four cases of ducts were examined, with different geometry and mass flow rates at the design point. The geometry for each one was generated by the *Parametrization Process II*, presented in Section 3.3. This procedure was selected because it ensures that the Mach numbers are maintained at the desired, typical values given in Figure 2.7, even when the mass flow rate is varied. The parameters defined for each case are shown in Table 5.7, while the boundary conditions are the ones discussed in Section 4.4.2. The values chosen for  $R_{hub}/R_{shroud}$  at the inlet and outlet of the duct are the mean values found from the digitization process, while the length is equal to the length of the base case duct.

Case	$\alpha_{2_{shroud}}$	$\left(\frac{R_{hub}}{R_{shroud}}\right)_{in}$	$\left(\frac{R_{hub}}{R_{shroud}}\right)_{out}$	$L$ (m)	$\dot{m}_{des}$ $\left(\frac{kg}{s}\right)$	$Mach_{in}$	$Mach_{out}$
1	-0.4	0.8	0.64	0.50882	100	0.3618	0.5039
2	0.1	0.8	0.64	0.50882	100	0.3618	0.5039
3	-0.2	0.8	0.64	0.50882	50	0.3618	0.5039
4	-0.2	0.8	0.64	0.50882	25	0.3618	0.5039

Table 5.7 Cases examined for the validation of the model.

Firstly, the losses for each duct were calculated by conducting a CFX simulation for the design and some off-design operating points. The second step was the computation of the pressure loss factor using the model described for the same conditions. Finally, the values calculated as well as the exponent, used for the derivation of losses at the off-design points, were compared.

### 5.3.1 Case 1

For the first case, the process is explained analytically. In Table 5.8 the values of the parameters affecting the losses as well as the ratio of them to their reference values, are shown.

Parameter	Case 1	Ratio
$\Delta R/L$	0.5280	0.8023
$h_{in}/L$	0.3126	0.9670
$R_{min}/L$	1.4066	1.0321

Table 5.8 Input Parameters for Case 1.

The pressure loss factor for the reference values and the exponent used to estimate the losses for varying mass flow rates, are presented in Table 5.9. Both values were calculated directly from  $\alpha_{2_{shroud}}$  via the equations discussed in the previous paragraphs.

$(DP/P)_{ref}$	2.246%
<b>exponent</b>	2.86107

Table 5.9 Reference Pressure losses and exponent of Case 1.

The  $DP/P$  at the design point, for the examined duct, can be easily calculated by the value corresponding to the reference parameters and the model's equations found to connect it to the ratios of Table. Its value for the design mass flow rate is also derived from the results of the CFD simulation. The difference between the two factors, shown in Table 5.10, does not exceed 2%. This small deviation confirms the model's accuracy.

	Estimated Value	CFD Value	Deviation (%)
$(DP/P)_{des}$	1.421%	1.398%	1.69%

Table 5.10 Comparison of  $DP/P$  at design point for Case 1.

In order to ensure that the method used to estimate the losses for the lower mass flow rates, CFD simulations were conducted, with the results contained in Table 5.11.

Mass Flow (%)	Estimated Value	CFD Value
80%	0.751%	0.692%
60%	0.330%	0.330%
40%	0.103%	0.143%
20%	0.014%	0.041%
10%	0.002%	0.013%

Table 5.11 Comparison of  $DP/P$  at off-design points for Case 1.

It is evident that the model is more accurate for the mass flow rates closer to the design point, where the losses are also more important. The exponent used for the estimation of the off-design pressure losses factor and the one calculated, by the same procedure, from the CFD results, are compared in Table 5.12. As it is seen the difference it is not significant.

	Estimated Value	CFD Value	Deviation (%)
exponent	2.8611	2.9471	2.92%

Table 5.12 Comparison of exponent for Case 1.

Overall, for the first case the model estimates accurately  $\frac{DP}{P}$  at all the operating points of the duct for  $a_{2shroud} = -0.4$ .

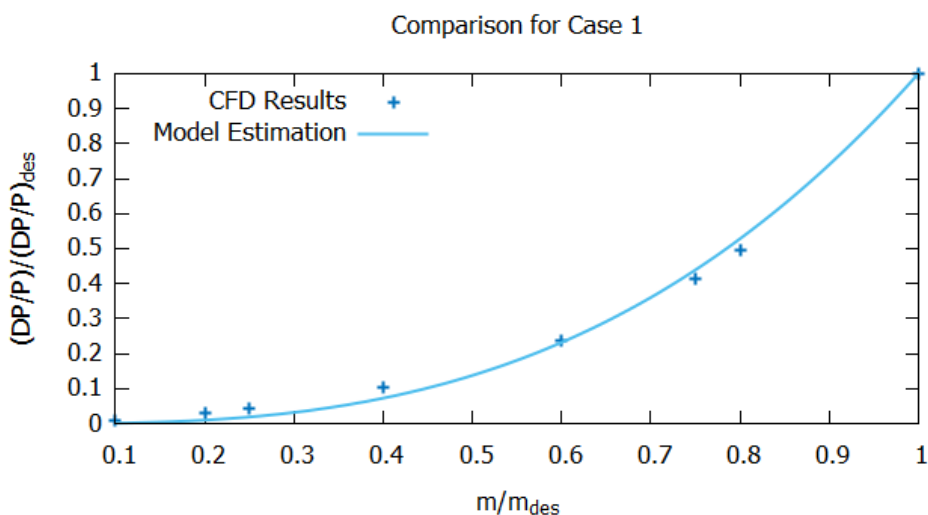


Figure 5.18 Comparison of curves generated by the model and the CFD results for Case 1.

### 5.3.2 Case 2

The same procedure was followed for the second case studied. The new duct geometry is characterized by  $a_{2shroud} = 0.1$  with the mass flow rate at the design point set to  $100 \text{ kg/s}$ . Table 5.13 contains the pressure loss factor and the exponent calculated by the model and the simulation, while in Table 5.14 the results for lower mass flow rates are shown.



	Estimated Value	CFD Value	Deviation (%)
$(DP/P)_{des}$	0.969%	1.043%	7.05%
<i>exponent</i>	2.3853	2.4240	1.59%

Table 5.13 Comparison of  $DP/P$  at design point and exponent for Case 2.

Mass Flow (%)	Estimated Value	CFD Value
80%	0.569%	0.591%
60%	0.287%	0.305%
40%	0.109%	0.133%
20%	0.021%	0.035%
10%	0.004%	0.009%

Table 5.14 Comparison of  $DP/P$  at off-design points for Case 2.

Similar observations are made concerning the accuracy of the estimations. However, the deviation of the factor at the design point is increased, which suggests that probably the model's performance may be affected by  $a_{2shroud}$ .

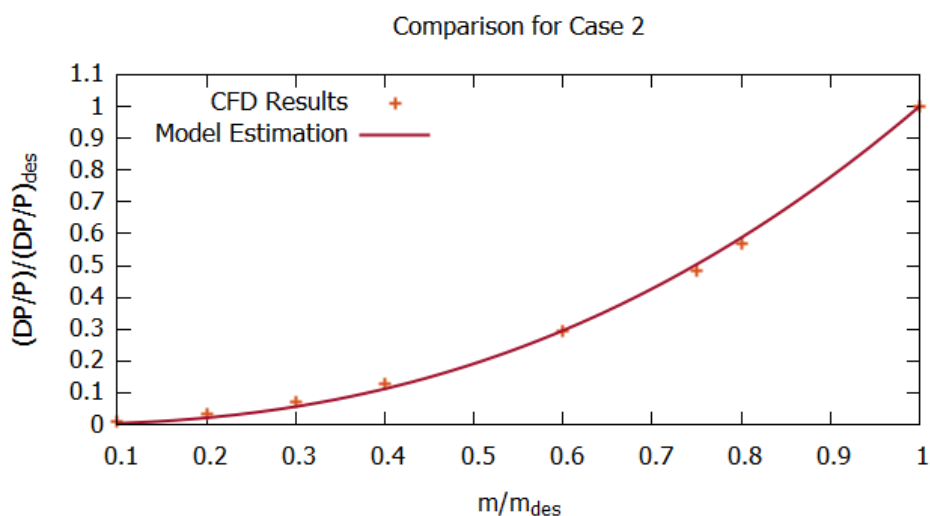


Figure 5.19 Comparison of curves generated by the model and the CFD result for Case 2.

### 5.3.3 Case 3

Another dependence that should be explored is whether the model is affected by the mass flow rate specified for the design point by the user. For this purpose, for the third case its value is set to  $50 \text{ kg/s}$  and the  $a_{2shroud}$  is equal to  $-0.2$ . The Mach numbers at the inlet and the outlet of the duct are kept constant, since they are close to the expected ones for the proper function of the upstream and downstream compressors. As in the previous cases the values of the parameters influencing the pressure losses are calculated and through them the factor  $DP/P$  is found for the design point. In Table 5.15 the losses and the exponent estimated from the model are demonstrated.

	Estimated Value	CFD Value	Deviation (%)
$(DP/P)_{des}$	0.714%	0.703%	1.61 %
<i>exponent</i>	2.5818	2.5114	2.81%

Table 5.15 Comparison of  $DP/P$  at design point and exponent for Case 3.

The CFD simulation was conducted for different operating points, thus different mass flow rates, seen in Table 5.16.

Mass Flow (%)	Estimated Value	CFD Value
75%	0.340%	0.325%
50%	0.119%	0.135%
25%	0.020%	0.035%

Table 5.16 Comparison of  $DP/P$  at off-design points for Case 3.

From the deviations of the results, it can be assumed that the model is suitable for approximating the pressure losses within the S-Duct.

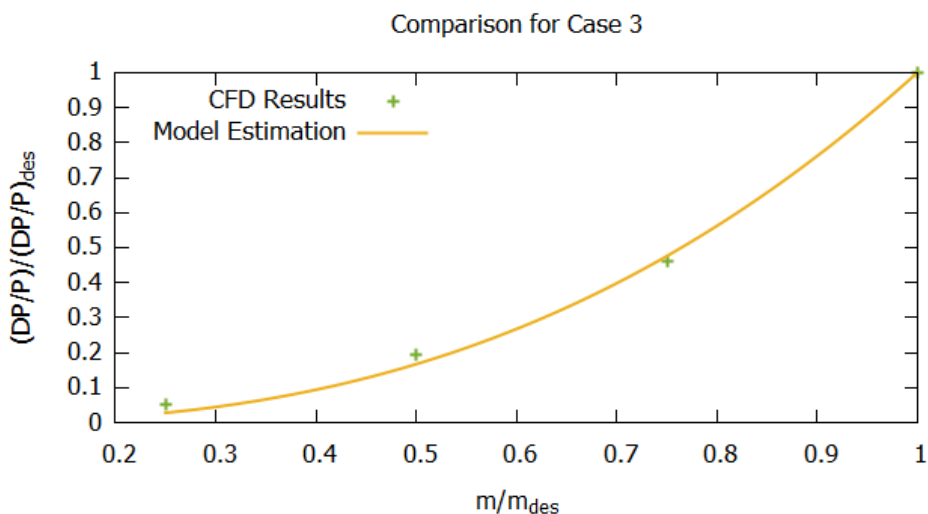


Figure 5.20 Comparison of curves generated by the model and the CFD result for Case 3.

### 5.3.4 Case 4

A lower mass flow rate, for the design point of the duct, was examined in order to check that the model is able to function even with “extreme” inputs. In the fourth case the mass flow is 25 kg/s while all the other parameters are the same as in Case 3.

	Estimated Value	CFD Value	Deviation (%)
$(DP/P)_{des}$	0.482%	0.497%	3.00 %
<i>exponent</i>	2.5818	2.3496	9.88%

Table 5.17 Comparison of  $DP/P$  at design point and exponent for Case 4.

Mass Flow (%)	Estimated Value	CFD Value
75%	0.229%	0.246%
50%	0.080%	0.107%
25%	0.013%	0.028%

Table 5.18 Comparison of  $DP/P$  at off-design points for Case 4.

Although the deviation for the loss factor is maintained low, the difference between the exponents found is almost 10%, which is higher than the other cases, but it does not result in a significant lack in the accuracy of the model.

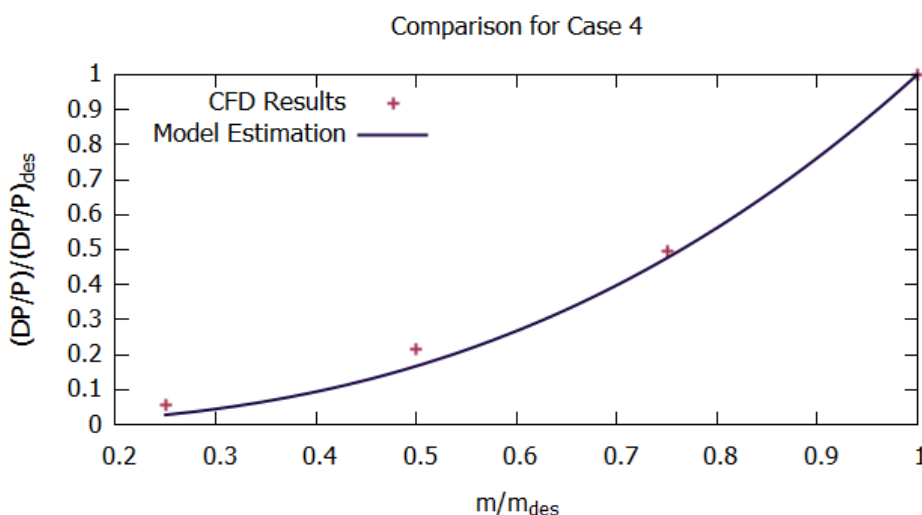


Figure 5.21 Comparison of curves generated by the model and the CFD result for Case 4.

## 5.4 Parametric study based on the model's results

After the model's validation it is important to examine how the estimated loss factor is influenced by the inputs of *Parametrization Process II*. As it was mentioned in Chapter 2, one of the constraints that is imposed to the designer of the intermediate compressor duct, is its weight. Each one of the variables selected as inputs result to a different S-duct and thus, to different weight and losses. In the paragraphs below the connection between these values is discussed and the existence of "optimal" input values is examined.

For the calculation of the weight, it is assumed that the duct's material is Steel,  $\rho = 8000 \text{ kg/m}^3$ , and that the thickness of the walls is  $t = 2 \text{ mm}$ . It should be mentioned that even though the material chosen serves the purpose of this study since the duct is not subjected to high stresses, aluminum, titanium and composites can also be used. For every set of values for  $a_{2_{shroud}}$ ,  $L$ ,  $(R_{hub}/R_{shroud})_{in}$ ,  $(R_{hub}/R_{shroud})_{out}$ ,  $M_{in}$ ,  $M_{out}$ ,  $\dot{m}$ , the geometry is derived from *Process II*, described in Section 3.3, and the weight is estimated by numerical integration, as shown in (5.10).

$$W = \rho t \sum_{i=2}^{N+1} 2\pi \left[ \frac{R_{hub_{i-1}} + R_{hub_i}}{2} + \frac{(R_{shroud_{i-1}} + R_{shroud_i})}{2} \right] (x_{i-1} + x_i) \quad (5.10)$$

### 5.4.1 Variation of $a_{2_{shroud}}$

For different values of  $a_{2_{shroud}}$  the geometry generated is also varying and thus the weight calculated is changed. By using the model developed the loss factor  $DP/P$  is estimated. In Figure 5.22, by plotting the losses versus the weight, a frontier is created, which can also be referred to as Pareto Front. The Pareto Front represents the compromise that needs to be made while designing the intercompressor ducts for turbofan engines. In order to achieve the minimum weight the losses are increased. As it is seen this frontier is moving to lower values of losses and weight as the design point mass flow rate is reduced.

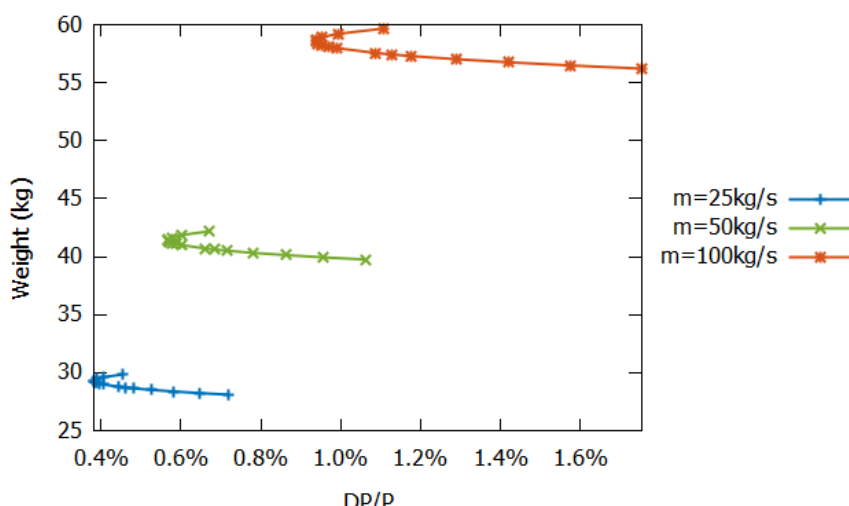


Figure 5.22 Diagram for variation of  $a_{2_{shroud}}$  and different  $\dot{m}$ .

If the axes are non-dimensional the Pareto front coincides for the different mass flow rates, as in Figure 5.23. For the x axis the total pressure loss factor is expressed as the percentage of its minimum values, calculated for the examined range of  $a_{2_{shroud}}$ , while for the y axis the weight is divided by the weight corresponding to the  $(DP/P)_{min}$ . Thus, the point (1,1) corresponds to the optimal  $a_{2_{shroud}}$  which is equal to 0.25.

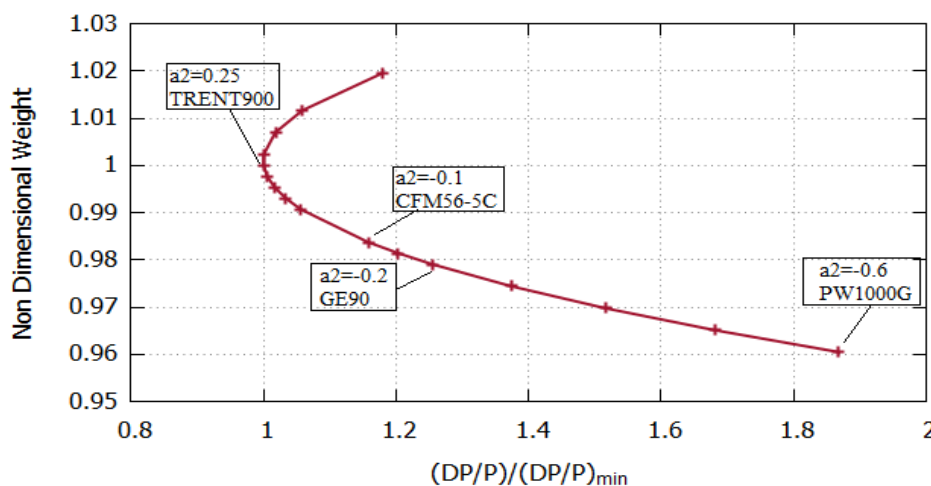


Figure 5.23 Non-Dimensional diagram for variation of  $a_{2shroud}$ .

Another observation made from Figure 5.23 is that for a duct 4% lighter than the optimal the loss factor is increased by 87%. Nonetheless, by recognizing on the Pareto front the points corresponding to some of the digitized, high bypass ratio engines, it is suggested that it is preferred to design lighter ducts.

The conclusions reached for the selection of  $a_{2shroud}$  are not necessarily corresponding to the real design compromises made, since for the definition of the optimal geometry other parameters, such as the presence of struts and the constraints imposed by the upstream and downstream components, should be considered. In order to find the real optimal geometry, all the above should be taken into account developing a more integrated approach.

## 5.4.2 Variation of Length

As it was demonstrated in Section 5.1.2, the length of the duct is significantly affecting the flow patterns developed and the total pressure losses. As the duct is elongated the losses are reduced but the overall weight is increased as shown in Figure 5.24. Thus, a Pareto front is created to describe the “trade-off” between the two parameters. It is suggested that after a certain length the weight is expected to rise without any significant benefit on the loss factor.

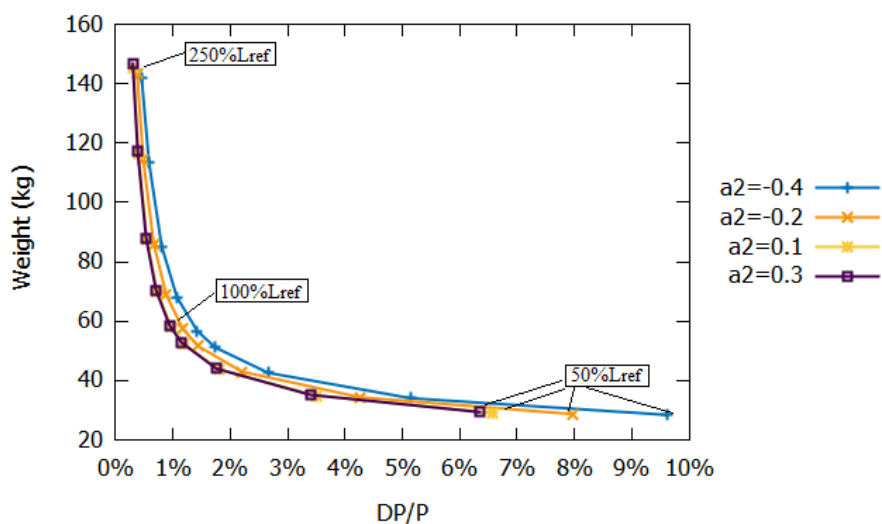


Figure 5.24 Diagram for variation of length and  $\dot{m} = 100\text{kg/s}$ .

For different mass flow rates, plotted in non-dimensional axes, the frontier presents a slight change. The lower the mass flow rate at the design point, the lower the total pressure loss factor for the same weight. This observation is justified since the duct's geometries produced by the *Parametrization Process II* are directly affected by the mass flow rate, as in Figure 5.26.

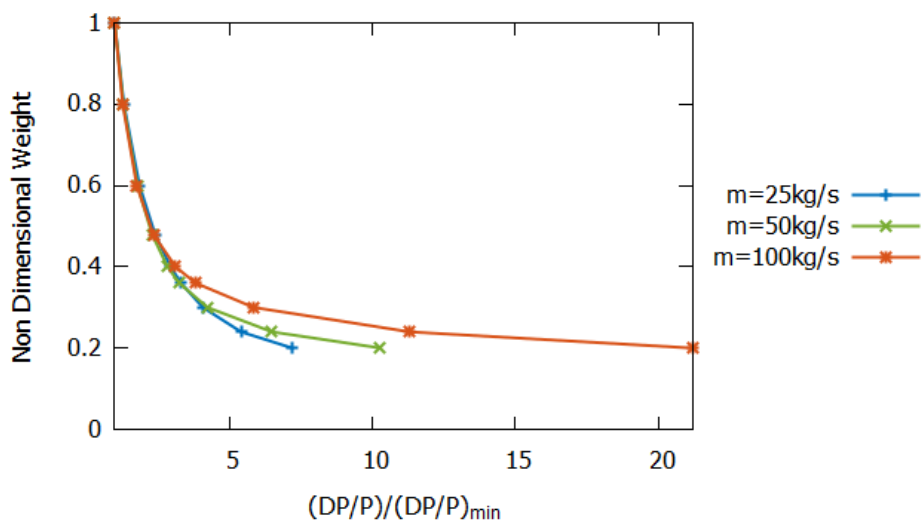


Figure 5.25 Diagram for variation of length, different  $\dot{m}$  and  $a_{2\text{shroud}} = 0.3$ .

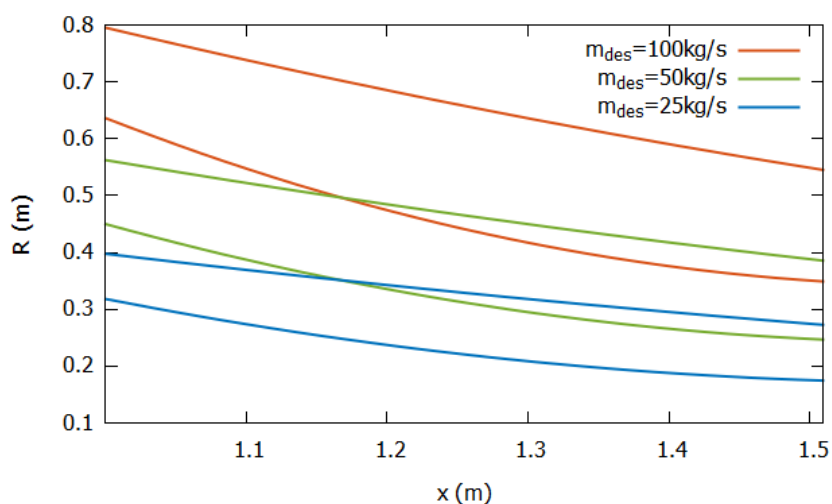


Figure 5.26 Duct's Shapes for  $100\%L_{ref}$  and different mass flow rates.

### 5.4.3 Variation of $R_{hub}/R_{shroud}$

Both in the inlet and the outlet of the duct the ratio  $R_{hub}/R_{shroud}$  is constrained by the design of the HPC and LPC, respectively. The range within the variation of the parameter is maintained is the one provided by the analysis of the digitized engines, given in Table 3.2.

At the inlet of the duct the values assigned to  $(R_{hub}/R_{shroud})_{in}$  are within 0.72 – 0.88. For these geometries the processes, explained in the paragraphs above, are followed for the estimation of the weight and the total pressure loss factor. As the value of  $(R_{hub}/R_{shroud})_{in}$  is changed the geometric parameters are affected, and the geometry is varied as in Figure 5.27. More specifically a rise in  $(R_{hub}/R_{shroud})_{in}$  results to a significant increase in  $\Delta R/L$ ,  $R_{min}/L$  and a decrease in  $h_{in}/L$ , and thus to a sharp increase in the pressure loss factor.

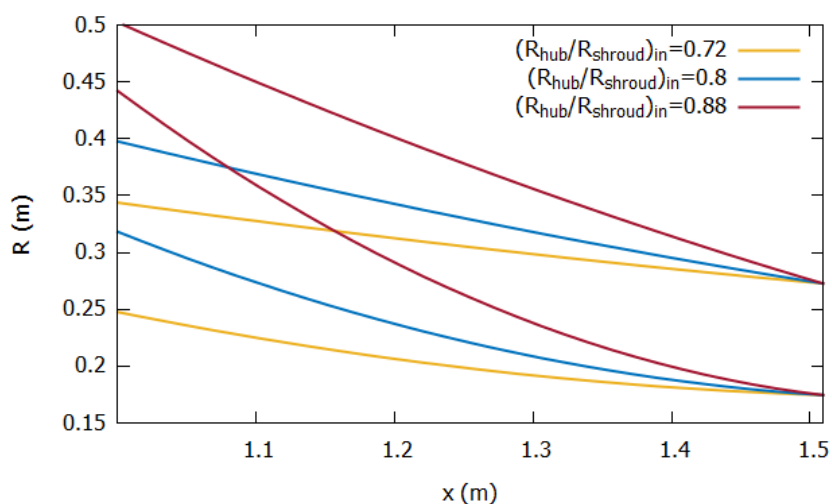


Figure 5.27 Different geometries produced for varying  $(R_{hub}/R_{shroud})_{in}$ .

In Figure 5.28, it is evident that the minimum weight and losses can be achieved for the lower values of the parameter, for every  $a_{2shroud}$ . The curves generated for different mass flow rates and  $a_{2shroud} = 0.3$  are shown in Figure 5.29.

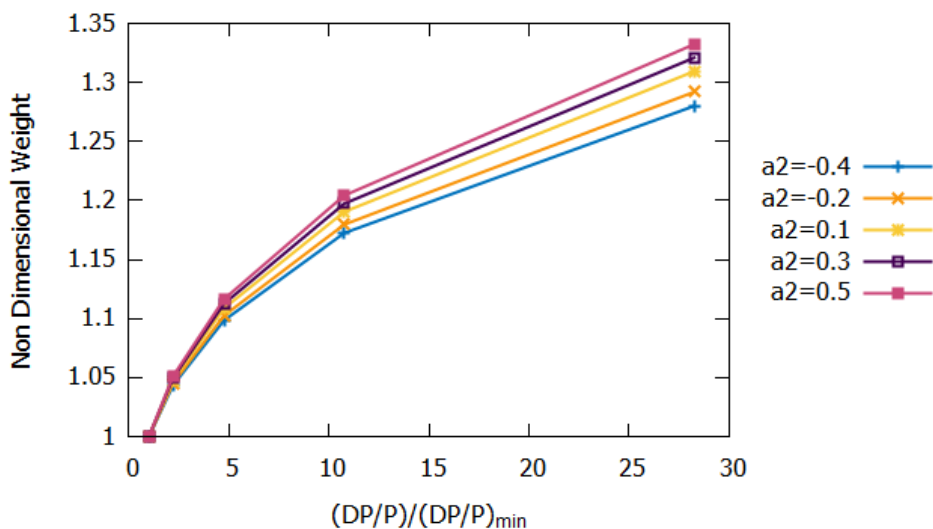


Figure 5.28 Diagram for variation  $(R_{hub}/R_{shroud})_{in}$  and  $\dot{m} = 100\text{kg/s}$ .

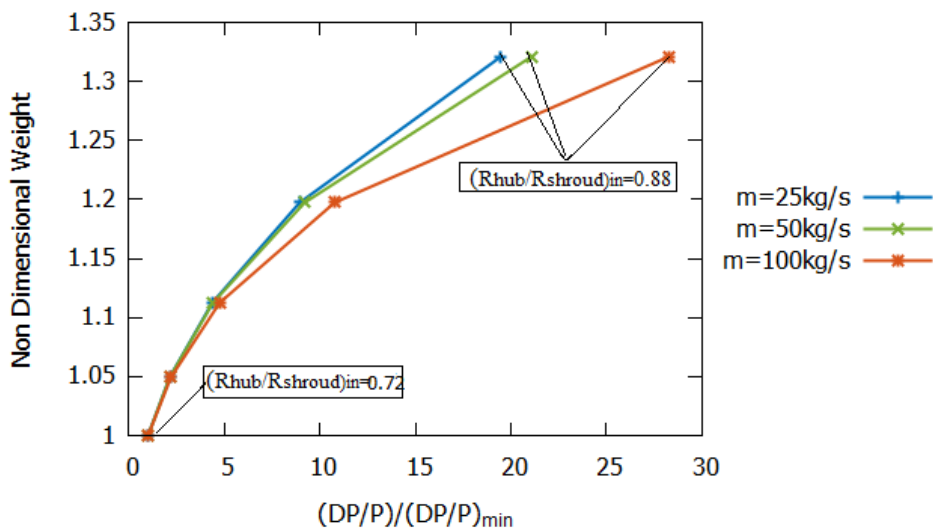


Figure 5.29 Diagram for variation  $(R_{hub}/R_{shroud})_{in}$ , different  $\dot{m}$  and  $a_{2shroud} = 0.3$ .

At the outlet,  $(R_{hub}/R_{shroud})_{out}$  is varying between 0.48 – 0.77. As the parameter is increased  $\Delta R/L$  is reduced, as seen in Figure 5.30. In this case, the heavier duct corresponds to the minimum losses, and to the upper limit of the range. As seen in Figure 5.31, the weight is increased for higher values of  $a_{2shroud}$ . For different mass flow rates and a constant  $a_{2shroud}$  the curves produced coincide, as in Figure 5.32.



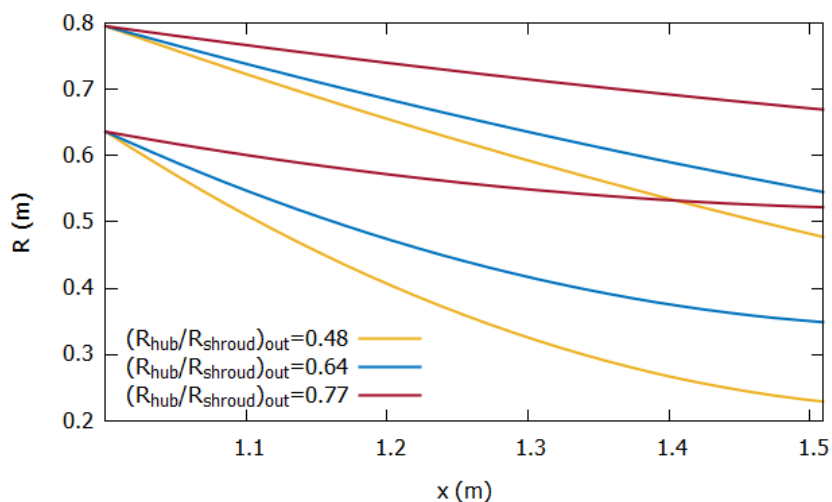


Figure 5.30 Different geometries produced for varying  $(R_{hub}/R_{shroud})_{out}$ .

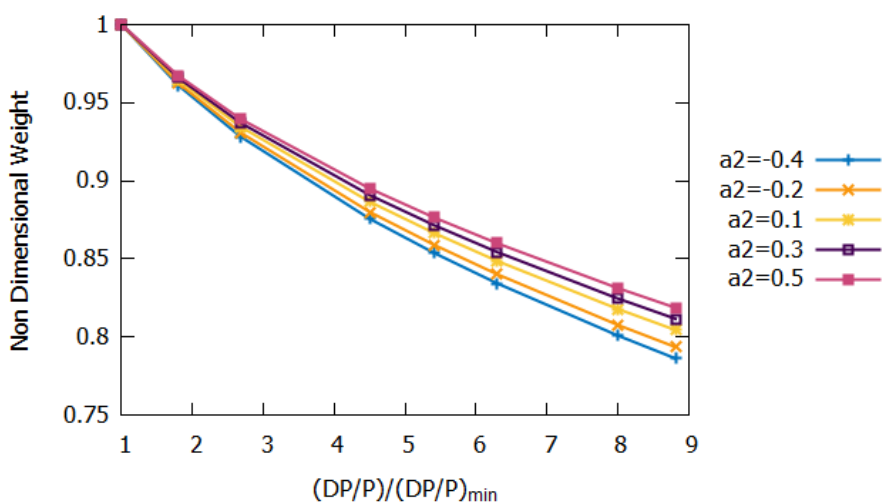


Figure 5.31 Diagram for variation  $(R_{hub}/R_{shroud})_{out}$  and  $\dot{m} = 100\text{kg/s}$ .

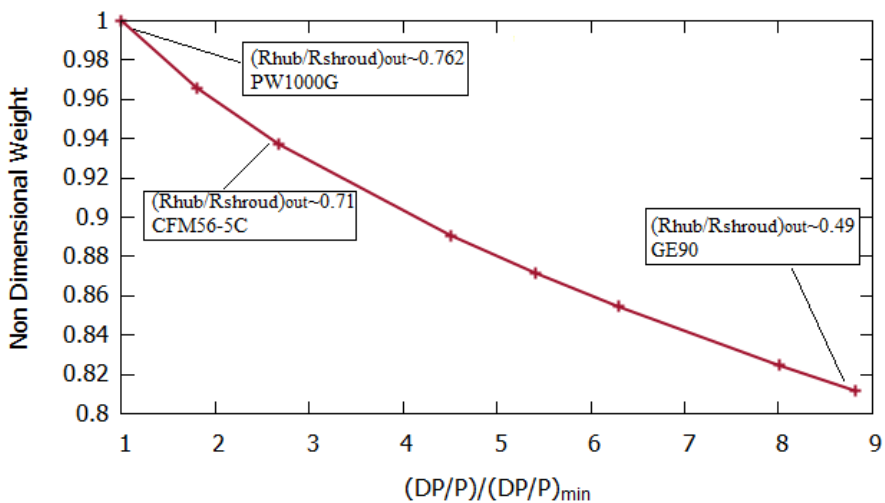


Figure 5.32 Diagram for variation  $(R_{hub}/R_{shroud})_{out}$ , different  $\dot{m}$  and  $a_{2shroud} = 0.3$ .

It should be noted that it is not possible to choose the values of  $R_{hub}/R_{shroud}$  that result in the more efficient duct, for both the inlet and outlet, since they result in a negative value of radial offset. Thus, apart from the constraints imposed by the existence of the compressors, the choice of the parameters should lead to a feasible duct geometry.

#### 5.4.4 Variation of Mach Numbers

In *Parametrization Process II* the Mach numbers, defined at the inlet and outlet, combined with the mass flow rate, are used for the computation of the duct area at the same positions. Thus, their influence on the weight and the losses should be analyzed.

At the inlet of the intercompressor duct, the Mach number is expected to be in the range 0.30 – 0.45. The different geometries generated for varying inlet Mach number are shown in Figure 5.33. From these, both weight and losses are low for  $M_{in} = 0.45$ , for every  $a_{2shroud}$ . When the mass flow rate is decreased, as in Figure 5.35, it is observed that the rise of the loss factor with the increase of weight is lower.

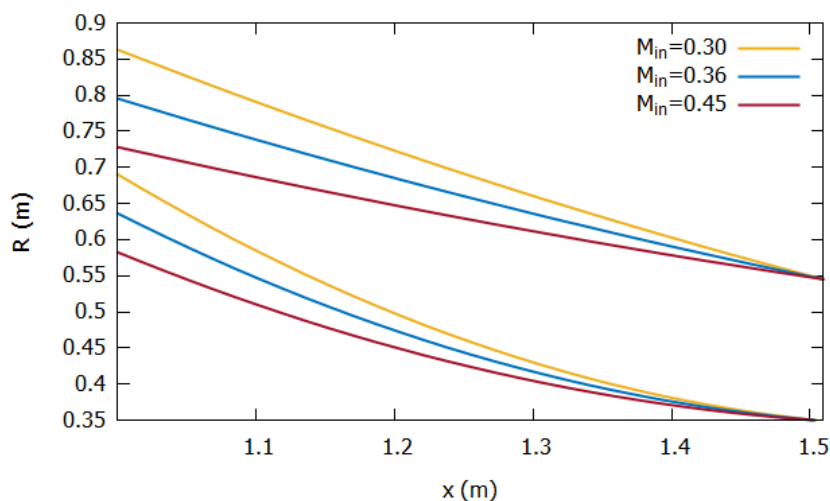


Figure 5.33 Different geometries produced for varying  $M_{in}$ .

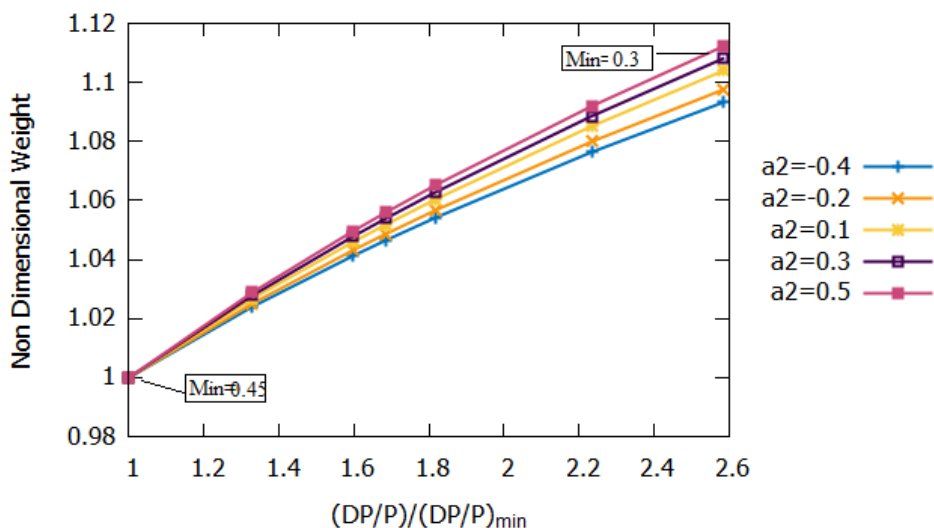


Figure 5.34 Diagram for variation  $M_{in}$  and  $\dot{m} = 100\text{kg/s}$ .

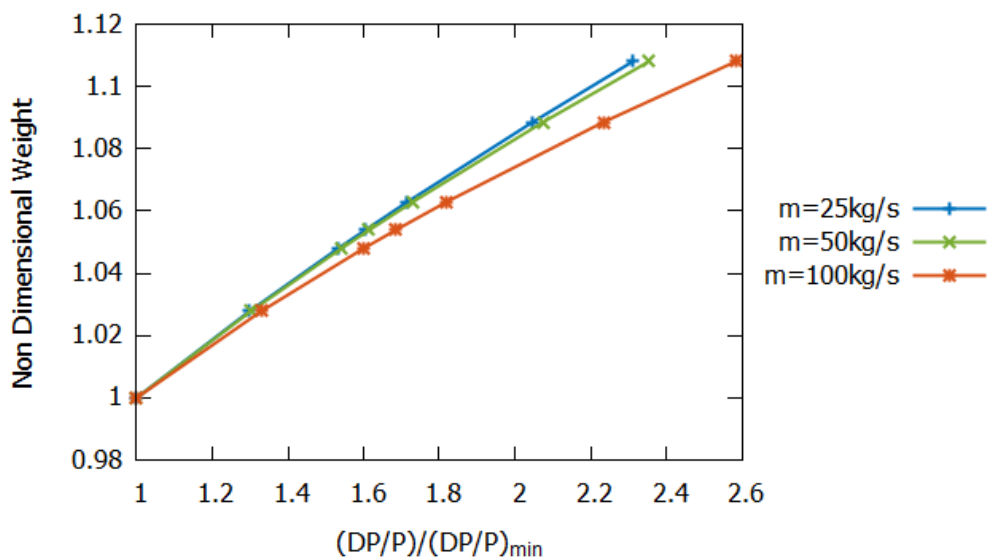


Figure 5.35 Diagram for variation  $M_{in}$ , different  $\dot{m}$  and  $a_{2shroud} = 0.3$ .

For  $M_{out}$  the typical limits, due to the existence of the HPC, are 0.45 – 0.55. An increase to its value results to a rise in  $\Delta R/L$ , and thus higher pressure losses are expected. The best duct performance, in terms of pressure loss, corresponds to  $M_{out} = 0.45$ , as seen in Figure 5.37. The change of the mass flow rate does not lead to any displacement of the curve, in the non-dimensional plot of Figure 5.38.

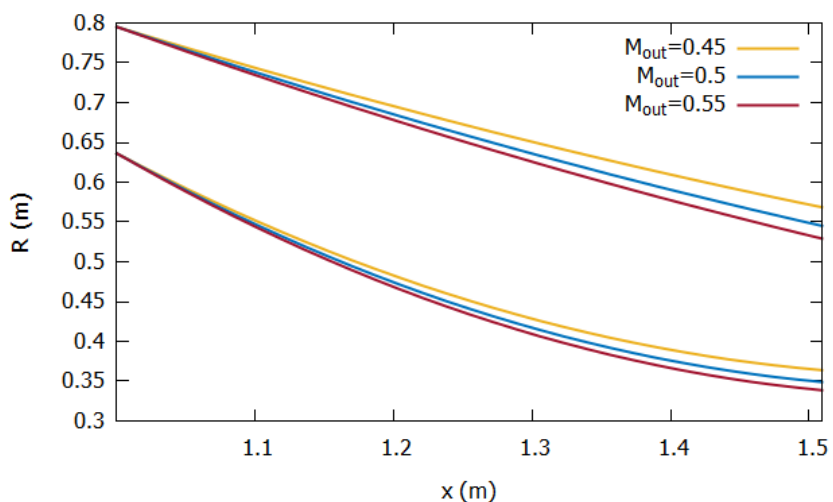


Figure 5.36 Different geometries produced for varying  $M_{out}$ .

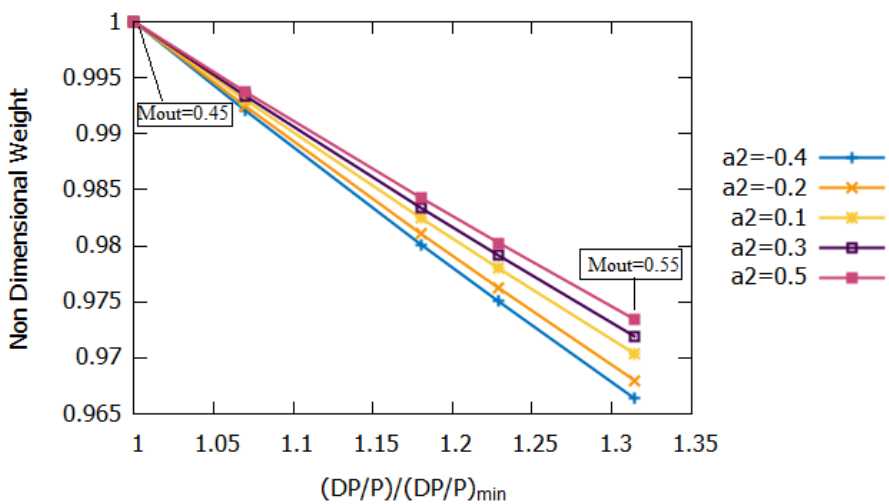


Figure 5.37 Diagram for variation  $M_{out}$  and  $\dot{m} = 100\text{kg/s}$ .

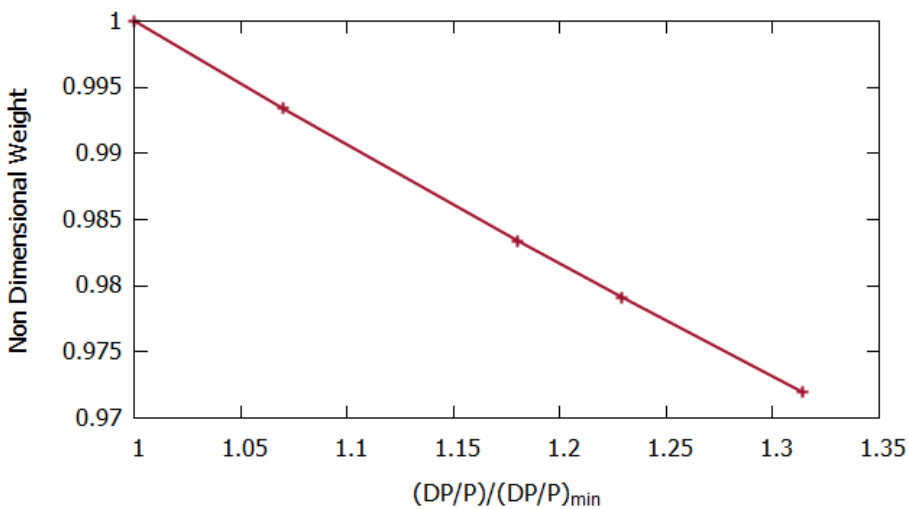


Figure 5.38 Diagram for variation  $M_{out}$  coinciding for different  $\dot{m}$  and  $a_{2shroud} = 0.3$ .

Similar to the previous parameters examined, it is not possible to set both the Mach numbers at their “optimal” values, since this would result in a non-feasible duct geometry. Thus, the values that offer a satisfactory compromise between the pressure losses and the weight, could be defined by investigating the results for combinations of the two parameters.

## Chapter 6 Conclusions and Future Work

### 6.1 Overview

In the present thesis, the development of a model for the estimation of the total pressure loss factor within the intermediate compressor duct based on its geometry is presented. The main parameters describing the shape of this duct were derived for seventeen digitized turbofan engines. In order to define the minimum numbers of variables needed for the accurate description of the duct's geometry, the correlation between them were examined. This way, two different parametrization processes were demonstrated, with their inputs being the basic geometric and design parameters.

The functions connecting the geometry with the pressure losses were determined by analyzing the results of CFD flow simulation, conducted for different geometries and mass flows. The accuracy of these correlations was tested by comparing the results of the model with the results of the CFD calculations, using the second available parametrization process. As a result, the model developed provides an accurate estimation of the total pressure loss factor and it is expected to be more reliable than using an empirical value, with no connection to the actual engine's geometry. However, it is demonstrated that there is a lack of accuracy for the off-design, lower, mass flow rates. The deviations obtained were acceptable, since for low mass flow rates, the pressure losses are significantly reduced, and the absolute difference is not so important.

Finally, a parametric study was conducted, using the estimations of the model, to identify the compromises required to be made between the weight and the performance of the duct during the design process. The values of the inputs  $a_{2shroud}$ ,  $L$ ,  $(R_{hub}/R_{shroud})_{in}$ ,  $(R_{hub}/R_{shroud})_{out}$ ,  $M_{in}$ ,  $M_{out}$  that separately could result in the lower loss factor are discussed. Nonetheless, as it is underlined, the selection of the optimal geometry is challenging, since there are more constraints imposed by the cooperation of the different engine components, which should be considered.

### 6.2 Conclusions

The simulations and the parametric studies conducted for the purpose of this diploma thesis have led to the following conclusions.

From the analysis of the digitized turbofan engines, it is possible to identify the differences between the wall curvatures for their intercompressor ducts. More specifically, the curvature, which in this thesis is described by the parameter  $a_2$ , is not varying significantly for the hub wall, with  $a_{2_{hub}}$  values being all negative and higher than -1. However, for the shroud wall, the  $a_{2_{shroud}}$  fluctuates from -0.63 to 0.67, with the curvature being reversed for the higher, positive values. In addition, a correlation between the parameters describing the hub and shroud curvatures is found. Such a connection is crucial since only one of the two parameters is necessary to recreate the shape of the duct's walls.

The parametric study conducted to derive the functions used in the model revealed the influence of the geometric parameters on the total pressure loss factor. The wall curvature parameter,  $a_{2_{shroud}}$ , significantly affects the losses with the minimum value corresponding to  $a_{2_{shroud}} \approx 0.25$ . Furthermore, an increase in  $\Delta R/L$  results to an increase in the loss factor, while a rise in  $h_{in}/L$  leads to lower losses. For the parameter  $R_{min}/L$  a slight influence on the loss factor is observed and for  $A_{out}/A_{in}$  the dependence is negligible.

In order to complete the model, the pressure loss factor for the off-design mass flows is estimated. In the existing zero-dimensional models the calculation of the factor, based on the losses at the engine's design point, is through an exponential function, with the exponent set to 2. This function provides an accurate estimation for simple, cylindrical ducts. For the annular, S-shaped ducts examined in this diploma thesis, a correlation between the exponent and the wall curvature parameter is derived, with the exponent varying within the range 2.3-3.3. The comparison of the bibliography and the derived exponential functions showed that the latter's results agree with the simulations.

Following the generation of the pressure loss estimation model, the influence of the parameters, commonly available to the designers, on the weight and the pressure losses is determined. This parametric study was conducted separately for each one of the parameters  $a_{2_{shroud}}$ ,  $L$ ,  $(R_{hub}/R_{shroud})_{in}$ ,  $(R_{hub}/R_{shroud})_{out}$ ,  $M_{in}$ ,  $M_{out}$ . For  $a_{2_{shroud}}=0.25$  the minimum pressure loss factor is achieved while the lighter geometry corresponds to the most negative values of the curvature parameter. This conclusion is reached for all the different design mass flow rates examined. The elongation of the duct leads to an increase in its weight but a significant reduce in the losses, as expected. However, after a certain increase in the length the weight is rising rapidly with the pressure loss factor maintained almost constant. As a result, the need for a compromise between the two arises. With a decrease in the design mass flow rate a decrease in the pressure loss factor is noted since the radial offset of the duct is reduced. The value of  $R_{hub}/R_{shroud}$ , for both the inlet and the outlet, significantly affects the radial offset of the duct and thus the total losses. For an increase in  $(R_{hub}/R_{shroud})_{in}$  of approximately 0.15 the losses are grown by 30 times, while the reverse behavior is shown for  $(R_{hub}/R_{shroud})_{out}$ . Finally, the influence of the Mach numbers on the duct's factor is less important. At the inlet, the Mach number should be set to the higher of the values examined to achieve the lower losses and at the outlet to the lower limit of its range.

### 6.3 Future Prospects

Based on the model developed in this work, the following future steps are proposed:

1. In order to increase the accuracy of the model, a higher number of the existing engines could be analyzed, different curve fitting methods could be used and a greater number of validating cases should be examined.
2. A component corresponding to the intermediate compressor S-duct, could be created in PROOSIS, to provide a more accurate estimation of the pressure losses than just assigning an empirical value to the factor. This would require from the user to insert as inputs the ones for either the Parametrization Process I or II and thus, to have basic knowledge of the duct's geometry.
3. Using the component created in PROOSIS, an optimization study for the duct's shape could be conducted.
4. The model should be enriched with the constraints introduced by the existence of the upstream and downstream compressors, for which surge should be avoided, the existence of struts and bleed ducts. This integrated approach could provide more accurate estimations for the performance of the S-duct.
5. The model could be used to conduct a mission analysis for a turbofan engine to recognize the influence of the duct's total pressure loss estimation provided to the performance and the fuel consumption.



## Appendix A: Digitized Turbofans' Engines

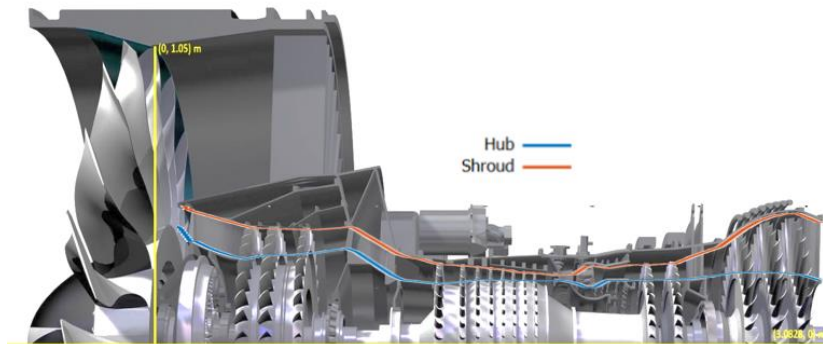


Figure A. 1 Digitized Geometry for PW1000G.

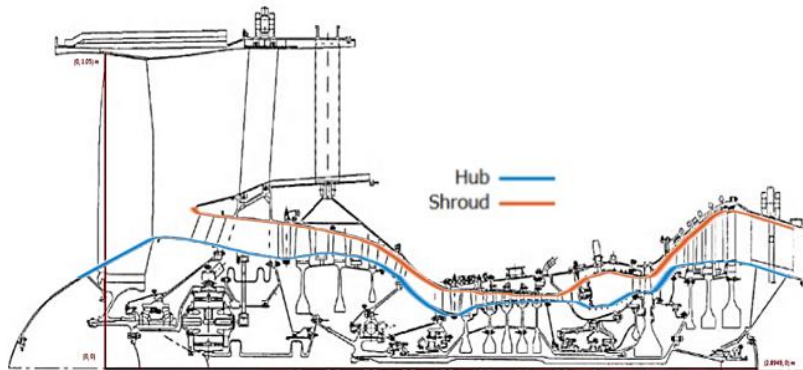


Figure A. 2 Digitized Geometry for the early version of PW1000G.

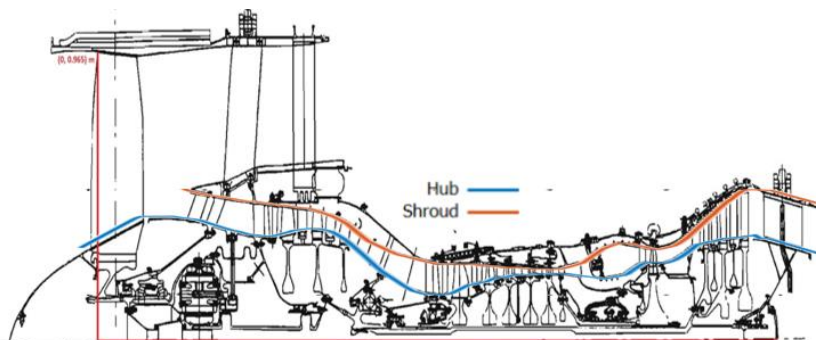


Figure A. 3 Digitized Geometry for PW8000.

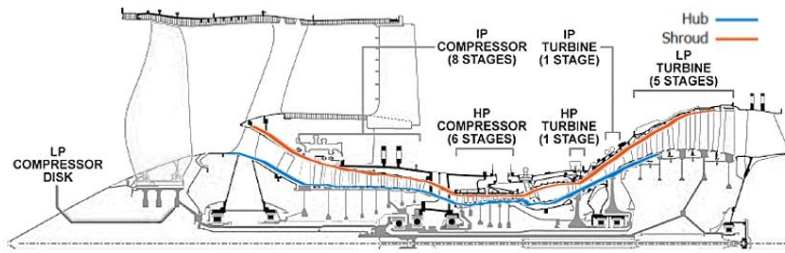


Figure A. 4 Digitized Geometry for TRENT900.

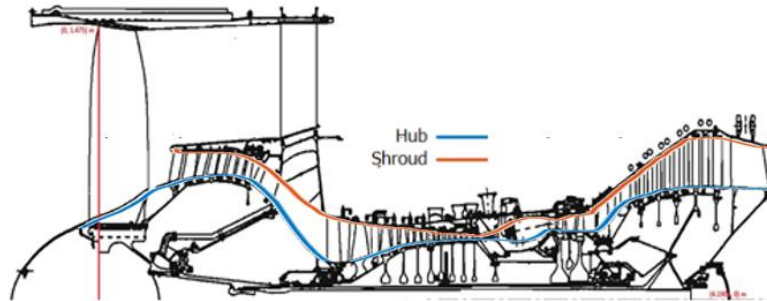


Figure A. 5 Digitized Geometry for GP7275.

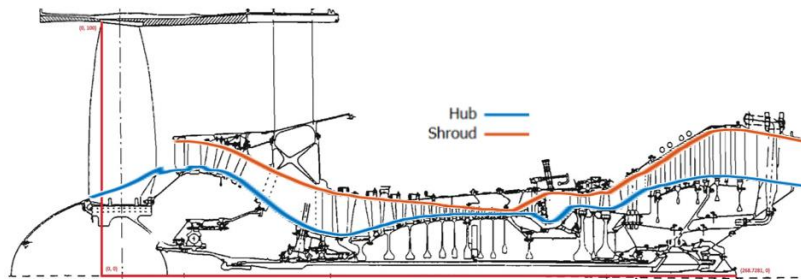


Figure A. 6 Digitized Geometry for GP7176.

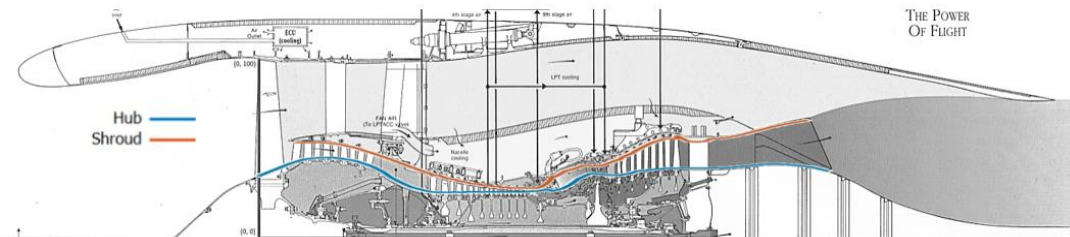


Figure A. 7 Digitized Geometry for CFM56-5C.

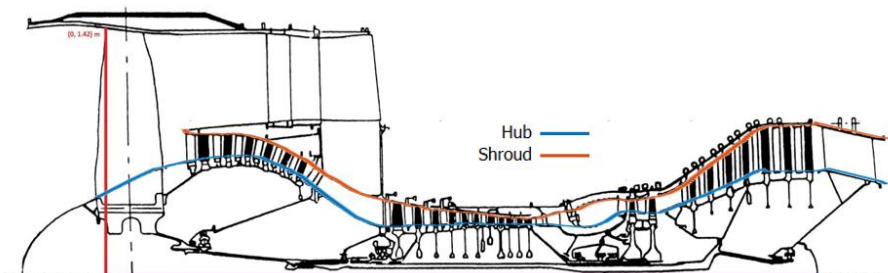


Figure A. 8 Digitized Geometry for PW4084.

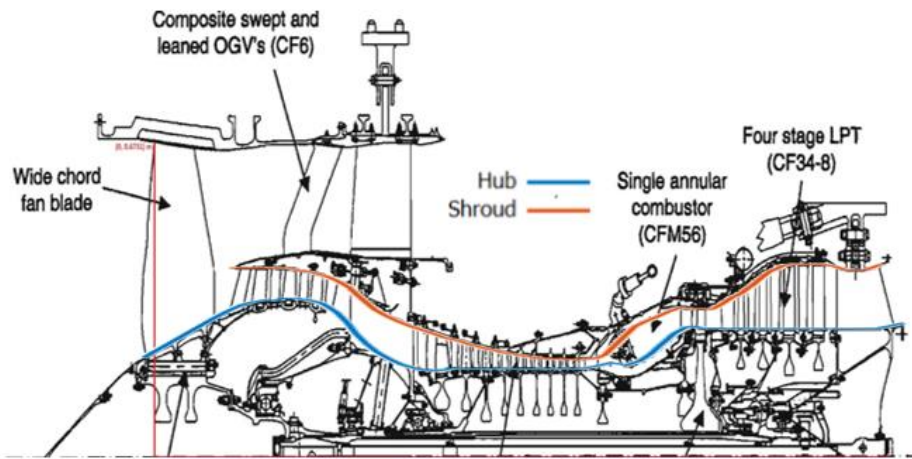


Figure A. 9 Digitized Geometry for CF34-10.

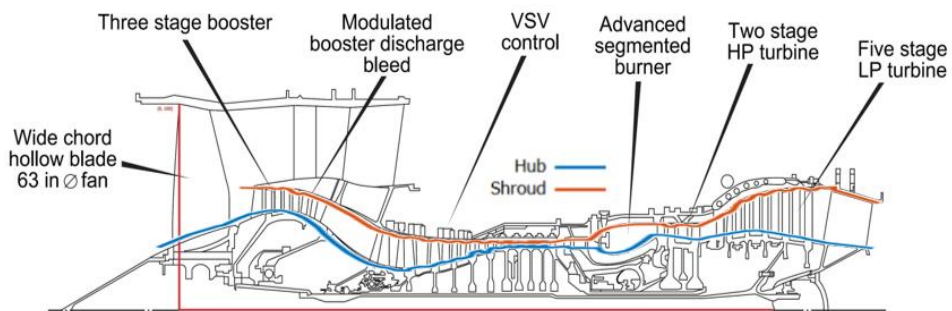


Figure A. 10 Digitized Geometry for V2500-A1.

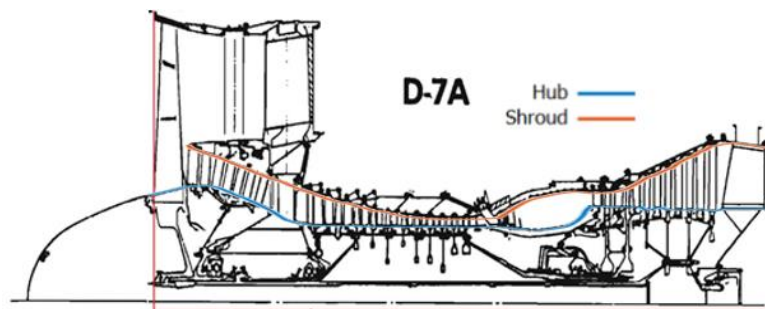


Figure A. 11 Digitized Geometry for JT9D-7.

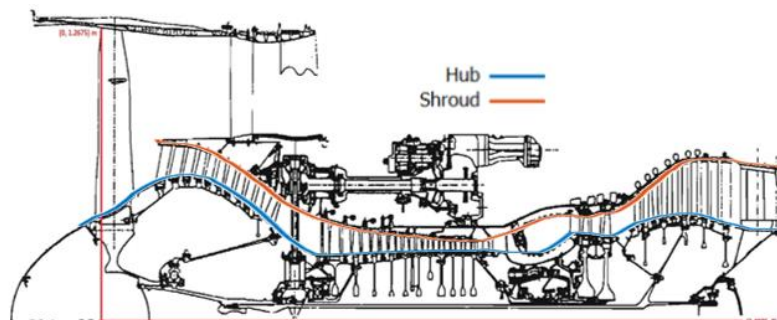


Figure A. 12 Digitized Geometry for PW4000.

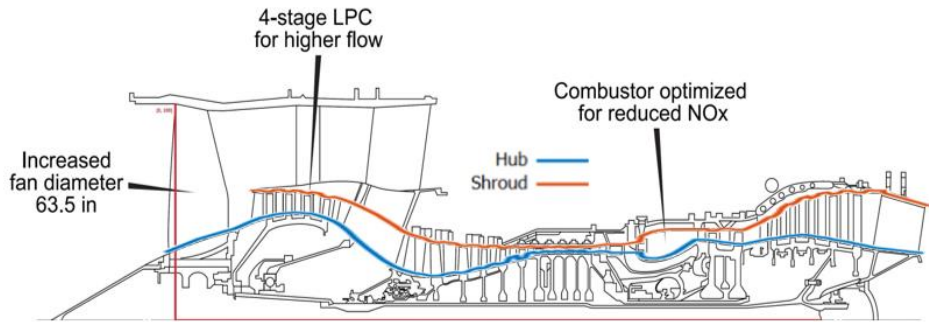


Figure A. 13 Digitized Geometry for V2500-A5.

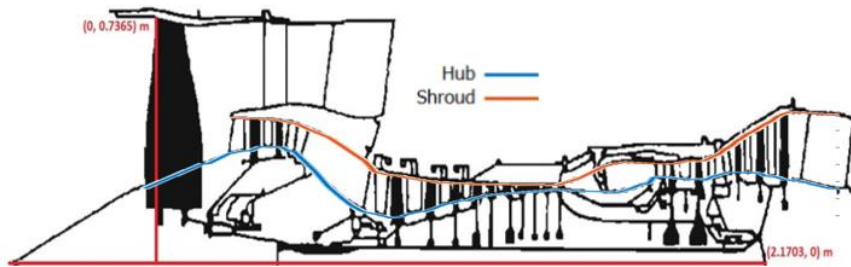


Figure A. 14 Digitized Geometry for BR715.

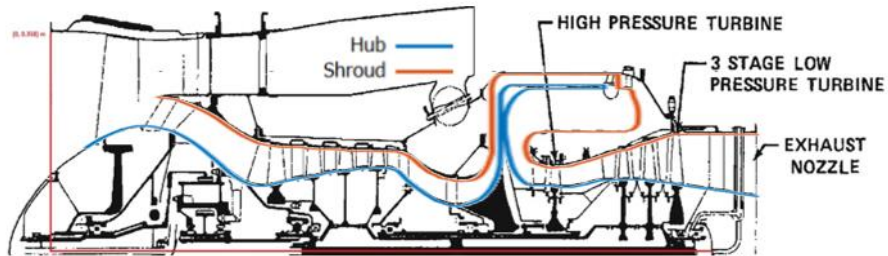


Figure A. 15 Digitized Geometry for TFE731-2.

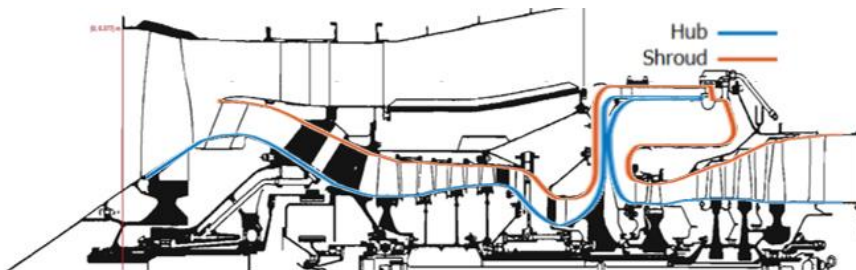


Figure A. 16 Digitized Geometry for TFE731-5.

# Bibliography

- [1] E. Mazareanu, "Number of scheduled passengers boarded by the global airline industry from 2004 to 2021," *Statista*, May 2021.  
<https://www.statista.com/statistics/564717/airline-industry-passenger-traffic-globally/>
- [2] E. Mazareanu, "Worldwide air freight traffic from 2004 to 2021," *Statista*, May 2021.
- [3] D. Dilba, "High-bypass engines of the future," *AEROREPORT, The aviation magazine of MTU Aero Engines*, Feb. 2018.
- [4] Committee on Propulsion and Energy Systems to Reduce Commercial Aviation Carbon Emissions, Aeronautics and Space Engineering Board, Division on Engineering and Physical Sciences, and National Academies of Sciences, Engineering, and Medicine, *Commercial Aircraft Propulsion and Energy Systems Research: Reducing Global Carbon Emissions*. Washington, D.C.: National Academies Press, 2016, p. 23490. doi: 10.17226/23490.
- [5] "New and Future Gas Turbine Propulsion System Technologies," in *Gas Turbine Propulsion Systems*, Chichester, UK: John Wiley & Sons, Ltd, 2011, pp. 257–278. doi: 10.1002/9781119975489.ch11.
- [6] L. Gao, X. Deng, X. Feng, and Z. Yang, "Effect of inlet conditions on compressor intermediate duct," *Proc. Inst. Mech. Eng. Part G J. Aerosp. Eng.*, vol. 229, no. 6, pp. 1154–1168, May 2015, doi: 10.1177/0954410014542624.
- [7] M. K. Karakasis, E. M. J. Naylor, R. J. Miller, and H. P. Hodson, "The Effect of an Upstream Compressor on a Non-Axisymmetric S-Duct," in *Volume 7: Turbomachinery, Parts A, B, and C*, Glasgow, UK, Oct. 2010, pp. 477–486. doi: 10.1115/GT2010-23404.
- [8] P. P. Walsh and P. Fletcher, Eds., "Gas Turbine Engine Components," in *Gas Turbine Performance*, Oxford, UK: Blackwell Science Ltd, 2004, pp. 159–291. doi: 10.1002/9780470774533.ch5.
- [9] N. Chiereghin *et al.*, "Shape Optimization of a Curved Duct with Free Form Deformations," presented at the 23rd AIAA Computational Fluid Dynamics Conference, Denver, Colorado, Jun. 2017. doi: 10.2514/6.2017-4114.
- [10] H. X. Bu, H. J. Tan, H. Chen, and X. M. He, "Investigation on Secondary Flow Characteristics in a Curved Annular Duct with Struts," *Flow Turbul. Combust.*, vol. 97, no. 1, pp. 27–44, Jul. 2016, doi: 10.1007/s10494-015-9674-5.
- [11] A. D. Walker, A. G. Barker, and J. F. Carrotte, "Numerical Design and Experimental Evaluation of an Aggressive S-Shaped Compressor Transition Duct With Bleed," in *Volume 7: Turbomachinery, Parts A, B, and C*, Vancouver, British Columbia, Canada, Jan. 2011, pp. 151–161. doi: 10.1115/GT2011-45628.
- [12] D. Jin, X. Liu, W. Zhao, and X. Gui, "Optimization of endwall contouring in axial compressor S-shaped ducts," *Chin. J. Aeronaut.*, vol. 28, no. 4, pp. 1076–1086, Aug. 2015, doi: 10.1016/j.cja.2015.06.011.

- [13] C. Ortiz Duen~as, R. J. Miller, H. P. Hodson, and J. P. Longley, "Effect of Length on Compressor Inter-Stage Duct Performance," in *Volume 6: Turbo Expo 2007, Parts A and B*, Montreal, Canada, Jan. 2007, pp. 319–329. doi: 10.1115/GT2007-27752.
- [14] T. Stürzebecher, G. Goinis, C. Voss, H. Sahota, P. Groth, and S. Hammer, "Automated Aerodynamic Optimization of an Aggressive S-Shaped Intermediate Compressor Duct," in *Volume 2D: Turbomachinery*, Oslo, Norway, Jun. 2018, p. V02DT46A002. doi: 10.1115/GT2018-75184.
- [15] K. M. Britchford, A. P. Manners, J. J. McGuirk, and S. J. Stevens, "Measurement and Prediction of Flow in Annular S-shaped Ducts," in *Engineering Turbulence Modelling and Experiments*, Elsevier, 1993, pp. 785–794. doi: 10.1016/B978-0-444-89802-9.50077-0.
- [16] D. W. Bailey, K. M. Britchford, J. F. Carrotte, and S. J. Stevens, "Performance Assessment of an Annular S-Shaped Duct," *J. Turbomach.*, vol. 119, p. 8, Jan. 1997.
- [17] P. Bradshaw, "EFFECTS OF STREAMLINE CURVATURE ON TURBULENT FLOW," p. 134.
- [18] Y. T. Ng, S. C. Luo, T. T. Lim, and Q. W. Ho, "On the relation between centrifugal force and radial pressure gradient in flow inside curved and S-shaped ducts," *Phys. Fluids*, vol. 20, no. 5, p. 055109, May 2008, doi: 10.1063/1.2926759.
- [19] M. Sharma and B. D. Baloni, "Review on the aerodynamics of intermediate compressor duct," *J. Mech. Eng. Sci.*, vol. 14, no. 4, pp. 7446–7468, Dec. 2020, doi: 10.15282/jmes.14.4.2020.13.0587.
- [20] P. Taylor, "Developing Flow in S-Shaped Ducts," p. 60.
- [21] A. D. Walker, A. G. Barker, J. F. Carrotte, J. J. Bolger, and M. J. Green, "Integrated OGV Design for an Aggressive S-Shaped Compressor Transition Duct," in *Volume 7: Turbomachinery, Parts A, B, and C*, Vancouver, British Columbia, Canada, Jan. 2011, pp. 139–149. doi: 10.1115/GT2011-45627.
- [22] E. M. J. Naylor, C. O. Dueñas, R. J. Miller, and H. P. Hodson, "Optimization of Nonaxisymmetric Endwalls in Compressor S-Shaped Ducts," *J. Turbomach.*, vol. 132, no. 1, p. 011011, Jan. 2010, doi: 10.1115/1.3103927.
- [23] B. D. Baloni, K. V. Kumar, and S. A. Channiwala, "Study and Numerical Analysis of Compressor Transition Duct," presented at the International Conference of Fluid Flow, Heat and Mass Transfer, Aug. 2017. doi: 10.11159/ffhmt17.108.
- [24] A. D. Walker, A. G. Barker, I. Mariah, G. L. Peacock, J. F. Carrotte, and R. M. Northall, "An Aggressive S-Shaped Compressor Transition Duct With Swirling Flow and Aerodynamic Lifting Struts," in *Volume 2A: Turbomachinery*, Düsseldorf, Germany, Jun. 2014, p. V02AT40A002. doi: 10.1115/GT2014-25844.
- [25] D. W. Bailey and J. F. Carrotte, "The Influence of Inlet Swirl on the Flow Within an Annular S-Shaped Duct," in *Volume 1: Turbomachinery*, Birmingham, UK, Jun. 1996, p. V001T01A016. doi: 10.1115/96-GT-060.
- [26] T. Sonoda, T. Arima, and M. Oana, "The Effect of Inlet Boundary Layer Thickness on the Flow Within an Annular S-Shaped Duct," *J. Turbomach.*, vol. 121, p. 9, Jun. 1999.
- [27] H. Lu, X. Zheng, and Q. Li, "A combinatorial optimization design method applied to S-shaped compressor transition duct design," *Proc. Inst. Mech. Eng. Part G J. Aerosp. Eng.*, vol. 228, no. 10, pp. 1749–1758, Aug. 2014, doi: 10.1177/0954410014531922.

- [28] T. Ghisu, G. T. Parks, J. P. Jarrett, and P. J. Clarkson, "An Integrated System for the Aerodynamic Design of Compression Systems—Part I: Development," *J. Turbomach.*, vol. 133, no. 1, p. 011011, Jan. 2011, doi: 10.1115/1.4000534.
- [29] J. V. Taylor, F. Flanagan, A. Dunlop, S. D. Grimshaw, and R. J. Miller, "SUPER AGGRESSIVES-DUCTS FOR AIR BREATHING ROCKET ENGINES," p. 9, 2020.
- [30] A. D'Ambros, T. Kipouros, P. Zachos, M. Savill, and E. Benini, "Computational Design Optimization for S-Ducts," *Designs*, vol. 2, no. 4, p. 36, Oct. 2018, doi: 10.3390/designs2040036.
- [31] T. Ghisu, G. T. Parks, J. P. Jarrett, and P. J. Clarkson, "An Integrated System for the Aerodynamic Design of Compression Systems—Part II: Application," *J. Turbomach.*, vol. 133, no. 1, p. 011012, Jan. 2011, doi: 10.1115/1.4000535.
- [32] Pooneh Aref, Mehdi Ghoreyshi, Adam Jirasek, and Matthew Satchell, "CFD Validation and Flow Control of RAE-M2129 S-Duct Diffuser Using CREATETM-AV Kestrel Simulation Tools," *Aerospace*, vol. 5, no. 1, p. 31, Mar. 2018, doi: 10.3390/aerospace5010031.
- [33] E. M. V. Siggeirsson, N. Andersson, and F. Wallin, "Numerical and Experimental Study on Bleed Impact on Intermediate Compressor Duct Performance," in *Volume 2B: Turbomachinery*, Oslo, Norway, Jun. 2018, p. V02BT43A008. doi: 10.1115/GT2018-76649.
- [34] L. Davidson, "An Introduction to Turbulence Models," p. 50.
- [35] H. Nepf, "Basics of Turbulent Flow," MIT, Fall 2008. [Online]. Available: <https://ocw.mit.edu/courses/civil-and-environmental-engineering/1-061-transport-processes-in-the-environment-fall-2008/index.htm>
- [36] E. Siggeirsson, "Aerodynamics of an Aeroengine Intermediate Compressor Duct: Effects from an Integrated Bleed System," p. 75.
- [37] Inc. ANSYS, "CFX-Solver Theory Guide." ANSYS, Inc., 2020.
- [38] Y. Zhiyin, "Large-eddy simulation: Past, present and the future," *Chin. J. Aeronaut.*, vol. 28, no. 1, pp. 11–24, Feb. 2015, doi: 10.1016/j.cja.2014.12.007.
- [39] S. Heinz, "A review of hybrid RANS-LES methods for turbulent flows: Concepts and applications," *Prog. Aerosp. Sci.*, vol. 114, p. 100597, Apr. 2020, doi: 10.1016/j.paerosci.2019.100597.
- [40] P. R. Spalart, W.-H. Jou, M. Strelets, and S. R. Allmaras, "Comments on the Feasibility of LES for Wings, and on Hybrid RANS/LES Approach." Conference: Advances in DNS/LES, Jan. 1997.
- [41] P. R. Spalart, "Detached-Eddy Simulation," *Annu. Rev. Fluid Mech.*, vol. 41, no. 1, pp. 181–202, Jan. 2009, doi: 10.1146/annurev.fluid.010908.165130.
- [42] "Detached Eddy Simulation," *Wall-Modeled Large Eddy Simulation Resource*. <https://wmles.umd.edu/hybrid-les-rans-models/des/> (accessed Jul. 26, 2021).
- [43] "Basics of Y Plus, Boundary Layer and Wall Function in Turbulent Flows," *LearnCAx*. <https://www.learncax.com/knowledge-base/blog/by-category/cfd/basics-of-y-plus-boundary-layer-and-wall-function-in-turbulent-flows>
- [44] Inc. ANSYS, "CFX-Solver Modeling Guide." ANSYS, Inc., 2020.
- [45] Inc. ANSYS, "Meshing User's Guide." ANSYS, Inc., 2010.

- [46] I. Yurko and G. Bondarenko, "A New Approach to Designing the S-Shaped Annular Duct for Industrial Centrifugal Compressor," *Int. J. Rotating Mach.*, vol. 2014, pp. 1–10, 2014, doi: 10.1155/2014/925368.
- [47] A. Alexiou, "TURBO 4.0 Library Reference Manual." Laboratory of Thermal Turbomachines, National Technical University of Athens, 2014.



## Εκτεταμένη Περίληψη Διπλωματικής Εργασίας

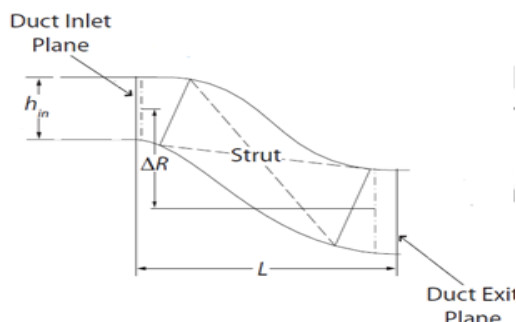
Τα τελευταία χρόνια ο τομέας της αεροπορίας έχει γνωρίσει ραγδαία ανάπτυξη οδηγώντας στην αύξηση του ενδιαφέροντος των ερευνητών για τον σχεδιασμό και την βελτιστοποίηση των αεροπορικών κινητήρων. Πιο συγκεκριμένα, στόχος πλέον είναι η αύξηση της απόδοσης των χρησιμοποιούμενων κινητήρων, κυρίως τύπου Turbofan, που μπορεί να επιτευχθεί μέσω της βελτιστοποίησης της λειτουργίας των επιμέρους τμημάτων τους. Σε αυτή την προσπάθεια σημαντική είναι η συνεισφορά των μεθόδων υπολογιστικής ρευστομηχανικής (Computational Fluid Dynamics, CFD), οι οποίες παρέχουν την δυνατότητα μοντελοποίησης της ροής εντός του κινητήρα.

Ένα από τα τμήματα των αεροπορικών κινητήρων που έχει προσελκύσει αρκετούς από τους ερευνητές είναι ο αγωγός που βρίσκεται ενδιάμεσα των συμπιεστών. Ο ρόλος του είναι η σωστή καθοδήγηση της ροής από τον συμπιεστή χαμηλής (LPC) ή μέσης (IPC) προς τον συμπιεστή υψηλής πίεσης (HPC). Το σχήμα του προσομοιάζεται με το γράμμα της αγγλικής αλφαβήτου "S", και για αυτό συχνά καλείται και αγωγός τύπου S.

Σκοπός αυτής της εργασίας είναι η δημιουργία ενός μοντέλου εκτίμησης των απωλειών πίεσης εντός του συγκεκριμένου αγωγού, βασιζόμενο στα αποτελέσματα προσομοιώσεων CFD. Ένα τέτοιο μοντέλο προϋποθέτει την γνώση των φαινομένων που αναπτύσσονται εντός του αγωγού καθώς και των παραμέτρων που τα επηρεάζουν. Κατά συνέπεια, η ανάπτυξη μίας διαδικασίας παραμετροποίησης του αγωγού και συσχέτισης των απωλειών με τις βασικές της μεταβλητές αποτελεί αναπόσπαστο κομμάτι της εργασίας.

### Η ροή εντός του αγωγού

Στην βιβλιογραφία, ο αγωγός τύπου S, περιγράφεται από ορισμένες γεωμετρικές παραμέτρους. Πιο συγκεκριμένα, από την ακτινική διαφορά εισόδου και εξόδου  $\Delta R$ , το ύψος στην είσοδο  $h_{in}$ , την μέση ακτίνα στην είσοδο  $R_{min}$ , τα εμβαδά εισόδου και εξόδου  $A_{in}, A_{out}$  και το μήκος  $L$ , οι λόγοι των οποίων αποτελούν τις βασικές αδιάστατες παραμέτρους σχεδίασής του.



Σχήμα 1 Γεωμετρία Αγωγού.

Parameter	Typical Value
$\Delta R/L$	0.30-0.45
$h_{in}/L$	0.1-0.3
$r_{in}/L$	1.5-1.7
$t/c$	0.14-0.30
$A_{ex}/A_{in}$	0.6-0.7

Πίνακας 1 Βασικές Παράμετροι.

Αδιάστατοι συντελεστές χρησιμοποιούνται ως μέτρα της αποδοτικής λειτουργίας του αγωγού. Οι συντελεστές  $\omega$ ,  $DP/P$  εκφράζουν την απώλεια ολικής πίεσης κατά μήκος του αγωγού ως ποσοστό της δυναμικής πίεσης και της ολικής πίεσης στην είσοδό του, αντίστοιχα. Ένας ακόμη χρήσιμος συντελεστής είναι το  $C_p$  που σχετίζεται με την κατανομή της στατικής πίεσης.

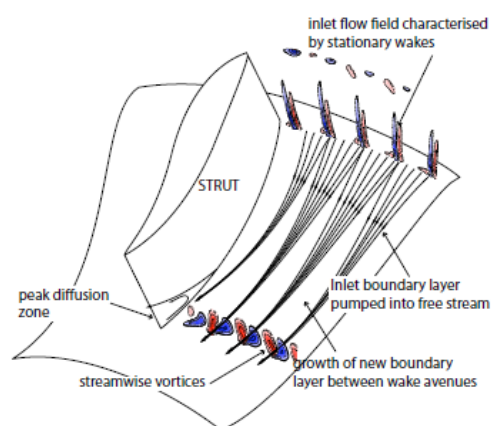
$$\omega = \frac{\bar{P}_{tin} - \bar{P}_{tout}}{\bar{P}_{tin} - \bar{P}_{sin}} \quad (1)$$

$$\frac{DP}{P} = \frac{\bar{P}_{tin} - \bar{P}_{tout}}{\bar{P}_{tin}} \quad (2)$$

$$C_p = \frac{P_s - \bar{P}_{sref}}{\bar{P}_{tref} - \bar{P}_{sref}} \quad (3)$$

Όπως φαίνεται στο Σχήμα 1, το τοίχωμα της πλήμνης (Hub), αποτελείται από μία κυρτή περιοχή που ακολουθείται από μία κοίλη ενώ για το κέλυφος (Shroud) η σειρά είναι ανεστραμμένη. Λόγω αυτής της καμπυλότητας, εντός του δημιουργείται διαφορά πίεσης, ανάμεσα στην πλήμνη και το κέλυφος, που σε συνδυασμό με τις φυγόκεντρες δυνάμεις που ασκούνται στην ροή οδηγεί στην εμφάνιση μίας περιοχής αποκόλλησης.

Όταν ο αγωγός τοποθετηθεί στην έξοδο του συμπιεστή, λόγω της ύπαρξης της τελευταίας βαθμίδας του LPC, των οδηγών περυγίων (OGVs), η περιοχή αποκόλλησης τείνει να συρρικνωθεί αλλά παρατηρείται αύξηση των απωλειών πίεσης. Μία ακόμη παράμετρος που επηρεάζει σημαντικά την ροή εντός του αγωγού είναι η ύπαρξη υποστυλωμάτων, που ονομάζονται Struts, και δημιουργούν μία περιοχή έντονης επιβράδυνσης που οδηγεί σε αύξηση της πιθανότητας εμφάνισης φαινομένων αποκόλλησης.



Σχήμα 2 Φαινόμενα εντός του αγωγού.

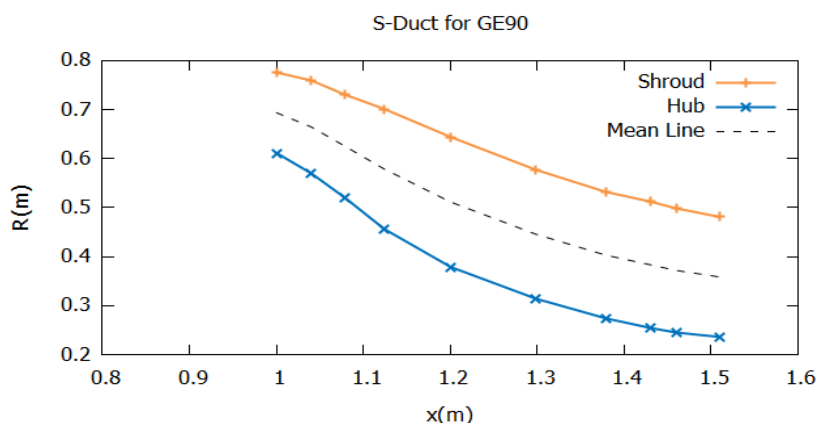
Οι συνθήκες εισόδου της ροής, δηλαδή η ύπαρξη η όχι στροβιλότητας (swirl), ο αριθμός Mach και το πάχος του οριακού στρώματος μπορούν να επηρεάσουν την αναπτυσσόμενη

ροή. Με την ύπαρξη γωνίας στροβιλότητας στην είσοδο του αγωγού η ροή επιταχύνεται, λόγω της μειούμενης ακτίνας, μειώνοντας την πιθανότητα αποκόλλησης αλλά οδηγώντας σε αύξηση των απωλειών πίεσης. Το πάχος του εισερχόμενου οριακού στρώματος οδηγεί σε δημιουργία ενός ζεύγους δινών που συνεισφέρει στις απώλειες κοντά στα τοιχώματων.

Για την βελτίωση της απόδοσης του ενδιάμεσου αγωγού τύπου S, έχουν προταθεί ποικίλες μέθοδοι. Πολλοί ερευνητές, αξιοποιούν ήδη υπάρχουσες τεχνικές βελτιστοποίησης, όπως η Response Surface Methodology, σε συνδυασμό με τις CFD προσομοιώσεις για την εκπαίδευση Τεχνητών Νευρωνικών Δικτύων, ώστε να αναγνωρίσουν την βέλτιστη γεωμετρία του αγωγού, συμμετρική η ασύμμετρη. Μία ακόμη μέθοδος που αξιοποιείται για την βελτίωση του συνολικού σχεδιασμού και της απόδοσης των αεροπορικών κινητήρων βασίζεται σε μία πιο ολοκληρωτική προσέγγιση (Integrated Design). Σύμφωνα με αυτήν, ο αγωγός πρέπει να αναλύεται ως ένα ενιαίο σύστημα με τους συμπιεστές έτσι ώστε να μην εξασφαλίζεται μόνο η βέλτιστη λειτουργία για κάθε μέρος της μηχανής ξεχωριστά, αλλά και όταν αυτά συνεργάζονται, καθώς τότε εισάγονται περαιτέρω περιορισμοί. Τέλος, η εγκατάσταση συσκευών ελέγχου της ροής (Flow Controlling Devices) και η αξιοποίηση του αγωγού απομάστευσης αέρα, για την επιτάχυνση του οριακού στρώματος και την αποφυγή της αποκόλλησης, αποτελούν μερικές από τις λύσεις που εξετάζονται από τους κατασκευαστές.

## Ανάλυση και Παραμετροποίηση αγωγών υπαρκτών κινητήρων τύπου Turbofan

Στα πλαίσια αυτής της εργασίας, οι αγωγοί τύπου S δεκαεφτά αεροπορικών κινητήρων ψηφιοποιήθηκαν με χρήση του προγράμματος Plot Digitizer. Πιο συγκεκριμένα, για κάθε μηχανή σημεία τοποθετήθηκαν κατά μήκος του κελύφους και της πλήμνης στο τμήμα του κύριου ρεύματος (core), προκειμένου να υπολογιστούν οι ακτίνες σε κάθε σημείο. Έτσι ήταν δυνατή η ανακατασκευή της γεωμετρίας του αγωγού, όπως φαίνεται χαρακτηριστικά για τον GE90 στο Σχήμα 3.



Σχήμα 3 Ο ψηφιοποιημένος αγωγός του GE90.

Στόχος αυτής της διαδικασίας ήταν η εξαγωγή των κύριων γεωμετρικών παραμέτρων που περιγράφουν κάθε αγωγό, όπως φαίνονται στον Πίνακα 2.

Engine	L (m)	$\left(\frac{R_{hub}}{R_{shroud}}\right)_{in}$	$\left(\frac{R_{hub}}{R_{shroud}}\right)_{out}$	$\frac{A_{out}}{A_{in}}$	$\frac{\Delta R}{L}$	$\frac{h_{in}}{L}$	$\frac{R_{min}}{L}$
PW1000G	0.5688	0.8049	0.7617	0.6039	0.1995	0.1413	0.6535
PW1000G (Early Version)	0.2564	0.8510	0.7037	0.9387	0.4535	0.2141	1.3301
PW8000	0.2935	0.8199	0.6215	1.1348	0.3127	0.2019	1.0203
GE90	0.5088	0.7880	0.4906	0.7707	0.6581	0.3232	1.3629
TRENT900	0.2338	0.8344	0.8290	0.6678	0.3184	0.2921	1.6174
GP7275	0.3477	0.8085	0.4818	0.8542	0.9060	0.3903	1.8432
GP7176	0.3595	0.7486	0.4822	0.8444	0.6417	0.4475	1.5564
CFM56-5C	0.3578	0.8189	0.7095	0.8155	0.3366	0.2170	1.0898
PW4084	0.4568	0.8046	0.6650	0.8143	0.3994	0.2558	1.1814
CF34-10	0.2099	0.8223	0.6904	0.8669	0.5234	0.3183	1.6321
V2500-A1	0.3956	0.7774	0.5607	0.8184	0.3912	0.2470	0.9865
JT9D-7	0.2740	0.7689	0.7427	0.8532	0.2274	0.4536	1.7359
PW4000	0.2396	0.7377	0.6689	0.7721	0.4271	0.5887	1.9504
V2500-A5	0.3948	0.7827	0.5539	0.8595	0.3996	0.2460	1.0092
BR715	0.2762	0.7885	0.5582	0.8088	0.5689	0.3209	1.3570
TFE731-2	0.1049	0.8164	0.6698	0.8447	0.4892	0.2889	1.4291
TFE731-5	0.1065	0.8229	0.6735	0.8587	0.4806	0.2698	1.3886
<b>Average</b>	-	0.7998	0.6390	0.8310	0.4549	0.3068	1.3614
<b>Min. Value</b>	-	0.7377	0.4818	0.6039	0.1995	0.1413	0.6535
<b>Max. Value</b>	-	0.8510	0.8290	1.1348	0.9060	0.5887	1.9504

Πίνακας 2 Γεωμετρικές παράμετροι για τους αγωγούς των Turbofan μηχανών.

Παρατηρήθηκε ότι η κατανομή της ακτίνας, τόσο της πλήμνης όσο και του κελύφους, περιγράφεται με ικανοποιητική ακρίβεια από ένα πολυώνυμο δευτέρου βαθμού. Αναλυτικότερα, για την διαδικασία παραμετροποίησης ήταν σημαντική η εξαγωγή των αδιάστατων κατανομών των ακτίνων  $r$ , ως συνάρτηση της αδιάστατης απόστασης  $x$ .

$$x = \frac{x_{real} - x_{in}}{x_{out} - x_{in}}, \quad x \in [0,1] \quad (4)$$

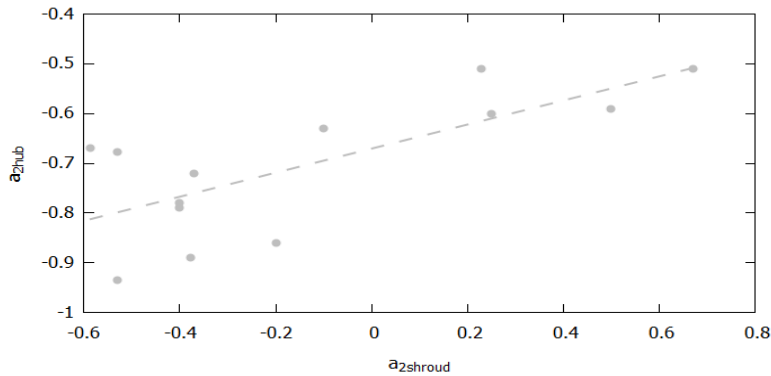
$$r = \frac{R - R_{in}}{R_{out} - R_{in}} = a_2 x^2 + a_1 x, \quad r \in [0,1] \quad (5)$$

$$a_2 + a_1 = 1 \quad (6)$$

Οι συντελεστές  $a_2, a_1$  είναι εκείνοι που περιγράφουν την καμπυλότητα των τοιχωμάτων. Ωστόσο, σκοπός της παραμετροποίησης είναι η διατήρηση μόνο των απαραίτητων μεταβλητών για την ακριβή περιγραφή της γεωμετρίας. Έτσι, οι συντελεστές  $a_1$  μέσω της (6) προκύπτουν από τους αντίστοιχους  $a_{2shroud}$  ενώ ο  $a_{2hub}$  μπορεί να συσχετιστεί με τον  $a_{2shroud}$  μέσω της σχέσης (7). Αυτή η μαθηματική εξάρτηση προέκυψε από τα αποτελέσματα της ψηφιοποίησης και δεν αντιστοιχεί σε κάποια από τις προσεγγίσεις που

εξετάζονται στην βιβλιογραφία. Ωστόσο, η χρήση της, δεν επηρεάζει την ακρίβεια των αποτελεσμάτων, αφού οι περιορισμοί που σχετίζονται με την ύπαρξη υποστυλωμάτων, μετρητικών οργάνων ή άλλων παραγόντων, δεν συνυπολογίζονται στην παρούσα εργασία.

$$a_{2hub} = 0.2417a_{2shroud} - 0.6706 \quad (7)$$



Σχήμα 4 Συσχέτιση συντελεστών  $a_{2shroud}$  και  $a_{2hub}$ .

Μία αντίστοιχη διαδικασία ακολουθήθηκε για την εύρεση της αδιάστατης κατανομής του εμβαδού της διατομής του αγωγού, η οποία περιγράφεται από ένα πολυώνυμο τρίτου βαθμού με συντελεστές  $b_1, b_2, b_3$ . Οι συντελεστές αυτοί μπορούν να προκύψουν άμεσα από τις κατανομές των ακτίνων.

$$\alpha = \frac{A - A_{in}}{A_{out} - A_{in}} = b_3x^3 + b_2x^2 + b_1x, \quad \alpha \in [0,1] \quad (8)$$

$$b_3 + b_2 + b_1 = 1 \quad (9)$$

Στην συνέχεια, αναπτύχθηκαν δύο διαδικασίες παραμετροποίησης του αγωγού τύπου S. Και στις δυο διαδικασίες, ο χρήστης οφείλει να εισάγει ως δεδομένα την παροχή μάζας ρευστού που διέρχεται από τον αγωγό, τις τιμές των  $P_t, T_t$ , καθώς και τις ιδιότητες του μέσου  $\gamma, R$ . Για την πρώτη διαδικασία, *Process I*, ως δεδομένα λαμβάνονται τα  $\Delta R/L, h_{in}/L, R_{min}/L, A_{out}/A_{in}$ , η τιμή του  $a_{2shroud}$  καθώς και το μήκος του αγωγού L. Με χρήση των γεωμετρικών σχέσεων που συσχετίζουν τα μεγέθη του αγωγού είναι δυνατός ο υπολογισμός των ακτίνων πλήμνης και κελύφους, της μέσης ακτίνας του και της κατανομής του εμβαδού των διατομών κατά μήκος του. Για την δεύτερη διαδικασία, τα δεδομένα είναι ο λόγος των ακτίνων των τοιχωμάτων στην είσοδο και την έξοδο  $(R_{hub}/R_{shroud})_{in}, (R_{hub}/R_{shroud})_{out}$ , το μήκος του αγωγού, ο συντελεστής  $a_{2shroud}$  καθώς και οι αριθμοί Mach της εισερχόμενης και εξερχόμενης ροής. Ο λόγος που επιλέγεται η χρήση του λόγου ακτίνων είναι ότι αποτελεί μία βασική παράμετρο που αξιοποιείται από τους σχεδιαστές για τους συμπιεστές. Οι αριθμοί Mach χρησιμοποιούνται για την εύρεση των εμβαδών στην είσοδο και την έξοδο του αγωγού, με βάση την σχέση (10).

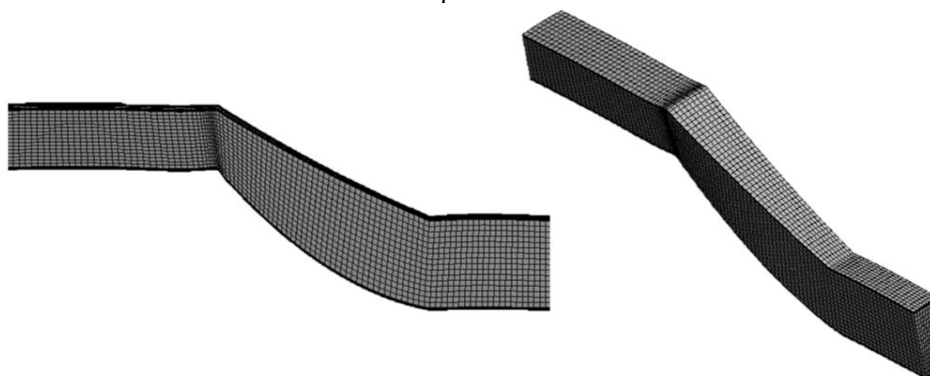
$$A = \frac{\dot{m}}{\frac{P_t}{\sqrt{T_t}} \sqrt{\frac{\gamma}{R}} M \left(1 + \frac{\gamma-1}{2} M^2\right)^{-\frac{\gamma+1}{2(\gamma-1)}}} \quad (10)$$

## Προσομοίωση της ροής στο λογισμικό ANSYS CFX

Η γεωμετρία των αγωγών που προκύπτει από την διαδικασία παραμετροποίησης εισάγεται στο λογισμικό ANSYS, όπου προσομοιώνεται η εσωτερική ροή τους. Η ροή χαρακτηρίζεται από περιοδικότητα και κατά συνέπεια δεν είναι ανάγκη να γίνει επίλυση όλου του αγωγού αλλά αρκεί η επίλυση της ροής για ένα τμήμα του 10°.

Το πρώτο βήμα είναι η δημιουργία του πλέγματος για το εξεταζόμενο τμήμα του αγωγού. Για την πλεγματοποίηση χρησιμοποιήθηκαν εξαεδρικά στοιχεία σε όλη την επιφάνεια του αγωγού, των οποίων το μέγεθος καθορίστηκε από την μελέτη ανεξαρτησίας του πλέγματος, που έγινε για την περίπτωση του αγωγού του GE90 (Base Case). Από αυτήν προέκυψε πλέγμα με πλήθος κόμβων περίπου 70000, που προσφέρει ικανοποιητική ακρίβεια στην προσομοίωση, όπως φαίνεται στο Σχήμα 6. Εκτός του πλήθους των στοιχείων σημαντικός είναι και ο καθορισμός των χαρακτηριστικών του πλέγματος στην περιοχή κοντά στα τοιχώματα. Σε αυτές τις θέσεις γίνεται εκλέπτυνση του πλέγματος ώστε να εξασφαλιστεί η πλήρης επίλυση του οριακού στρώματος. Για τον λόγο αυτό επιλέχθηκε το ύψος του πρώτου στοιχείου  $\Delta y$  (First element height) καθώς και ο βαθμός ανάπτυξης τους (Growth Rate), ώστε το αδιάστατο ύψος να διατηρηθεί κοντά στην μονάδα,  $y^+ \approx 1$ .

$$y^+ = \frac{\rho \Delta y u_\tau}{\mu} \quad (11)$$



Σχήμα 5 Πλέγμα που δημιουργήθηκε εντός του ANSYS.

Στην συνέχεια έγινε η επιλογή των φυσικών μοντέλων που χρησιμοποιούνται από το CFX για την επίλυση της ροής εντός του αγωγού. Το μέσο θεωρήθηκε ιδεατό (Air Ideal Gas), ενώ για την προσομοίωση αντιστοιχεί σε σταθερές συνθήκες (Steady State). Το χρησιμοποιούμενο μοντέλο τύρβης είναι τύπου k- $\omega$  και ονομάζεται Shear Stress Transport Model. Αυτό το μοντέλο επιλέγεται ευρέως για τις προσομοιώσεις ροής εντός στροβιλομηχανών, καθώς προσφέρει έναν ικανοποιητικό συμβιβασμό μεταξύ ακρίβειας και υπολογιστικού κόστους.

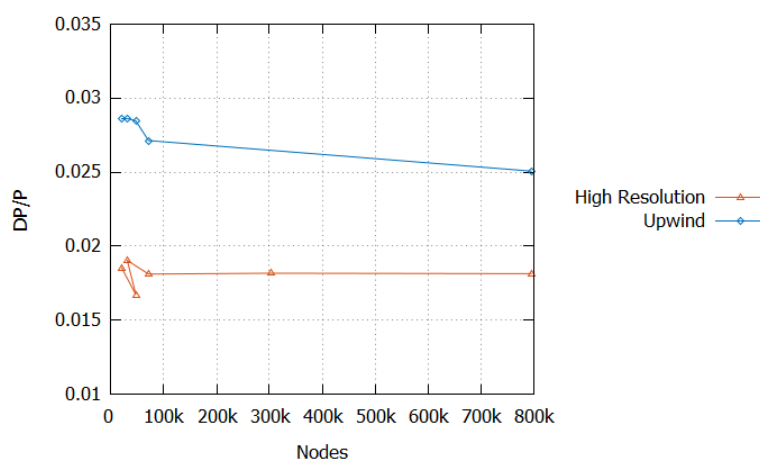
Οι οριακές συνθήκες για την είσοδο και την έξοδο του τομέα λήφθηκαν από τα δεδομένα της βιβλιογραφίας για τον GE90 εφαρμόζοντας τις θερμοδυναμικές σχέσεις που ισχύουν για κινητήρες τύπου Turbofan και ανήχθησαν στις τυπικές συνθήκες πίεσης και

θερμοκρασίας. Η τραχύτητα των τοιχωμάτων της πλήμνης και του κελύφους δεν λήφθηκε υπόψιν.

$P_{t_{in}}$ (bar)	1.01325
$T_{t_{in}}$ (K)	288.15
$\dot{m}$ (kg/s)	100

Πίνακας 3 Οριακές συνθήκες.

Τέλος, σχήμα επίλυσης που επιλέχθηκε ήταν το High-Resolution Advection Scheme που συνδυάζει το σχήμα πρώτης και δεύτερης τάξης, με αυτόματη επιλογή ανάλογα με τις ανάγκες της προσομοίωσης. Αυτή η επιλογή έγινε έπειτα από σύγκριση των διαθέσιμων μεθόδων όπως φαίνεται στο Σχήμα 6.

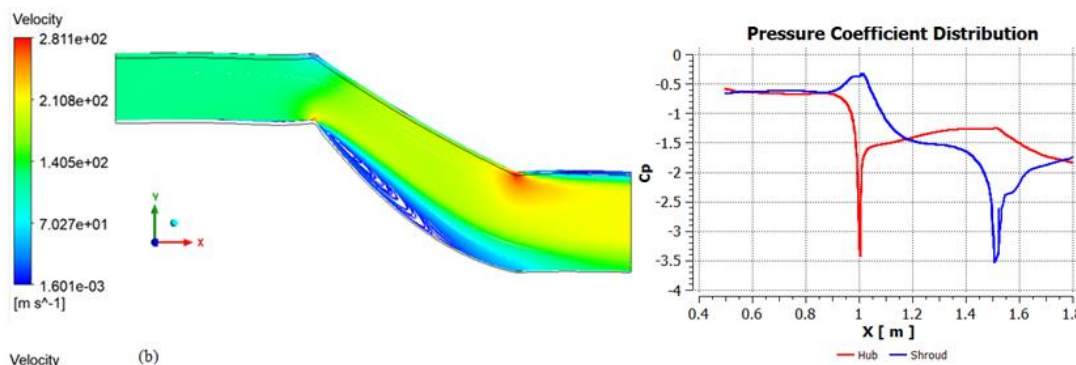


Σχήμα 6 Μελέτη ανεξαρτησίας πλέγματος.

Μετά το πέρας της προσομοίωσης τα αποτελέσματα είναι διαθέσιμα προς επεξεργασία στο CFX-Post, όπου υπολογίζονται και οι συντελεστές πίεσης του Πίνακα 4. Για τον αγωγό του GE90 οι ροϊκές γραμμές καθώς και η κατανομή της στατική πίεσης φαίνονται στο Σχήμα 7. Είναι ορατή η περιοχή αποκόλλησης κοντά στο τοίχωμα της πλήμνης.

Parameter	CFX Result
$M_{in}$	0.36187
$M_{out}$	0.59663
$\omega$	0.13668
$DP/P$	1.811%

Πίνακας 4 Αποτελέσματα προσομοίωσης για GE90.



Σχήμα 7 Αποτελέσματα προσομοίωσης για GE90.

### Δημιουργία Μοντέλου Εκτίμησης Απωλειών Πίεσης

Για την σύνθεση του μοντέλου εκτίμησης του συντελεστή απωλειών  $DP/P$  ήταν σημαντική η εύρεση των μαθηματικών σχέσεων που περιγράφουν την επιρροή των αδιάστατων γεωμετρικών παραμέτρων, που χρησιμοποιούνται για την περιγραφή του αγωγού, στις απώλειες ολικής πίεσης εντός του. Για τον λόγο αυτό, με χρήση του ANSYS CFX, υπολογίστηκαν οι απώλειες για μεταβαλλόμενες τιμές κάθε παραμέτρου. Οι παράμετροι αυτοί εμφανίζονται στις σχέσεις που ακολουθούν ως ποσοστά των τιμών αναφοράς τους, που στα πλαίσια αυτής της εργασίας αντιστοιχούν στον κινητήρα GE90, και φαίνονται στον Πίνακα 5. Τα εύρη εντός των οποίων επιλέχθηκαν οι τιμές για τις προσομοιώσεις αντιστοιχούν σε αυτά που βρέθηκαν από την ψηφιοποίηση των μηχανών.

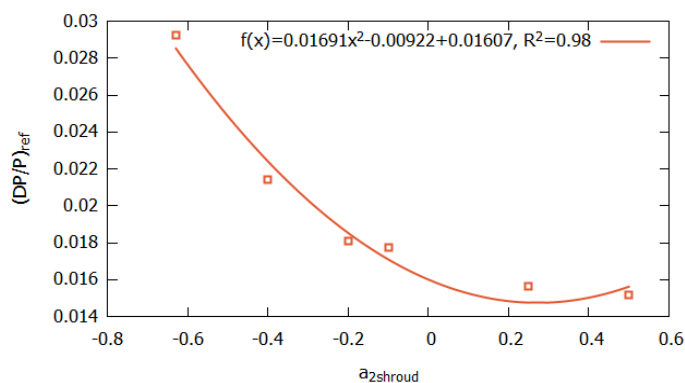
Parameter	Reference Values
$A_{out}/A_{in}$	0.7707
$\Delta R/L$	0.6581
$h_{in}/L$	0.3232
$R_{min}/L$	1.3629

Πίνακας 5 Τιμές αναφοράς αδιάστατων παραμέτρων.

Αρχικά, μέσω της μεταβολής του συντελεστή  $a_{2_{shroud}}$  προέκυψε η σχέση υπολογισμού των απωλειών για τις τιμές αναφοράς, (12). Όσο το  $a_{2_{shroud}}$  αυξάνεται οι απώλειες τείνουν να μειωθούν, αφού ο αγωγός χάνει το S σχήμα του και η περιοχή αποκόλλησης περιορίζεται.

$$(DP/P)_{ref} = 0.01691a_{2_{shroud}}^2 - 0.00922a_{2_{shroud}} + 0.01607 \quad (12)$$





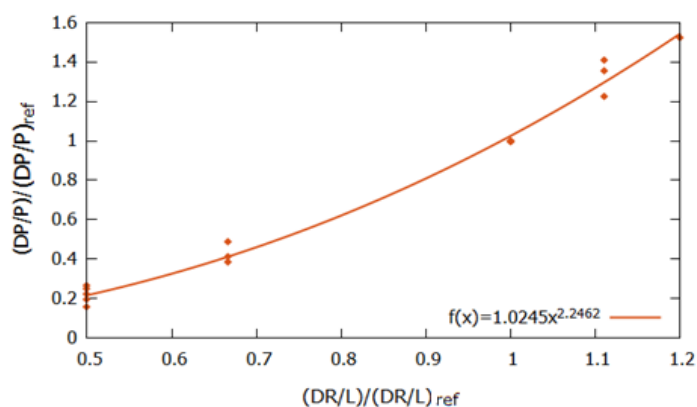
Σχήμα 8 Συσχέτιση συντελεστή απωλειών με  $a_{2shroud}$ .

Η μεταβολή της παραμέτρου  $\Delta R/L$  έχει σημαντική επιρροή στην διαμόρφωση της ροής και των απωλειών εντός του αγωγού. Πιο συγκεκριμένα, μείωση αυτής τη παραμέτρου, δηλαδή αύξηση του μήκους ή μείωση της ακτινικής διαφοράς εισόδου-εξόδου, οδηγεί σε μείωση των απωλειών. Παρατηρήθηκε ότι για υποδιπλασιασμό της παραμέτρου η περιοχή αποκόλλησης συρρικνώνεται και σχεδόν εξαφανίζεται. Από τις προσομοιώσεις που εκτελέστηκαν για  $\Delta R/L$ : (50% – 120%)  $(\Delta R/L)_{ref}$ , και για διάφορα  $a_{2shroud}$ , εξήχθη το συμπέρασμα ότι η συσχέτισή τους δίνεται από εκθετική συνάρτηση της μορφής (13).

$$\frac{DP/P}{(DP/P)_{ref}} = b_1 \left[ \frac{\Delta R/L}{(\Delta R/L)_{ref}} \right]^{b_2} \quad (13)$$

Ωστόσο, δεν βρέθηκε συσχέτιση για τις τιμές των συντελεστών  $b_1$ ,  $b_2$  και το  $a_{2shroud}$ . Έτσι, υπολογίστηκαν οι τιμές τους που μπορούν να χρησιμοποιηθούν για τον υπολογισμό του  $DP/P$  ανεξαρτήτως του συντελεστή  $a_{2shroud}$ .

$$\frac{DP/P}{(DP/P)_{ref}} = 1.0245 \left[ \frac{\Delta R/L}{(\Delta R/L)_{ref}} \right]^{2.2462} \quad (14)$$

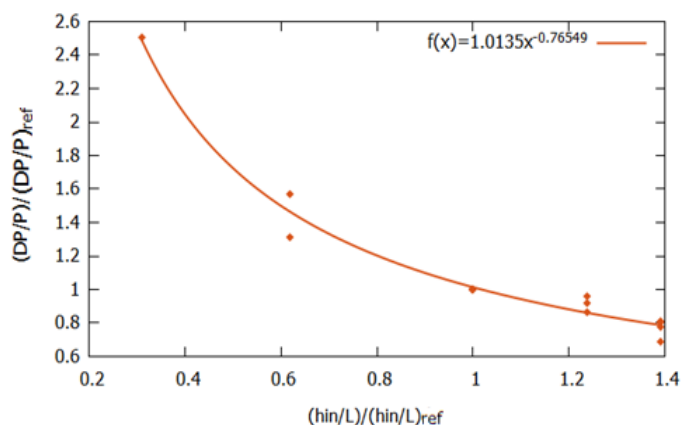


Σχήμα 9 Συσχέτιση συντελεστή απωλειών με  $\Delta R/L$ .

Παρόμοια διαδικασία ακολουθήθηκε και για τις παραμέτρους  $h_{in}/L$ ,  $R_{min}/L$ . Στην περίπτωση της πρώτης παραμέτρου, το εύρος διακύμανσής για τις προσομοιώσεις ήταν

(62% – 139%)  $(h_{in}/L)_{ref}$  και η επιρροή της στον συντελεστή απωλειών δίνεται και πάλι από την εκθετική συνάρτηση. Για την απαλοιφή της εξάρτησης από το  $a_{2shroud}$  είναι δυνατή και πάλι η χρήση μίας, ενιαίας σχέσης (15).

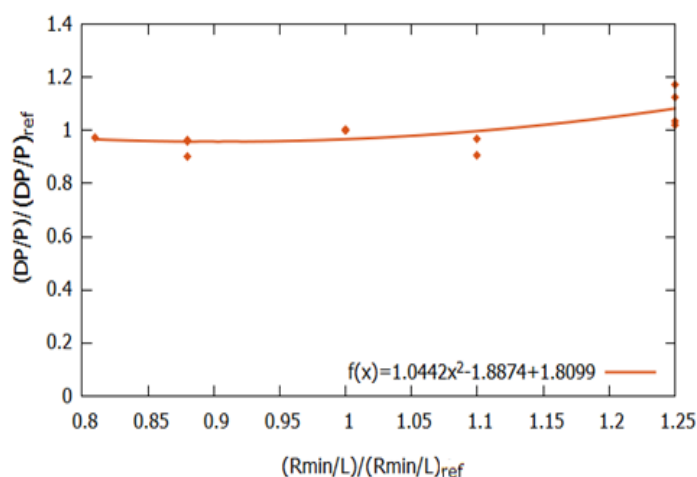
$$\frac{DP/P}{(DP/P)_{ref}} = 1.0135 \left[ \frac{h_{in}/L}{(h_{in}/L)_{ref}} \right]^{-0.7655} \quad (15)$$



Σχήμα 10 Συσχέτιση συντελεστή απωλειών με  $h_{in}/L$ .

Για τις τιμές του λόγου  $R_{min}/L$ : (88% – 125%)  $(R_{min}/L)_{ref}$  η επιρροή στις απώλειες ολικής πίεσης δίνεται από ένα πολυώνυμο δευτέρου βαθμού. Οι συντελεστές του μεταβάλλονται αμελητέα και χωρίς συγκεκριμένη τάση με την τιμή του  $a_{2shroud}$ . Κατά συνέπεια, η εξάρτηση αυτή είναι δυνατό να αποφευχθεί χρησιμοποιώντας τους συντελεστές που, με βάση τον αλγόριθμο ελαχίστων τετραγώνων, μπορούν να περιγράψουν την συσχέτιση των μεγεθών για όλα τα  $a_{2shroud}$ .

$$\frac{DP/P}{(DP/P)_{ref}} = 1.0442 \left[ \frac{R_{min}/L}{(R_{min}/L)_{ref}} \right]^2 + 1.8874 \left[ \frac{R_{min}/L}{(R_{min}/L)_{ref}} \right] + 1.8099 \quad (16)$$



Σχήμα 11 Συσχέτιση συντελεστή απωλειών με  $R_{min}/L$ .

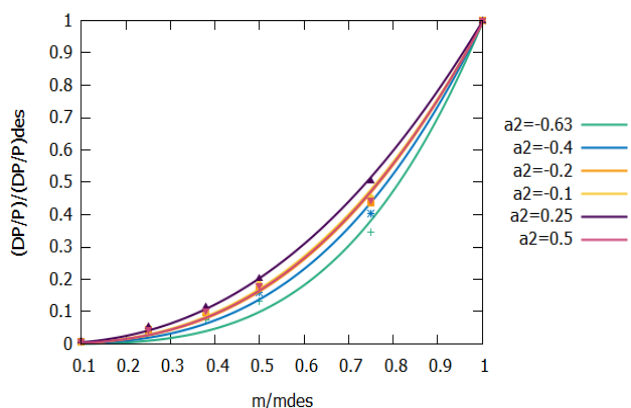
Για την παράμετρο  $A_{out}/A_{in}$  παρατηρήθηκε αμελητέα επίδραση στις απώλειες και δεν ήταν δυνατή η εύρεση άμεσης συσχέτισης με τον συντελεστή  $DP/P$ .

Ο συνδυασμός των εξισώσεων (14),(15),(16) αξιοποιείται για τον υπολογισμό του συντελεστή απωλειών ολικής πίεσης στο σημείο σχεδιασμού (Design Point),  $(DP/P)_{des}$ , που αντιστοιχεί στο 100% της παροχής μάζας αέρα για την οποία έχει σχεδιαστεί ο κινητήρας. Για τις απώλειες εκτός αυτού του σημείου, για χαμηλότερα ποσοστά της παροχής, αναμένεται οι απώλειες να μεταβάλλονται. Στην βιβλιογραφία, η εξάρτηση των απωλειών από την παροχή συχνά περιγράφεται μέσω της (17), με τον εκθέτη ίσο με 2.

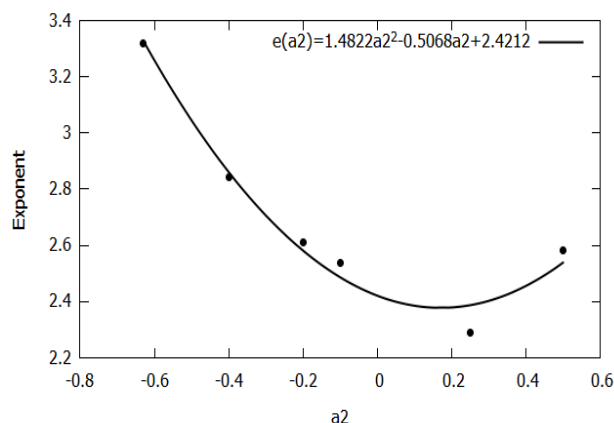
$$\frac{DP/P}{(DP/P)_{des}} = \left[ \frac{\dot{m}}{\dot{m}_{des}} \right]^{\text{exponent}} \quad (17)$$

Εκτελώντας τις προσομοιώσεις για μεταβλητές τιμές του  $a_{2shroud}$  και της παροχής  $\dot{m}$ , προέκυψε άμεση εξάρτηση του εκθέτη από το σχήμα του αγωγού, που δίνεται από την (18). Αναλυτικότερα, στο Σχήμα 12 φαίνονται οι καμπύλες που προέκυψαν για τα διαφορετικά  $a_{2shroud}$ , ενώ στο Σχήμα 13 παρατηρείται η εξάρτηση του εκθέτη από την τιμή του συντελεστή.

$$\text{exponent} = 1.4822a_{2shroud}^2 - 0.5068a_{2shroud} + 2.4212 \quad (18)$$

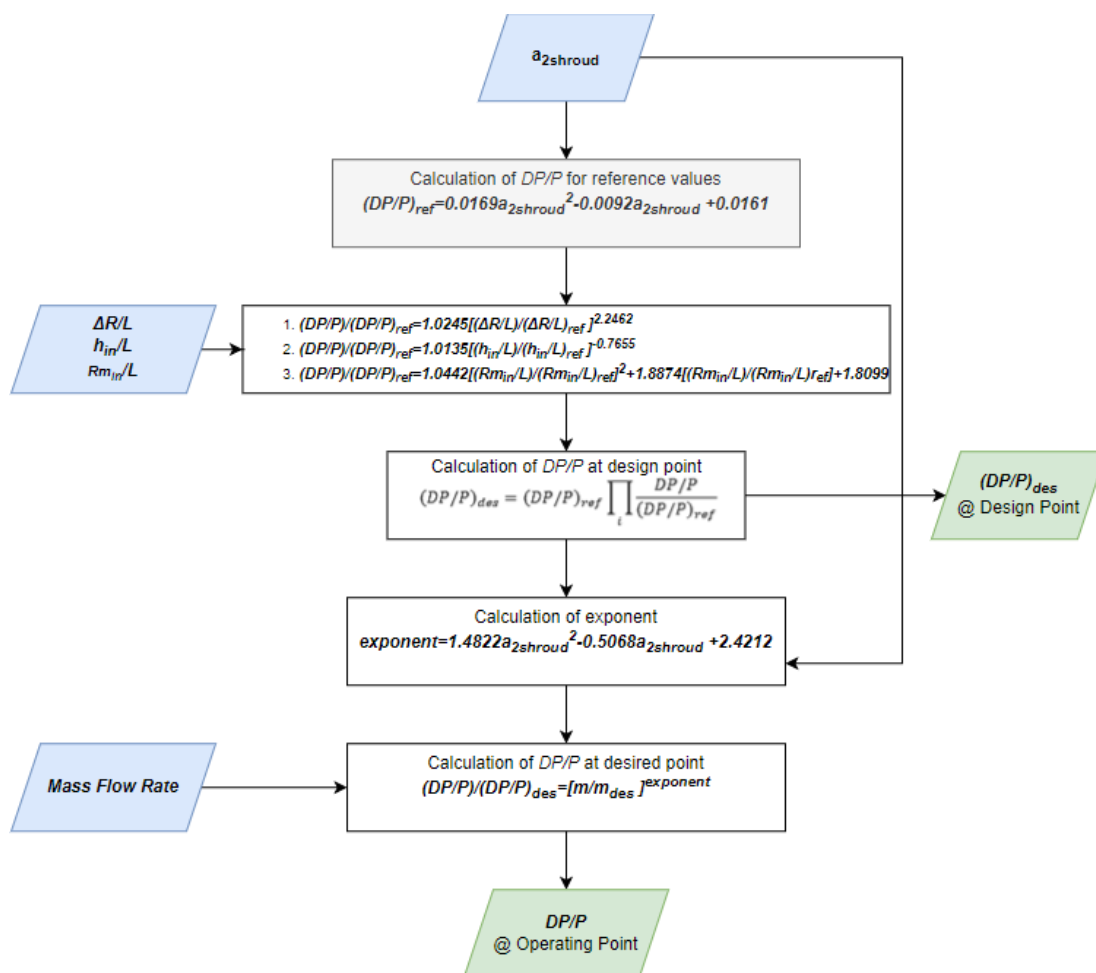


Σχήμα 12 Συσχέτιση συντελεστή απωλειών με  $\dot{m}$ .



Σχήμα 13 Εξάρτηση εκθέτη από  $a_{2shroud}$ .

Το μοντέλο που τελικά δημιουργήθηκε φαίνεται στο Σχήμα 14. Τα δεδομένα που απαιτούνται για τους υπολογισμούς είναι τα  $a_{2shroud}$ ,  $\dot{m}$  και οι αδιάστατες παράμετροι  $\Delta R/L, h_{in}/L, R_{min}/L$ , που είτε δίνονται απευθείας ως απαραίτητες για την πρώτη διαδικασία παραμετροποίησης ή προκύπτουν από τα  $(R_{hub}/R_{shroud})_{in}, (R_{hub}/R_{shroud})_{out}, M_{in}, M_{out}$  που απαιτούνται κατά την δεύτερη προτεινόμενης διαδικασίας.



Σχήμα 14 Περιγραφή μοντέλου εκτίμησης απωλειών.

### Επαλήθευση Μοντέλου

Για την επιβεβαίωση της ακρίβειας των εκτιμώντων μέσω του μοντέλου απωλειών εξετάστηκαν τέσσερις διαφορετικές περιπτώσεις. Τα δεδομένα που αντιστοιχούν σε κάθε μία από αυτές φαίνονται στον Πίνακα 6.

Case	$a_{2shroud}$	$\left(\frac{R_{hub}}{R_{shroud}}\right)_{in}$	$\left(\frac{R_{hub}}{R_{shroud}}\right)_{out}$	$L (m)$	$\dot{m}_{des} \left(\frac{kg}{s}\right)$	$Mach_{in}$	$Mach_{out}$
1	-0.4	0.8	0.64	0.50882	100	0.3618	0.5039
2	0.1	0.8	0.64	0.50882	100	0.3618	0.5039
3	-0.2	0.8	0.64	0.50882	50	0.3618	0.5039
4	-0.2	0.8	0.64	0.50882	25	0.3618	0.5039

Πίνακας 6 Δεδομένα περιπτώσεων που εξετάστηκαν για την επαλήθευση του μοντέλου.

Για κάθε περίπτωση ο συντελεστής απωλειών υπολογίστηκε μέσω του μοντέλου προκειμένου να συγκριθεί με την τιμή του που εξήχθη από τις προσομοιώσεις στο CFX. Επιπλέον, ένα μέγεθος που βρέθηκε και συγκρίθηκε είναι ο εκθέτης που χρησιμοποιείται

για την εύρεση των απωλειών όταν η μηχανή λειτουργεί εκτός του σημείου σχεδιασμού. Στον Πίνακα 7 φαίνονται τα αποτελέσματα των συγκρίσεων, με τις διαφοροποιήσεις μεταξύ των τιμών να μην ξεπερνούν το 10%. Ακόμη και όταν η απόκλιση μεταξύ των εκτιμώμενων απωλειών και των αποτελεσμάτων του CFD είναι 7%, όπως για την 2<sup>η</sup> περίπτωση, οι τιμές τους δεν απέχουν σημαντικά. Μέσω αυτής της διαδικασίας επαλήθευσης συμπεραίνεται ότι το μοντέλο προσφέρει ικανοποιητικές εκτιμήσεις για τους διαφορετικούς συνδυασμούς δεδομένων, με μέσο σφάλμα περίπου ίσο με 2.5%

		Estimated Value	CFD Value	Deviation (%)
Case 1	$(DP/P)_{des}$	1.42%	1.40%	1.69%
	<i>exponent</i>	2.8611	2.9471	2.92%
Case 2	$(DP/P)_{des}$	0.97%	1.04%	7.05%
	<i>exponent</i>	2.3853	2.424	1.59%
Case 3	$(DP/P)_{des}$	0.71%	0.70%	1.61%
	<i>exponent</i>	2.5818	2.5114	2.81%
Case 4	$(DP/P)_{des}$	0.48%	0.50%	3.00%
	<i>exponent</i>	2.5818	2.3496	9.88%

Πίνακας 7 Αποτελέσματα συγκρίσεων.

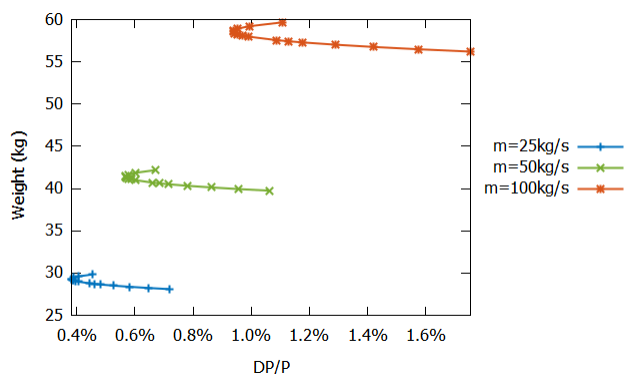
## Παραμετρική Μελέτη για Ελαχιστοποίηση Απωλειών

Με βάση τα αποτελέσματα του μοντέλου είναι δυνατόν να διεξαχθεί μία παραμετρική ανάλυση, προκειμένου να διαπιστωθεί η επιρροή των δεδομένων της *Parametrization Process II* στον συντελεστή απωλειών και να γίνουν εκτιμήσεις σχετικά με τις βέλτιστες τιμές για κάθε ένα από αυτά.

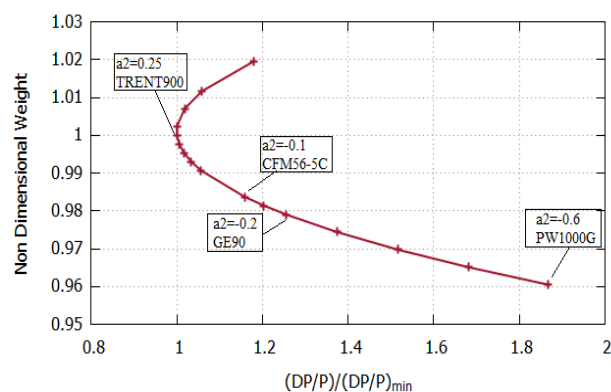
Κατά τον σχεδιασμό ενός αγωγού αεροπορικού κινητήρα ένας σημαντικός περιορισμός είναι το βάρος, καθώς στόχος είναι η σχεδίαση του ελαφρύτερου εξαρτήματος με την καλύτερη δυνατή απόδοση. Με την αλλαγή των παραμέτρων  $a_{2_{shroud}}$ ,  $L$ ,  $(R_{hub}/R_{shroud})_{in}$ ,  $(R_{hub}/R_{shroud})_{out}$ ,  $M_{in}$ ,  $M_{out}$ ,  $\dot{m}$  η γεωμετρία, και κατά συνέπεια και το βάρος, μεταβάλλονται. Στα πλαίσια αυτής της εργασίας, το βάρος του αγωγού τύπου S υπολογίζεται μέσω αριθμητικής ολοκλήρωσης, θεωρώντας ότι είναι κατασκευασμένος από χάλυβα  $\rho = 8000 \text{ kg/m}^3$  με πάχος τοιχωμάτων  $t = 2\text{mm}$ . Για κάθε μεταβλητή που εξετάστηκε παρουσιάστηκε η καμπύλη μεταβολής του βάρους συναρτήσει του συντελεστή απωλειών, το οποίο συχνά καλείται Pareto Front, και χρησιμοποιείται για την κατανόηση των αναγκαιών συμβιβασμών μεταξύ των σχεδιαστικών περιορισμών. Προκειμένου να είναι τα αποτελέσματα πιο ξεκάθαρα οι άξονες των διαγραμμάτων αδιαστατοποιήθηκαν ως προς τα μεγέθη που αντιστοιχούν στις ελάχιστες απώλειες.

Με την μεταβολή του  $a_{2_{shroud}}$  δημιουργήθηκαν στο Σχήμα 15 και Σχήμα 16. Όπως φαίνεται, για μικρότερες παροχές μάζας τόσο το βάρος όσο και οι απώλειες μετακινούνται προς χαμηλότερες τιμές, ενώ αν τα μεγέθη αδιαστατοποιηθούν οι καμπύλες θα συμπίπτουν. Τοποθετώντας επί της καμπύλης κάποιους κινητήρες, ανάλογα με το  $a_{2_{shroud}}$

που προέκυψε από την ψηφιοποίησή τους, παρατηρείται ότι αν και το βέλτιστο φαίνεται να αντιστοιχεί σε  $a_{2shroud} = 0.25$ , αρκετοί έχουν σχεδιαστεί με σκοπό την μείωση του βάρους, εις βάρος της απόδοσης. Η βέλτιστη τιμή που προκύπτει δεν αντιστοιχεί στην πραγματική, διότι δεν έχουν θεωρηθεί οι περιορισμοί λόγω της ύπαρξης των συμπιεστών.

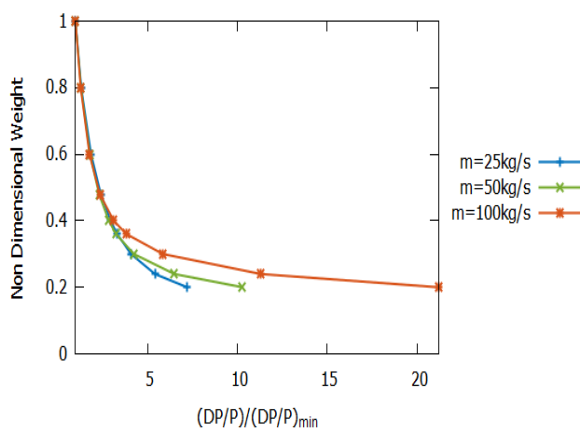


Σχήμα 15 Συσχέτιση βάρους, απωλειών για μεταβαλλόμενο  $a_{2shroud}$  και  $\dot{m}$ .

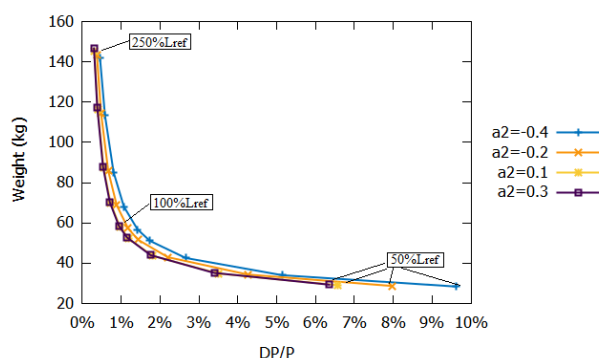


Σχήμα 16 Συσχέτιση βάρους, απωλειών για μεταβαλλόμενο  $a_{2shroud}$  σε αδιάστατους άξονες.

Με την αύξηση του μήκους  $L$ , όπως έχει ήδη εξηγηθεί, οι απώλειες μειώνονται. Ωστόσο, το βάρος του αγωγού αναμένεται να αυξηθεί σημαντικά. Από το Σχήμα 18, φαίνεται ότι για κάποια ανώτατη τιμή του μήκους οι απώλειες ελαχιστοποιούνται και πέραν αυτής το βάρος αυξάνεται χωρίς να υπάρχει βελτίωση στις επιδόσεις του αγωγού. Για μικρότερες τιμές της παροχής μάζας στο σημείο σχεδιασμού, Σχήμα 17, το ίδιο βάρος αγωγού αντιστοιχεί σε μικρότερες απώλειες, καθώς μειώνεται η αδιάστατη παράμετρος  $\Delta R/L$ .



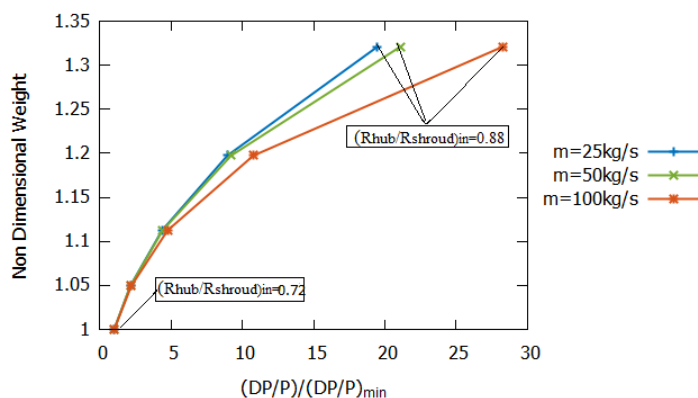
Σχήμα 17 Συσχέτιση βάρους, απωλειών για μεταβαλλόμενο  $L$ ,  $\dot{m}$ .



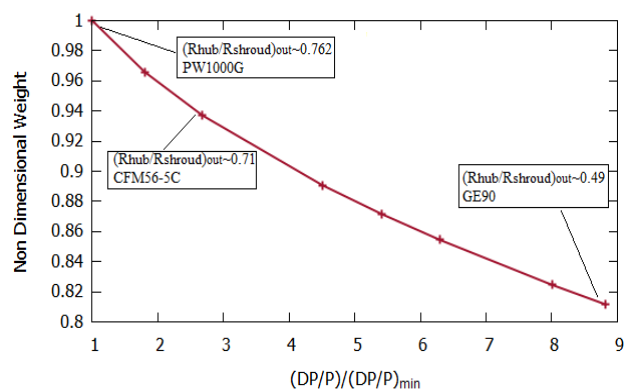
Σχήμα 18 Συσχέτιση βάρους, απωλειών για μεταβαλλόμενο  $L$  και  $a_{2shroud}$  100kg/s.

Για τους λόγους  $R_{hub}/R_{shroud}$ , τόσο στην είσοδο όσο και στην έξοδο του αγωγού, υπάρχει περιορισμός στις πιθανές τιμές τους, λόγω της άμεσης σχέσης τους με τις ακτίνες των συμπιεστών. Έτσι, οι περιοχές μεταβολής τους, όπως προκύπτουν από τις ψηφιοποιημένες μηχανές, είναι  $(R_{hub}/R_{shroud})_{in}: 0.72 - 0.88$  και  $(R_{hub}/R_{shroud})_{out}: 0.48 - 0.77$ . Η βέλτιστη τιμή του λόγου εισόδου, για επίτευξη του ελάχιστου βάρους και  $DP/P$ , με τον λόγο εξόδου σταθερό, για κάθε  $a_{2shroud}$ , αντιστοιχεί στο κάτω όριο του εύρους του

διότι με την αύξηση του αυξάνεται η παράμετρος  $\Delta R/L$  και μειώνεται η  $h_{in}/L$  οδηγώντας σε αύξηση των απωλειών. Αντίθετα, ο βέλτιστος λόγος ακτίνων για την ελαχιστοποίηση των απωλειών στην έξοδο είναι το άνω όριο του εύρους και οι αδιάστατες καμπύλες για τις διαφορετικές παροχές σχεδιασμού συμπίπτουν, όπως στο Σχήμα 20. Ωστόσο, δεν είναι δυνατή η ταυτόχρονη επιλογή βέλτιστων τιμών, καθώς τότε η ακτινική διαφορά μεταξύ εισόδου και εξόδου προκύπτει αρνητική. Κατ' επέκταση για την εύρεση του βέλτιστου συνδυασμού πρέπει να γίνει δοκιμή όλων των πιθανών γεωμετριών.

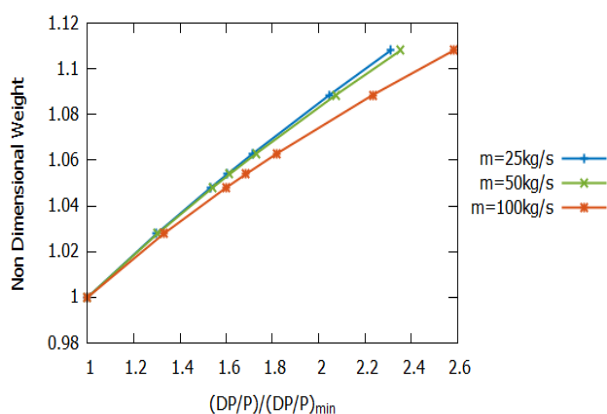


Σχήμα 19 Συσχέτιση βάρους, απωλειών για μεταβαλλόμενα  $(R_{hub}/R_{shroud})_{in}$   $\dot{m}$ .

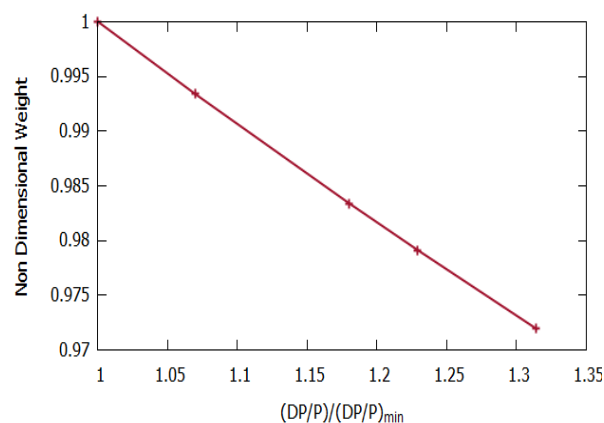


Σχήμα 20 Συσχέτιση βάρους, απωλειών για μεταβαλλόμενα  $(R_{hub}/R_{shroud})_{out}$ .

Τέλος, με την μεταβολή των αριθμών Mach της ροής στην είσοδο και στην έξοδο μεταβάλλονται και τα αντίστοιχα εμβαδά των διατομών, με αποτέλεσμα την μεταβολή των αδιάστατων γεωμετρικών παραμέτρων, δηλαδή της συνολικής γεωμετρίας του αγωγού. Όμοια με τους λόγους ακτίνων, το πιθανό εύρος των τιμών Mach περιορίζεται λόγω της τοποθέτησης του αγωγού ενδιάμεσα στους συμπιεστές. Έτσι, στην είσοδο  $M_{in}$ : 0.30 – 0.45, με βέλτιστη τιμή την  $M_{in} = 0.45$ , για κάθε  $a_{2shroud}$ , και στην έξοδο  $M_{out}$ : 0.45 – 0.55 με ελάχιστες απώλειες, αλλά μέγιστο βάρος, για  $M_{out} = 0.45$ . Ωστόσο, η επίδραση της μεταβολής των αριθμών Mach στο συντελεστή απωλειών δεν είναι τόσο δραστική. Όμοια με τις προηγούμενες παραμέτρους, για την εύρεση των βέλτιστων τιμών δεδομένων, θα πρέπει να εξετασθούν οι πιθανοί συνδυασμοί.



Σχήμα 21 Συσχέτιση βάρους, απωλειών για μεταβαλλόμενα  $M_{in}, \dot{m}$ .



Σχήμα 22 Συσχέτιση βάρους, απωλειών για μεταβαλλόμενα  $M_{out}, \dot{m}$ .

## Συμπεράσματα

Το μοντέλο που αναπτύχθηκε στα πλαίσια αυτής της εργασίας, και βασίζεται στα αποτελέσματα προσομοιώσεων με εργαλεία υψηλής ακρίβειας, παρέχει ικανοποιητικής ακρίβειας προβλέψεις για τις απώλειες ολικής πίεσης εντός του αγωγού που τοποθετείται ενδιάμεσα των συμπιεστών. Μέσω των αναλύσεων, των προσομοιώσεων και των παραμετρικών μελετών που έγιναν στα πλαίσια αυτής της εργασίας είναι δυνατό να εξαχθούν τα παρακάτω συμπεράσματα:

1. Για τους αγωγούς των ψηφιοποιημένων Turbofan κινητήρων παρατηρήθηκε ότι η κυρτότητα ή καμπυλότητα των τοιχωμάτων περιγράφεται με την χρήση των συντελεστών  $\alpha_2$ , για την πλήμνη και το κέλυφος. Πιο συγκεκριμένα, για το τοίχωμα της πλήμνης οι καμπυλότητες των δεκαεφτά αγωγών δεν διαφοροποιούνται σημαντικά ενώ για το κέλυφος ο συντελεστής κυμαίνεται από -0.63-0.67 με το S σχήμα σχεδόν να αντιστρέφεται για τις υψηλές θετικές τιμές.
2. Οι συντελεστές καμπυλότητας των τοιχωμάτων μπορούν να συσχετισθούν μεταξύ τους με την χρήση μίας προσεγγιστικής γραμμικής συνάρτησης. Κατά συνέπεια, για να καθοριστεί η κυρτότητα του αγωγού απαιτείται μόνο μία παράμετρος.
3. Οι απώλειες πίεσης επηρεάζονται σημαντικά από την καμπυλότητα των τοιχωμάτων του αγωγού. Με την αύξηση του  $\alpha_{2shroud}$  ο συντελεστής απωλειών μειώνεται ενώ η ελάχιστη τιμή βρέθηκε για περίπου  $\alpha_{2shroud} = 0.25$ .
4. Οι αδιάστατες γεωμετρικές παράμετροι συνδέονται άμεσα με τον συντελεστή απωλειών ολικής πίεσης. Ο λόγος της ακτινικής διαφοράς προς το μήκος  $\Delta R/L$  έχει την πιο σημαντική επίδραση στην αναπτυσσόμενη ροή και αυξανόμενος οδηγεί σε πιο απότομες γεωμετρίες και αυξημένες απώλειες. Από την άλλη, με την αύξηση



του  $h_{in}/L$  οι απώλειες μειώνονται. Η επίδραση της παραμέτρου  $R_{min}/L$  στον συντελεστή απωλειών είναι πολύ μικρή.

5. Για παροχές μάζας, εκτός του σημείου σχεδιασμού, ο συντελεστής απωλειών μεταβάλλεται μέσω μίας εκθετικής συνάρτησης. Στα υπάρχοντα μοντέλα, ο εκθέτης της συνάρτησης τίθεται ίσος με 2, που αντιστοιχεί στην αναγωγή των απωλειών στα σημεία εκτός σχεδιασμού για κυλινδρικούς αγωγούς. Στα πλαίσια αυτής της διπλωματικής εργασίας βρέθηκε συσχέτιση του εκθέτη με την καμπυλότητα των τοιχωμάτων του αγωγού τύπου S των ψηφιοποιημένων μηχανών.
6. Η ελάχιστη τιμή του συντελεστή απωλειών πίεσης, όπως υπολογίζεται από το μοντέλο, αντιστοιχεί σε  $a_{2shroud} = 0.25$ . Ωστόσο, για την δημιουργία αγωγών με ελάχιστο βάρος το  $a_{2shroud}$  πρέπει να λάβει τις χαμηλότερες δυνατές τιμές.
7. Με την αύξηση του μήκους του αγωγού το μοντέλο προβλέπει την αύξηση του βάρους και την μείωση των απωλειών, όπως είναι αναμενόμενο. Έπειτα από αύξηση του μήκους κατά περίπου 20%, από την τιμή αναφοράς, οι απώλειες πίεσης σχεδόν σταθεροποιούνται ενώ το βάρος συνεχίζει να μεγαλώνει.
8. Ο λόγος ( $R_{hub}/R_{shroud}$ ), στην είσοδο και την έξοδο οδηγεί σε αύξηση και μείωση της παραμέτρου  $\Delta R/L$ , αντίστοιχα. Έτσι, με αύξηση της τιμής εισόδου κατά πείπου 0.15 ο συντελεστής απωλειών αυξάνεται σχεδόν τριάντα φορές, ενώ η αντίστροφη συμπεριφορά παρατηρείται για τις τιμές στην έξοδο του αγωγού.
9. Τέλος, η μεταβολή των αριθμών Mach της εισερχόμενης και εξερχόμενης ροής έχουν λιγότερο σημαντική επιρροή στις εκτιμώμενες απώλειες πίεσης, μέσω της μεταβολής των γεωμετρικών παραμέτρων. Η αύξηση του Mach εισόδου επιφέρει μείωση των απωλειών ενώ το αντίθετο συμβαίνει για την τιμή του στην έξοδο.

Μελλοντικά, το μοντέλο που δημιουργήθηκε θα μπορούσε να χρησιμοποιηθεί για την διερεύνηση της επιρροής της γεωμετρίας του αγωγού στις συνολικές επιδόσεις του κινητήρα. Τέλος, για την αύξηση της ακρίβειας των εκτιμήσεων του μοντέλου θα πρέπει αυτό να εμπλουτιστεί με τους περιορισμούς που εισάγονται κατά τον σχεδιασμό του αγωγού λόγω της συνεργασίας του με τους συμπιεστές, της ύπαρξης βαλβίδων απομάστευσης αέρα και των υπολοίπων κατασκευαστικών χαρακτηριστικών του.